THE ANALYSIS OF A ROCKET TOMOGRAPHY MEASUREMENT OF THE N_2^+ 3914Å EMISSION AND N_2 IONIZATION RATES IN AN AURORAL ARC

NASA Grant No. NAG5-670

Principal Investigator

IAN C. McDADE

Space Physics Research Laboratory
Department of Atmospheric, Oceanic and Space Sciences
The University of Michigan

FINAL REPORT

July 1991

THE ANALYSIS OF A ROCKET TOMOGRAPHY MEASUREMENT OF THE N_2^+ 3914Å EMISSION AND N_2 IONIZATION RATES IN AN AURORAL ARC

NASA Grant No. NAG5-670

Principal Investigator

IAN C. McDADE

Space Physics Research Laboratory
Department of Atmospheric, Oceanic and Space Sciences
The University of Michigan

FINAL REPORT

July 1991

SUMMARY

During the one year performance period of this grant (May 1990 - July 1991) we have acheived all of the goals identified in the original proposal and statement of work and have developed techniques for recovering two-dimensional distributions of auroral volume emission rates from rocket photometer measurements made in a tomographic spin scan mode. These tomographic inversion procedures are based upon an algebraic reconstruction technique (ART) and utilize two different iterative relaxation techniques for solving the problems associated with noise in the observational data. One of the inversion algorithms is based upon a least squares method and the other on a maximum probability approach. The performance of the inversion algorithms, and the limitations of the rocket tomography technique, have been critically assessed using various sets of simulated rocket measurements which were generated from 'known' auroral emission rate distributions. These simulations have been used to investigate how the quality of the tomographic recovery may be influenced by various factors such as (i) statistical and non-statistical noise in the observational data, (ii) rocket penetration of the auroral form, (iii) background sources of emission, (iv) smearing due to the photometer field of view, and (v) temporal variations in the auroral form. These tests show that the inversion procedures may be successfully applied to rocket observations made in medium intensity aurora with standard rocket photometer instruments.

The inversion procedures have been used to recover two-dimensional distributions of auroral emission rates and ionization rates from an existing set of N_2^+ 3914Å rocket photometer measurements which were made in a tomographic spin scan mode during the ARIES auroral campaign. The two-dimensional distributions of the 3914Å volume emission rates recovered from the inversion of the rocket data compare very well with the distributions that were inferred from ground-based measurements using triangulation-tomography techniques and the N_2 ionization rates derived from the rocket tomography results are in very good agreement with the *in situ* particle measurements that were made during the flight.

A presentation on the inversion procedures was made at the 1990 American Geophysical Union Fall Meeting in San Francisco and three papers describing the tomographic inversion techniques and the tomographic analysis of the ARIES rocket data have been published or accepted for publication.

1.

THE TOMOGRAPHIC INVERSION PROCEDURES - FORMULATION AND PERFORMANCE ASSESSMENT

The inversion procedures that have been developed for recovering two-dimensional distributions of auroral emission rates from tomographic spin-scan rocket photometer measurements are described in detail in Appendix "**A**" of this report. This appendix is a pre-print of a paper that has been accepted for publication in a forthcoming Space Physics special issue of the *Canadian Journal of Physics*. Appendix 'A' also describes the results of the tests that have been performed to assess the efficacy of the two inversion techniques developed under the grant.

2.

THE RESULTS OF THE TOMOGRAPHIC INVERSION OF THE ARIES 3914Å ROCKET PHOTOMETER MEASUREMENTS

The results obtained when the tomographic inversion procedures are applied to the N_2^+ 3914Å photometer measurements made during the ARIES rocket flight are described in detail in Appendix "**B**". This appendix is a pre-print of a paper which is to appear in the June 1991 (Vol. 39, No. 6) issue of *Planetary and Space Science*.

3.

THE N_2^+ EMISSION RATE DISTRIBUTIONS RECOVERED FROM THE ARIES ROCKET DATA COMPARED TO THE *IN SITU* PARTICLE MEASUREMENTS AND GROUND BASED OBSERVATIONS MADE DURING THE FLIGHT

Appendix "**C**" describes how the the two-dimensional distributions of the auroral N_2^+ 3914Å emission rates recovered from the tomographic inversion of the ARIES rocket data compare with (a) the *in situ* particle measurements, and (b) the coordinated ground-based observations that were made during the rocket flight. The analysis presented in Appendix C shows that although the emission rate distributions recovered from the rocket tomography measurements are in good agreement with those deduced from the ground-based observations, the N_2^+ ionization rates inferred from the rocket tomography results are in better agreement with the *in situ* particle measurements. Appendix C is a pre-print of a paper that has been accepted for publication in *Planetary and Space Science*.

PUBLICATIONS RELATED TO THE WORK PERFORMED UNDER THIS GRANT

McDade, I.C., Lloyd, N.D. and Llewellyn, E.J., A Rocket Tomography Measurement of the N_2^+ 3914Å Emission Rates within an Auroral Arc, *Planet. Space Sci.*, **39**, 895, 1991.

McDade, I.C.and Llewellyn, E.J., Inversion Techniques for Recovering Two-Dimensional Distributions of Auroral Emission Rates from Tomographic Rocket Photometer Measurements, *Can. J. Phys.*, In press 1991.

Vallance Jones, A., Gattinger, R.L., Creutzberg, F., Harris, F.R., McNamara, A.G., Yau, A.W., Llewellyn, E.J., Lummerzheim, D., Rees, M.H., McDade, I.C. and Margot, J., The ARIES Auroral Modelling Campaign: Characterization and Modelling of an Evening Auroral Arc Observed from a Rocket and a Ground-Based Line of Meridian Scanners, *Planet. Space Sci* , In press 1991.

THE ANALYSIS OF A ROCKET TOMOGRAPHY MEASUREMENT OF THE N_2^+ 3914Å EMISSION AND N_2 IONIZATION RATES IN AN AURORAL ARC

NASA Grant No. NAG5-670

FINAL REPORT

APPENDIX 'A'

"Inversion Techniques for Recovering Two-Dimensional Distributions of Auroral Emission Rates from Tomographic Rocket Photometer Measurements"

Ian. C. McDade
Space Physics Research Laboratory
Department of Atmospheric, Oceanic and Space Sciences
The University of Michigan

and

Edward J. Llewellyn
Institute of Space and Atmospheric Studies,Department of Physics
University of Saskatchewan

Accepted for publication in *Canadian Journal of Physics*, 1991

Abstract. In this paper we demonstrate how the spatial distribution of optical emission rates within an auroral arc may be recovered from rocket photometer measurements made in a tomographic spin scan mode. We describe the tomographic inversion procedures required to recover this information and the implementation of two inversion algorithms which are particularly well suited for dealing with the problem of noise in the observational data. These algorithms are based upon the algebraic reconstruction technique, ART, and utilize 'Least Squares' and 'Maximum Probability' iterative relaxation methods. The performance of the inversion algorithms, and the limitations of the rocket tomography technique, are assessed using various sets of simulated rocket measurements generated from 'known' auroral emission rate distributions. The simulations are used to investigate how the quality of the tomographic recovery may be influenced by various factors such as noise in the data, rocket penetration of the auroral form, background sources of emission, smearing due to the photometer field of view, and temporal variations in the auroral form.

1. INTRODUCTION

Rocket photometry measurements are widely used to study auroral and airglow excitation processes. In conventional auroral rocket photometry the altitude variation of the auroral brightness measured above the rocket is used to determine the altitude profile of the volume emission rates of a particular auroral feature. However, if the photometer measurements are also made in other directions during the flight then it is possible to obtain information about the spatial distribution of the emission rates within the vertical/horizontal plane of the rocket trajectory. This 'tomographic' approach to rocket photometry is a logical extension of the methods that have been developed during the last decade to recover airglow and auroral emission rate distributions from satellite measurements [*Thomas and Donahue*, 1977; *Hays et al.*, 1978; *Wasser and Donahue*, 1979; *Fesen and Hays*, 1982; *Solomon et al.*, 1984; *Solomon et al.*, 1985; *Solomon et al.*, 1988]. In this paper we describe methods for recovering auroral emission rate distributions from rocket measurements and we assess the performance of the inversion algorithms using sets of simulated test data. A separate paper [*McDade et al.*, 1991] describes the results which are obtained when these methods are used to invert a set of actual tomographic rocket measurements.

2. THE TOMOGRAPHIC INVERSION PROCEDURES

The problem of recovering spatial distributions of auroral volume emission rates from tomographic auroral brightness measurements is, in essence, the inverse problem of reconstructing a two dimensional spatial function from information about its line integrals. *Solomon et al.* [1984; 1985; 1988] have previously considered how this problem might be addressed when the measurements are made from an orbital platform and they have developed Fourier transform methods for inverting satellite data. The techniques developed by *Solomon et al.* [1984; 1985; 1988] are based upon numerical integration of the Cormack

inversion integral [*Cormack*, 1963] and they are, therefore, a natural choice for inverting limb observations made from a platform in circular, or near circular, earth orbit. Unfortunately, these methods cannot be readily applied to observations that are made along lines of sight that intersect the solid earth and they are not well suited for inverting rocket measurements which, by necessity, have to be made over a very limited range of horizontal displacements. To solve the sub-orbital problem we have, therefore, examined an alternative approach which is based upon the tomographic inversion method known as algebraic reconstruction. The algebraic reconstruction technique, or ART as it is sometimes known, was originally developed by Gordon *et al.* [1970] for solving tomographic inversion problems in radiology and procedures based on variations of this method have been used in the past to invert tomographic satellite airglow measurements [*Thomas and Donahue*, 1977; *Hays et al.*, 1978; *Wasser and Donahue* , 1979; *Fesen and Hays* , 1982].

Observational Requirements

The aim of the generic auroral tomography experiment is to obtain information about the two-dimensional distribution of the optical emission rates within a well defined vertical plane intersecting a discrete aurora form. To realize this objective using rocket measurements the vehicle should ideally be launched along a trajectory that encloses the auroral form as shown in Figure 1. During the flight a simple filter photometer, or some other optical instrument with a narrow field of view, would be used in a spin scan mode to measure the auroral brightnesses at elevations ranging from 0° to 360° in the plane of the rocket trajectory. The photometer spin rate should be fast enough to allow many complete scans to be acquired during the flight and the elevation angle sampling interval should be smaller than, or comparable to, the angular field of view of the photometer. The observational data set resulting from the experiment would then consist of a series of tomographic auroral brightness scans made from a large number of viewing positions along the rocket flight trajectory.

The Algebraic Reconstruction Formulation

In order to invert this set of tomographic measurements using algebraic reconstruction the atmospheric region of interest, within the plane of the rocket trajectory, is divided into a number of geometric elements as shown in Figure 2. The number and size of the elements is chosen so that the problem is overdetermined, i.e., the total number of elements for which volume emission rates are to be recovered, J_{tot}, is less than the total number of observations made, N_{obs}. Within each spatial element the auroral emission rate is assumed to be uniform and isotropic and the auroral brightness measured in a given direction is considered to be the sum of the contributions from all the elements that lie along the line of sight. Each of the auroral brightnesses measured during the flight, O_i, can then be expressed in terms of the volume emission rates in these elements weighted by the path length through each element, i.e.,

$$O_i = S \sum_{j=1}^{J_{tot}} L_{ij} V_j \qquad i = 1, .., N_{obs} \tag{1}$$

where V_j is the volume emission rate within the element j, L_{ij} represents the path length of the line of sight of observation i through the element j and S is an instrument calibration factor expressed in units commensurate with those adopted for O_i, V_j and L_{ij}. To simplify the formulation described below we will assume that the instrument calibration factor is included within the pathlength weighting factors, L_{ij}. Since the weighting factors can be readily obtained from geometric considerations, the tomographic inversion problem reduces to the problem of solving the system of linear equations defined by (1). In the absence of noise an exact solution to the set of equations should exist and this may, in principle, be found using standard matrix inversion techniques. However, in the presence of noise no exact, or unique, solution will exist and the problem is to find the set of volume emission rates that is most consistent with the observations. To recover this set of emission rates

from potentially noisy measurements we have investigated two different approaches both of which are based on iterative relaxation techniques. The first approach, which we will refer to as the 'maximum probability method', is based upon a deconvolution algorithm developed by *Lloyd and Llewellyn* [1989] for deblurring images that are subject to Poisson noise. The second approach, which we will referred to as the 'least squares method', is based upon the iterative least squares algebraic reconstruction technique described by *Budinger and Gullberg* [1974].

The Maximum Probability Method

This iterative method for solving the system of linear equations (1) is based upon an algorithm which allows for the effects of noise in the data by taking into account the Poisson counting statistics of the photometer measurements. To implement this algorithm the auroral brightnesses measured during the rocket flight must be expressed in terms of the number of photons detected during each photometer count integration period.

The algorithm is based upon the premise that the number of photons actually observed along a particular line of sight will deviate, to some extent, from that given by equation (1) due to the Poisson counting statistics of the measurement. However, the actual number of photons observed, O_i, will still be the sum of the contributions from the elements which lie along the line of sight. The contribution, C_{ij}, that the element j made to the observation i can never be established but it will have been some random Poisson deviate drawn from $L_{ij}V_j$,which is the contribution that should be expected from element j in the mean. If the number of elements intersected by the line of sight of the ith observation is n_i then there are $(n_i+O_i-1)!/\{(n_i-1)!O_i!\}$ different ways in which the O_i photons could possibly have been received, i.e., there are $(n_i+O_i-1)!/\{(n_i-1)!O_i!\}$ distinguishable sets of C_{ij} values which sum to the total observed O_i. However, each of these $(n_i+O_i-1)!/\{(n_i-1)!O_i!\}$ permutations has a different intrinsic probability and if the 'true' set of V_j values is known, the relative

probability associated with each permutation can be calculated and the most likely permutation can be found for each observation. Fortunately, it is not necessary to calculate the probability associated with each permutation in order to identify the one which is most likely and *Lloyd and Llewellyn* [1989] have shown that the set of contributions, $C_{ij}^{@\max P}$, associated with the most likely permutation can be estimated, for those elements along the line of sight, using the expression

$$C_{ij}^{@\max P} = \frac{(O_i + n_i) L_{ij} V_j}{\sum_{j=1}^{J_{tot}} L_{ij} V_j} - 1 \qquad (2)$$

The 'maximum probability' algorithm uses this relationship to seek the ensemble of C_{ij} values, and hence the set of volume emission rates, that has the highest probability of having produced the entire set of observations. The iterative process is initiated using an arbitrary set of 'first guess' V_j values which may be, for example, a uniformed distribution. At each step of the iterative process the V_j 's are modified in an attempt to obtain a better estimate of the volume emission rates and a new set of emission rates, V_j^{new}, is obtained. This is achieved using the iteration formula

$$V_j^{new} = \frac{\sum_{i=1}^{N_{obs}} C_{ij}^{@\max P}}{\sum_{i=1}^{N_{obs}} L_{ij}} \qquad (3)$$

where each of the $C_{ij}^{@\max P}$ is calculated from equation (2) using the V_j 's obtained at the end of the previous iteration. As the iterative process proceeds a consistent set of $C_{ij}^{@\max P}$ and V_j values would emerge and the procedure is terminated when the recovered volume emission rates converge on a stable solution.

The Least Squares Method

The iterative least squares method attempts to find the set of volume emission rates that minimizes the the error function

$$\chi^2 = \sum_{i=1}^{N_{obs}} \frac{(O_i - R_i)^2}{\sigma_i^2} \tag{4}$$

where O_i is, as before, the auroral brightness measured along the line of sight i, σ_i is the standard deviation associated with each of the measured brightnesses and R_i is the brightness reconstructed from the recovered V_j's using the expression

$$R_i = \sum_{j=1}^{J_{tot}} L_{ij} V_j^{recovered} \tag{5}$$

As in the case of the maximum probability method, the iterative process is initiated using some arbitrary set of 'first guess' V_j values. The derivation of the least squares algorithm is described in detail by *Budinger and Gullberg* [1974] and we simply present here the Budinger and Gullberg iteration formulae converted to our notation.

At each iteration step a new set of volume emission rates is obtained from the previous set using the formula

$$V_j^{new} = \max\{0\ ,\ (V_j^{old} + \delta \times \Delta V_j)\} \tag{6}$$

where the function max{0, x} represents 'take the larger of 0 or x'. The quantity ΔV_j appearing in equation (6) varies from element to element and is given by

$$\Delta V_j = \frac{\sum_{i=1}^{N_{obs}} L_{ij}(O_i - R_i)/\sigma_i^2}{\sum_{i=1}^{N_{obs}} (L_{ij}/\sigma_i)^2} \tag{7}$$

The quantity δ in equation (6) is a damping factor which is fixed for all elements and is given by

$$\delta = \frac{\sum_{i=1}^{N_{obs}} \left[(O_i - R_i) \sum_{j=1}^{J_{tot}} L_{ij} \Delta V_j / \sigma_i^2 \right]}{\sum_{i=1}^{N_{obs}} \left[\sum_{j=1}^{J_{tot}} L_{ij} \Delta V_j / \sigma_i \right]^2} \qquad (8)$$

If the measured brightnesses, O_i, are expressed in terms of the number of photons detected during each photometer count integration period then the σ_i appearing in equations (7) and (8) may be replaced with $\sqrt{O_i}$.

As the 'least squares' iteration process proceeds the complete set of V_j values is modified in the direction of decreasing χ^2 and a better estimate of the true volume emission rates is obtained. The iterative process is terminated when the recovered volume emission rates have converged on a stable solution.

3. ASSESSMENT OF THE INVERSION PROCEDURES

The performances of the inversion procedures described above have been tested using sets of simulated rocket measurements which were generated from 'known' auroral emission rate distributions using various observational and flight trajectory parameters. These sets of simulated measurements were inverted using the 'maximum probability' and 'least squares' methods and the 'recovered' emission rates were compared with those used to generate the test data. The results of these tests are described below.

Ideal Observing Geometry Without Noise in the Data

To test the performance of the inversion procedures under the most favourable conditions a set of simulated rocket photometer measurements was generated for the flight trajectory and auroral emission rate distribution shown in Figure 3. The test data consisted of 15,000 photometer measurements made over a 5 minute segment of the rocket flight between the altitudes of 115 km on the flight up-leg and 80 km on the downleg. The test data were modelled assuming a photometer sensitivity of 10 counts sec^{-1} $Rayleigh^{-1}$ and a sampling frequency of 50 Hz , i.e., a count integration period of 20 msec. The photometer was assumed to scan through elevation angles at the rate of 200° sec^{-1} (4° per integration period) and the simulated measurements were calculated on the basis of the photometer line of sight at the midpoint of each sampling interval. The complete data set consisted, therefore, of ~167 auroral scans with 90 observations per scan.

To invert this set of measurements a rectangle in the plane of the rocket trajectory, lying between 18.5 km and 243.5 km from the launch site and extending from 80.5 km to 203.5 km in altitude, was divided into a 75×41 grid containing 3075 elements each 3km × 3km square. This geometry was used to calculate the line of sight weighting factors described in Section 2.

For the initial tests the 'maximum probability' and 'least squares' algorithms were used to invert the set of simulated observations under noise-free conditions, i.e., a noise component was not added to the input observations. The inversion procedures were initiated using a uniformed emission rate distribution of ~300 photons cm^{-3} s^{-1} in each of the 3075 elements. This was obtained by dividing the sum of the 15,000 observed brightnesses by the sum of all of the contributing weights. The progress of the inversion procedures towards a stable solution was monitored by examining three different

quantities. These were, (i) the χ^2 function defined in equation (4), (ii) the root mean square difference between the 'observed' and 'reconstructed' brightnesses.

$$rmsd\ Obs = \sqrt{\sum_{i=1}^{N_{obs}} (O_i - R_i)^2 / N_{obs}} \tag{9}$$

and (iii) the root mean square difference between the 'true' and 'recovered' volume emission rates,

$$rmsd\ Vs = \sqrt{\sum_{j=1}^{J_{tot}} (V_j^{true} - V_j^{recovered})^2 / J_{tot}} \tag{10}$$

Figure 4 shows how these three quantities varied during the 'maximum probability' and 'least squares' inversions of the noise-free data set. The volume emission rates recovered with the 'maximum probability' method had converged after approximately 12 iterations and those obtained using the 'least squares' method had effectively converged on a slightly smaller value for *rmsd Vs* after 18 iterations. The 'maximum probability' method converged more rapidly than the 'least squares' method and although the 'least squares' χ^2 error function continues to decrease beyond the 18th iteration, the corresponding improvement in the root mean square difference between the 'true' and 'recovered' volume emission rates is not very significant. The distributions of volume emission rates recovered at the end of the 12th iteration of the 'maximum probability' inversion and at the end of the 18th iteration of the 'least squares' inversion are reproduced in Figures 5 and 6. A comparison of Figures 3, 5 and 6 demonstrates that the volume emission rates used to generate the observations were successfully recovered from the noise-free observations with considerable fidelity.

Ideal Observing Geometry With Noise in the Data

The effects of noise in the observational data were first examined by adding a Poisson noise component to each of the input observations, i.e., each O_i in the set of 15,000 observations was replaced by a random deviate O_i' drawn from a Poisson distribution with a mean of O_i. The volume emission rate distributions recovered from the inversions of the this noisy data set did not differ significantly from those shown in Figures 5 and 6. This indicates that statistical Poisson noise in the observations does not seriously affect the quality of the inversion when the observations are made using a photometer with a sensitivity of ~10 counts sec^{-1} $Rayleigh^{-1}$ in an aurora of comparable intensity to that shown in Figure 3.

In order to examine how the inversions might be affected by the presence of non-statistical noise, or by lower signal-to-noise ratios, tests were performed using simulated data sets in which the noise component was amplified by various factors. These tests show that the inversion procedures may still be used even if the signal-to-noise ratio is quite low. For example, in one of the tests the Poisson noise component of the observations considered in the previous paragraph was amplified by a factor of $\sqrt{50}$. A sample of these observations, corresponding to part of a scan made close to apogee, is reproduced in Figure 7 to illustrate the extent to which the signal-to-noise ratio was degraded by the introduction of the amplified noise. Figure 8 shows how the three quantities χ^2, *rmsd Vs* and *rmsd Obs* varied during the 'maximum probability' and 'least squares' inversions of the data set with the amplified noise. Under these circumstances the 'maximum probability' algorithm performed significantly better than the 'least squares' method. The *rmsd Obs* obtained with both methods converged on the value of the r.m.s. difference between the 'noise free' and 'amplified noise' measurements, but the final r.m.s. difference between the 'true' and 'recovered' volume emission rates obtained using the 'maximum

probability' method was approximately a factor of two smaller than that obtained with the 'least squares' method. The emission rate distributions recovered at the end of the 12th iteration of the 'maximum probability' inversion and at the end of the 18th iteration of the 'least squares' inversion are reproduced in Figures 9 and 10. Clearly, a comparison of Figure 3, 9 and 10 reveals that the 'maximum probability' and 'least squares' inversion techniques may still be used to recover the auroral emission rate distributions even if the observations have a relatively low signal-to-noise ratio.

Rocket Penetration of the Auroral Form and Contributions from Regions not Enclosed by the Flight Trajectory

In any 'real' rocket tomography experiment it must be anticipated that the rocket trajectory may not completely enclose the auroral form and that the actual flight data may contain contributions from other sources of emission. These may include distant auroral forms, the quiescent airglow and, for unabsorbed emissions, the albedo from the ground or lower atmosphere. It is important, therefore, to consider how the results of the tomographic inversions may be influenced by these factors.

To investigate the effects of incomplete trajectory enclosure of the aurora, simulations were performed using flight trajectories which passed through the form. The results of these tests show that the emission rates in the elements lying within the region enclosed by the trajectory can still be recovered with some confidence. However, for elements lying outside this region the discrepancy between the 'true' and 'recovered' emission rates can be quite large and the magnitude of this discrepancy generally increases with displacement from the trajectory. To illustrate how penetration of the aurora may adversely affect the inversion we reproduce in Figure 12 the emission rate distribution that was recovered from a 'maximum probability' inversion of a set of simulated observations which were generated using the auroral distribution and flight trajectory shown Figure 11.

It should be noted that in the auroral penetration case discussed above the simulated observations only contained emission from regions lying within the grid defined for the algebraic reconstruction and if the observations contain contributions from regions outside of the reconstruction grid then more serious distortions can arise. However, these problems may be dealt with in a number of ways. Firstly, additional elements of appropriate geometries may be added to the primary array of auroral elements to accommodate other anticipated sources of emission. For example, secondary arrays of annular elements may be added to accommodate emission from stratified airglow layers and a linear array of ground elements, lying within the plane of the photometer scan, may be incorporated to allow for any contributions from the ground albedo [*McDade et al.*, 1991]. Tests performed using this approach show that contributions from the limb enhanced airglow and the ground albedo can be taken into account and that the stratified airglow volume emission rates, and the ground surface brightnesses, can also be recovered along with the two dimensional distributions of auroral emission rates. This method does, however, require assumptions to be made about the albedo phase function and the homogeneity of the airglow emission rates. Alternatively, the problems that may arise from airglow emissions, or more distant sources of auroral emission, may be avoided by differencing pairs of observations made along common lines of sight from two different positions on the trajectory. In a sense this operation is implicitly performed by the inversion algorithms in their standard form and this explains why the volume emission rates recovered for elements lying in the region enclosed by the trajectory are not significantly distorted when the trajectory does not completely enclose the form. In a similar manner, contributions from the ground albedo may be taken into account using the downward viewing observations made when the rocket is below the auroral form on the upleg or the downleg of the flight. This method still requires, however, that the nature of

the albedo phase function is known or determined from the observations made when the rocket is below the form.

Field of View and Spin Scan Smearing Effects

So far we have assumed that the rocket observations may be reconstructed using a line of sight approximation and we now consider to what extent the tomographic recovery might be degraded by (a) the finite field of view of the photometer, and (b) the elevation angle smearing associated with the spin of the photometer during the count integration period. Both of these effects were examined by generating sets of test data that took into account the smearing due to the photometer field of view and the motion of the photometer optical axis during the count integration period. These sets of smeared observations were then inverted using the 'maximum probability' and 'least squares' inversion algorithms in their standard forms, i.e., the inversions were performed assuming that the input data represented instantaneous measurements made along single lines of sight. Since the photometer spatial capture function may be convolved with the scan motion of the optical axis to obtain the effective field of view, it is convenient to discuss the impact of both smearing effects in terms of the impact of this convolved quantity. For example, if the photometer optical axis scanned through 4° during the count integration period and the instrument had a square field of view 4° wide, then the apparent brightness measured during each count integration period would be the same as the brightness measured by a stationary photometer with a triangular capture function 4° wide at half maximum operating in a stepped scan mode.

The tests performed using the field of view smeared, and the spin smeared, sets of data show that observations obtained with effective fields of view of up to 10° wide (FWHM) can be successfully inverted using the inversion procedures in their standard single line of sight forms. These tests also show that useful information can still be recovered, using this

standard approach, even if the observations are obtained using an instrument with an effective field of view as large as ~20°(FWHM). For example, the emission rate distribution shown in Figure 13 was recovered from a standard 'maximum probability' inversion of a set of observations which were smeared using a triangular field of view 20° wide at half maximum. This set of rather heavily smeared observations was generated using the trajectory and distribution of emission rates shown in Figure 3. The standard 'maximum probability' inversion of these observations converged on a r.m.s. difference between the 'true' and 'recovered' volume emission rates of *rmsd Vs* = 173 photons cm^{-3} s^{-1}.

It is also possible to modify the procedures to enhance the quality of the inversions of heavily smeared observations. This may be achieved by calculating the L_{ij} weighting factors at a number of angular intervals across the effective field of view and summing these weights according to the magnitude of the off-axis capture function. The results of such a 'field weighted weights' inversion of the set of heavily smeared observations described in the previous paragraph is shown in Figure 14. The final r.m.s. difference between the 'true' and 'recovered' volume emission rates obtained using this 'weighted weights' approach was 84 photons cm^{-3} s^{-1}. This value for *rmsd Vs* is approximately a factor of two smaller than that obtained using the standard approach and, as a comparison of Figures 3, 13 and 14 reveals, the 'weighted weights' method is more successful at resolving the two peaks in the auroral emission rate distribution.

Temporal Variations in the Aurora

It is tacitly assumed by the algebraic reconstruction formulation that the auroral emission rates do not change during the time taken to acquire the rocket observations. Since one cannot expect this condition to be completely satisfied during any real experiment, it is important to establish how sensitive the inversions may be to temporal

variations in the auroral form. Clearly, the inversion procedures cannot be expected to provide reliable results if the auroral emission rates vary in an irregular fashion during the observation period. However, tests performed using simulations based on slowly varying aurora demonstrate that useful information can still be extracted from observations made in non-stationary forms. For example, the test distribution shown in Figure 3 is actually the sum of two auroral components which were generated by multiplying two Chapman-like vertical profiles by Gaussian horizontal amplitude factors. In one of the tests performed to investigate the temporal effects the input data were generated to simulate the observations that would result if the intensities of the two auroral components varied linearly in time so that their relative amplitudes changed by a factor of four between the start of the observing period (at 115 km on ascent) and the end of the period (at 80 km on descent). For this simulation the initial and final amplitudes of the two auroral components were chosen so that the average auroral distribution during the 5 minute observing period was the same as that shown in Figure 3. When these observations were inverted using the 'maximum probability' and 'least squares' methods the recovered emission rate distributions were found to be very similar to the mean 'true' distribution, i.e., the recovered emission rates were very similar to the time averaged emission rates in each element.

In order to examine if information can be extracted about the auroral distributions at specific times, we also investigated the possibility of inverting short segments of the flight data using the recovered 'mean' distribution as the first guess. Ideally, the subsets of the data used for this inversion should represent measurements made over as short a time interval as possible in order the minimize the effects of the auroral variations. However, if this interval is made too short then much of the tomographic information is lost as all of the measurements will have been made from essentially the same viewing position. Furthermore, as the interval is contracted the effective signal-to-noise ratio in the observations decreases. The minimum segment duration that can provide useful

information depends upon the magnitude of the auroral variations. For the simulation discussed in the previous paragraph we find that useful information about the history of the aurora can be obtained from inversions of segments of the data acquired over intervals of 10 to 15 seconds in duration. The effectiveness of this approach is clearly demonstrated in Figures 15 and 16 which show the 'true' auroral distributions at two specific times during the time dependent aurora simulation and the emission rate distributions that were recovered from inversions of the observations made during the two 15 second intervals centered on these times.

4. Discussion and Conclusions

The tests described in the previous section clearly demonstrate that an algebraic reconstruction technique based on the 'maximum probability' and 'least squares' iterative relaxation algorithms may be used to recover two-dimensional distributions of auroral volume emission rates from rocket photometer measurements made in medium intensity aurora. The tests also reveal that the 'maximum probability' method converges more rapidly than the 'least squares' method, and, in the presence of noise, recovers the 'true' distribution with somewhat greater fidelity. We should also note that the 'maximum probability' method is computationally more efficient. For example, a 'maximum probability' inversion involving 15,000 observations and 3,000 volume elements, requires approximately 1 minute of CPU time for each iteration on the University of Michigan Space Physics Research Laboratory's VAX 8600, whereas, the same inversion performed with the 'least squares' algorithm requires ~2 minutes of CPU. However, the 'maximum probability' method also offers a more important advantage in that it allows the possible errors in each of the recovered volume emission rates to be estimated in a fairly straightforward manner.

The iteration formula used by the 'maximum probability' method, equation (3), may

also be expressed as

$$V_j^{new} = \frac{n_j \times C_j^{mean}}{\Sigma L_j} \tag{11}$$

where n_j is the number of observations with finite pathlengths through the element j, ΣL_j is the sum of these pathlengths and C_j^{mean} is the mean value of the maximum probability contributions assigned to the element j. Since n_j and ΣL_j are known quantities defined by the geometry of the observations, an estimate of the standard error, σ_{V_j}, in each of the recovered volume emission rates may be obtained from an estimate of the standard error associated with the determination of C_j^{mean} at convergence. The latter quantity may be determined [*Bevington*, 1969] from the variance of the maximum probability contributions assigned to the element j and an estimate of the standard error in each of the recovered volume emission rates may then be obtained from

$$\sigma_{V_j} = \frac{n_j}{\Sigma L_j} \sqrt{\frac{1}{(n_j - 1)\, n_j} \sum_{k=1}^{n_j} (C_j^k - C_j^{mean})^2} \tag{1}$$

where the C_j^k are the set of 'n_j' maximum probability contributions assigned to the element j. In Figure 17 we show how the estimated uncertainties obtained using this formulation compare with the discrepancies between the 'true' emission rates and the 'recovered' emission rates for the case of the test data with amplified noise discussed in Section 3. Although only about 60% of the recovered emission rates lie within $\pm 2\sigma_{V_j}$ of their true values, this example shows that the error formulation does provide a reasonable sense of the possible errors in the recovered emission rates.

Acknowledgements. This work was supported by the National Aeronautics and Space Administration grant NAG5-670 to the University of Michigan. The authors would like to express their thanks to Dr. N.D. Lloyd (Institute of Space and Atmospheric Studies, University of Saskatchewan) and Mr. G. Roger (a participant in the National Science Foundation Research Experience for Undergraduates Program at the Space Physics Research Laboratory) for their invaluable contributions to the development and testing of the maximum probability algorithm discussed in this work.

REFERENCES

Bevington, P. R., *Data Reduction and Error Analysis for the Physical Sciences*, Wiley, New York, 1969.

Budinger, T. F. and G. T. Gullberg, Three-dimensional reconstruction in nuclear medicine emission imaging, *IEEE Trans. Nucl. Sci., NS-21*, 2, 1974.

Cormack, A. M., Representation of a function by its line integrals with some radiological applications, *J. Appl. Phys., 34*, 2722, 1963.

Fesen. C. G. and P. B. Hays, Two-dimensional inversion technique for satellite airglow data, *Appl. Opt., 21*, 3784, 1982.

Gordon, R., Bender, R. and G. T. Herman, Algebraic reconstruction techniques (ART) and three-dimensional electron microscopy and X-ray photography, *J. Theoret. Biol, 29*, 471, 1970.

Hays, P. B., Rusch, D. W., Roble, R. G., and J. C. G. Walker, The OI (6300Å) airglow, *Rev. Geophys. Space Sci., 16*, 225, 1978

Lloyd, N. D. and E. J. Llewellyn, Deconvolution of blurred images using photon counting statistics and maximum probability, *Can. J. Phys., 67*, 89, 1989.

McDade, I. C., Lloyd, N. D. and E. J. Llewellyn, A rocket tomography measurement of the N_2^+ 3914Å emission rates within an auroral arc, *Planet. Space Sci.*, in press, 1991.

Solomon, S. C., Hays, P. B. and V. J. Abreu, Tomographic inversion of satellite photometry, *Appl. Opt., 23*, 3409, 1984.

Solomon, S. C., Hays, P. B. and V. J. Abreu, Tomographic inversion of satellite photometry. Part 2, *Appl. Opt., 24*, 4134, 1985.

Solomon, S. C., Hays, P. B. and V. J. Abreu, The auroral 6300Å emission: observations and modelling, *J. Geophys. Res.*, *93*, 9867, 1988.

Thomas, R. J., and T. M. Donahue, Analysis of Ogo 6 observations of the OI 5577Å tropical nightglow, *J. Geophys. Res.*, *77*, 79, 1977.

Wasser, B. and T. M. Donahue, Atomic oxygen between 80 and 120 km: Evidence for a latitudinal variation in vertical transport near the mesopause, *J. Geophys. Res.*, *84*, 1297, 1979.

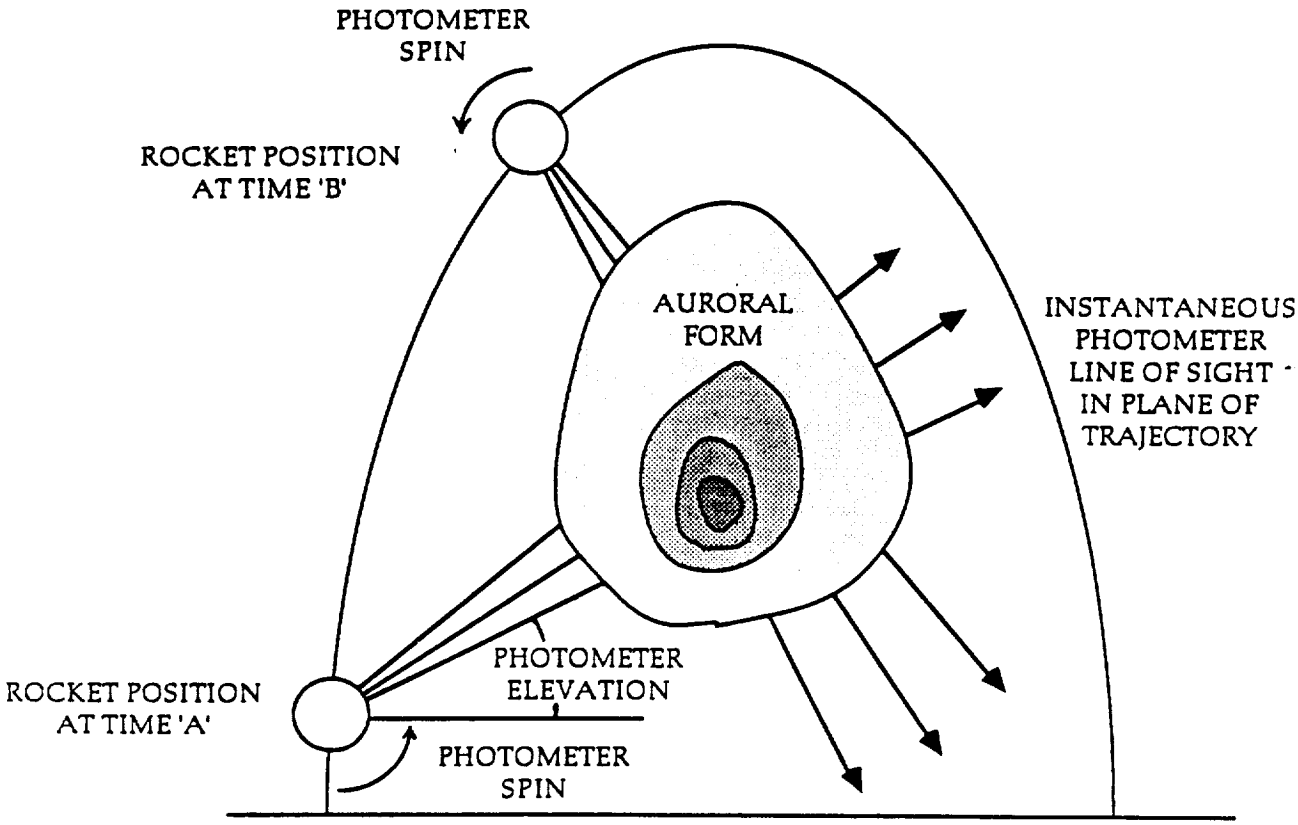

Fig. A1. Sketch illustrating how a rocket photometer operating in a spin scan mode would be used to make tomographic auroral brightness measurements in the plane of the rocket trajectory.

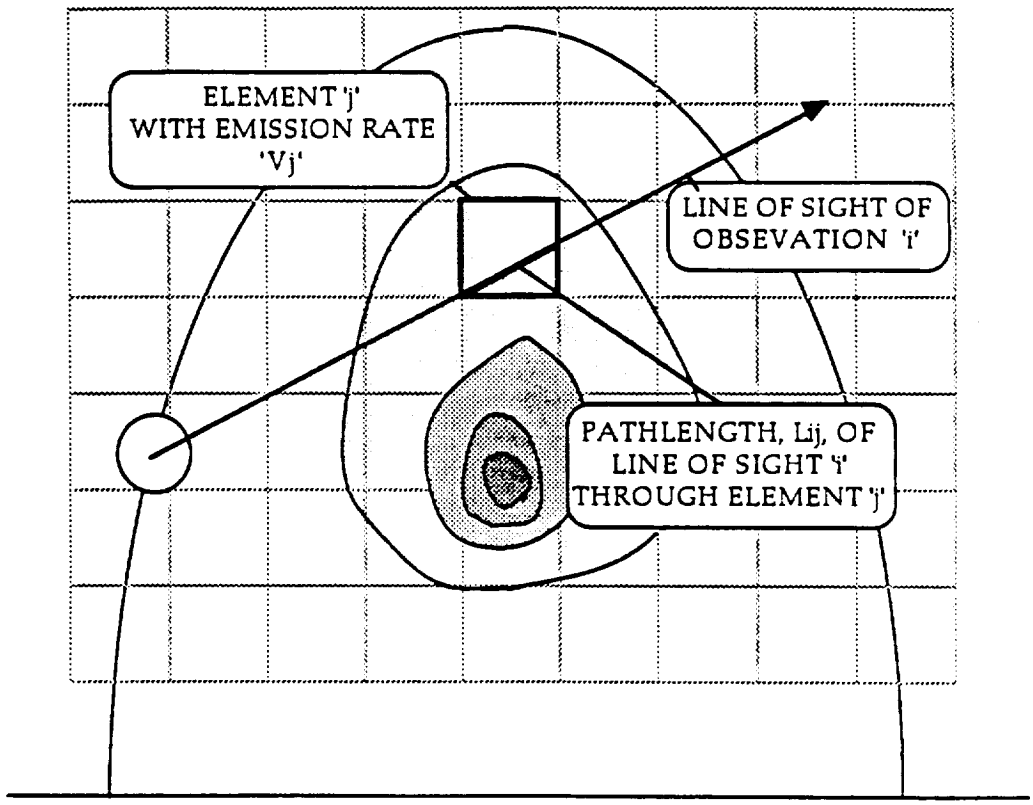

Fig. 2. Sketch illustrating the fundamentals of the algebraic reconstruction approach. The size of the reconstruction elements is greatly exaggerated.

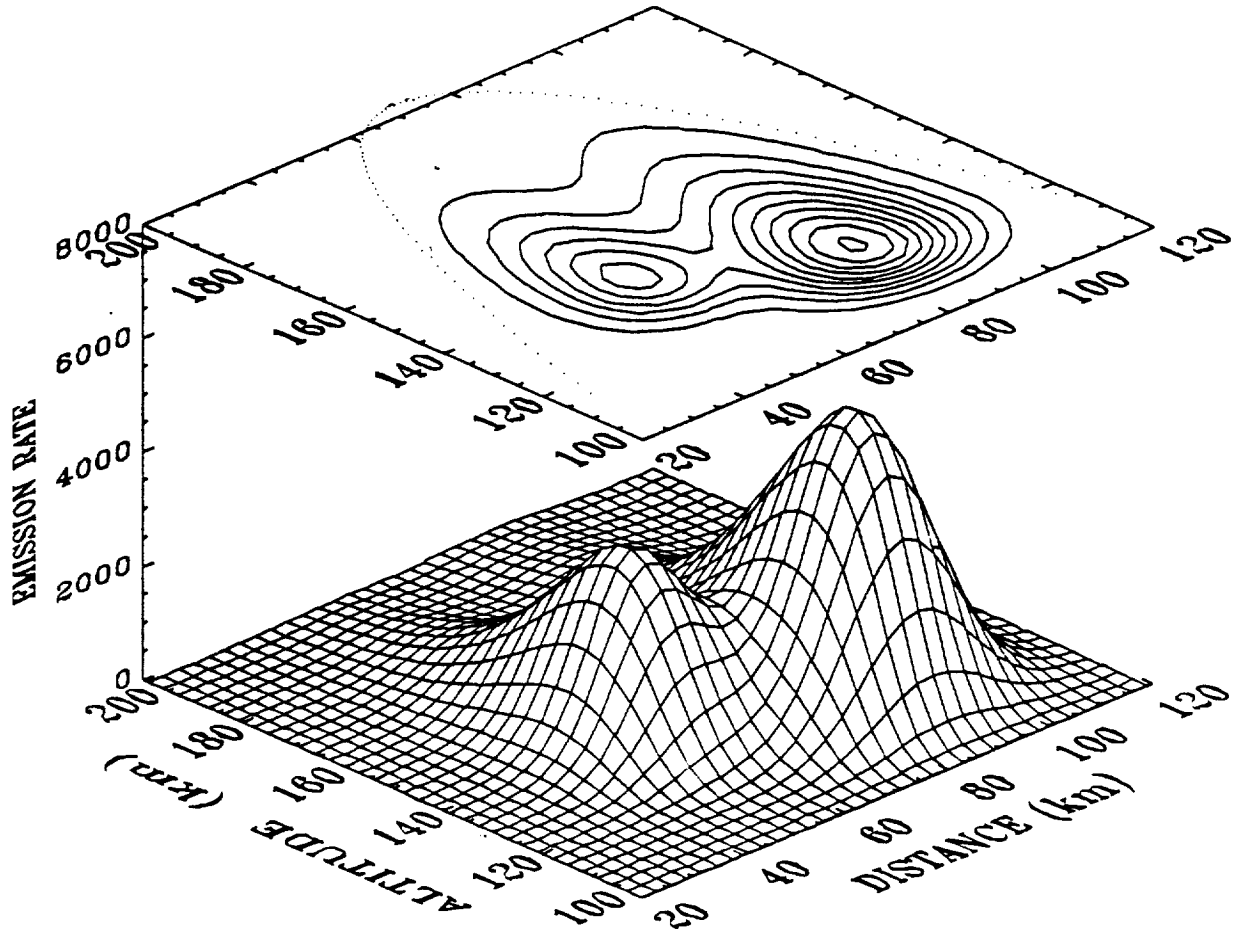

Fig A3. Surface and contour plot of the 'true' auroral emission rates used for some of the tests described in the text. The emission rates are expressed in units of photons cm^{-3} sec^{-1} and the contour lines are drawn at equal intervals of 500 photons cm^{-3} sec^{-1}. The zenith intensity through the core of the aurora is ~15 kR and the form would correspond to an IBC2 aurora if the emission feature was the $O(^1D\text{-}^1S)$ 5577Å greenline. The emission rates outside of the plotted region were essentially equal to zero. The dotted curve projected onto the contour plot shows the rocket flight trajectory.

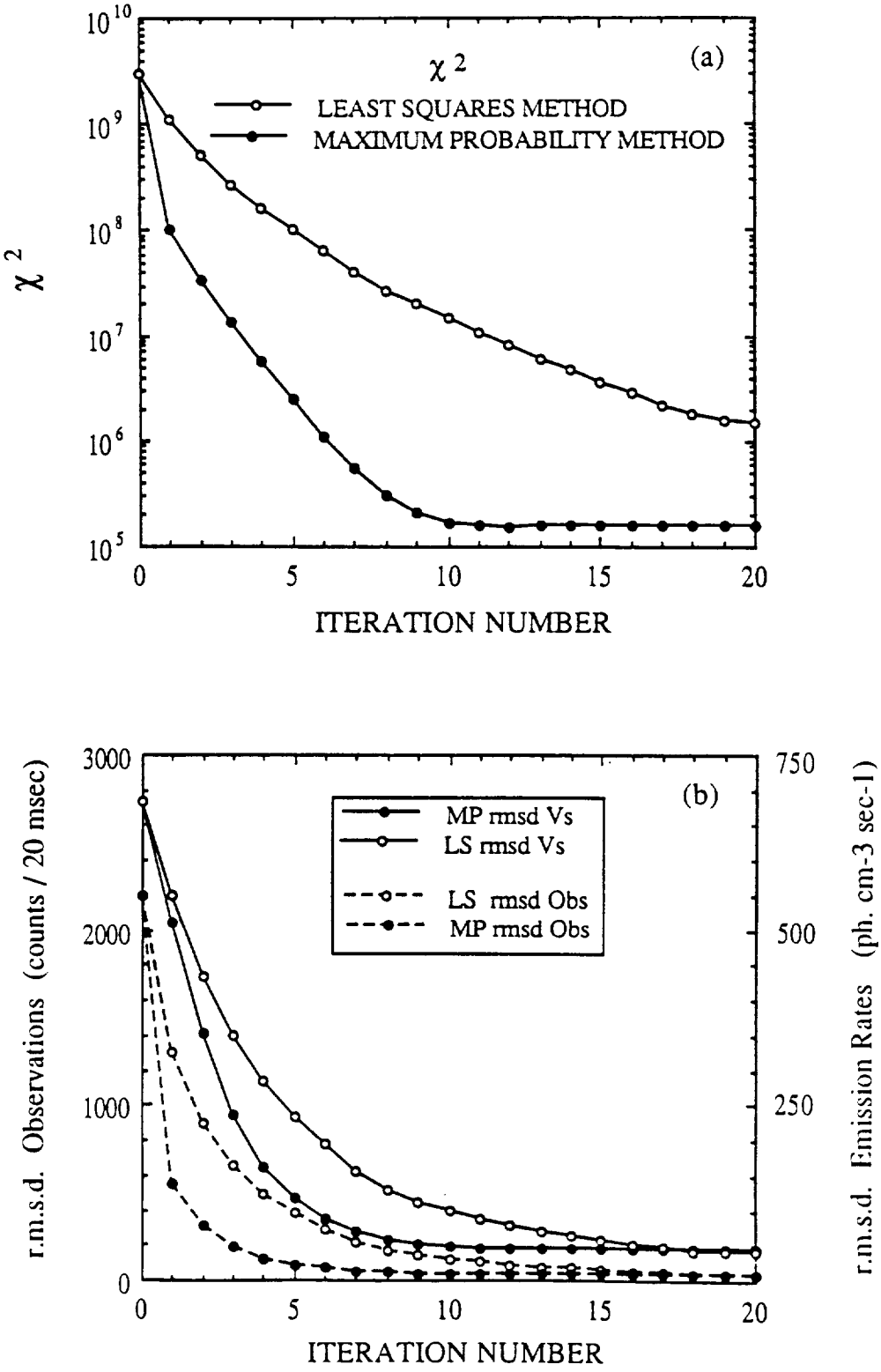

Fig.4. The variation in (a) χ^2, and (b) *rmsd Obs* and *rmsd Vs* during the 'maximum probability' (MP) and 'least squares' (LS) inversions of the noise-free test data described in the text.

'MAXIMUM PROBABILITY' RECOVERY FROM 'NOISE-FREE' DATA

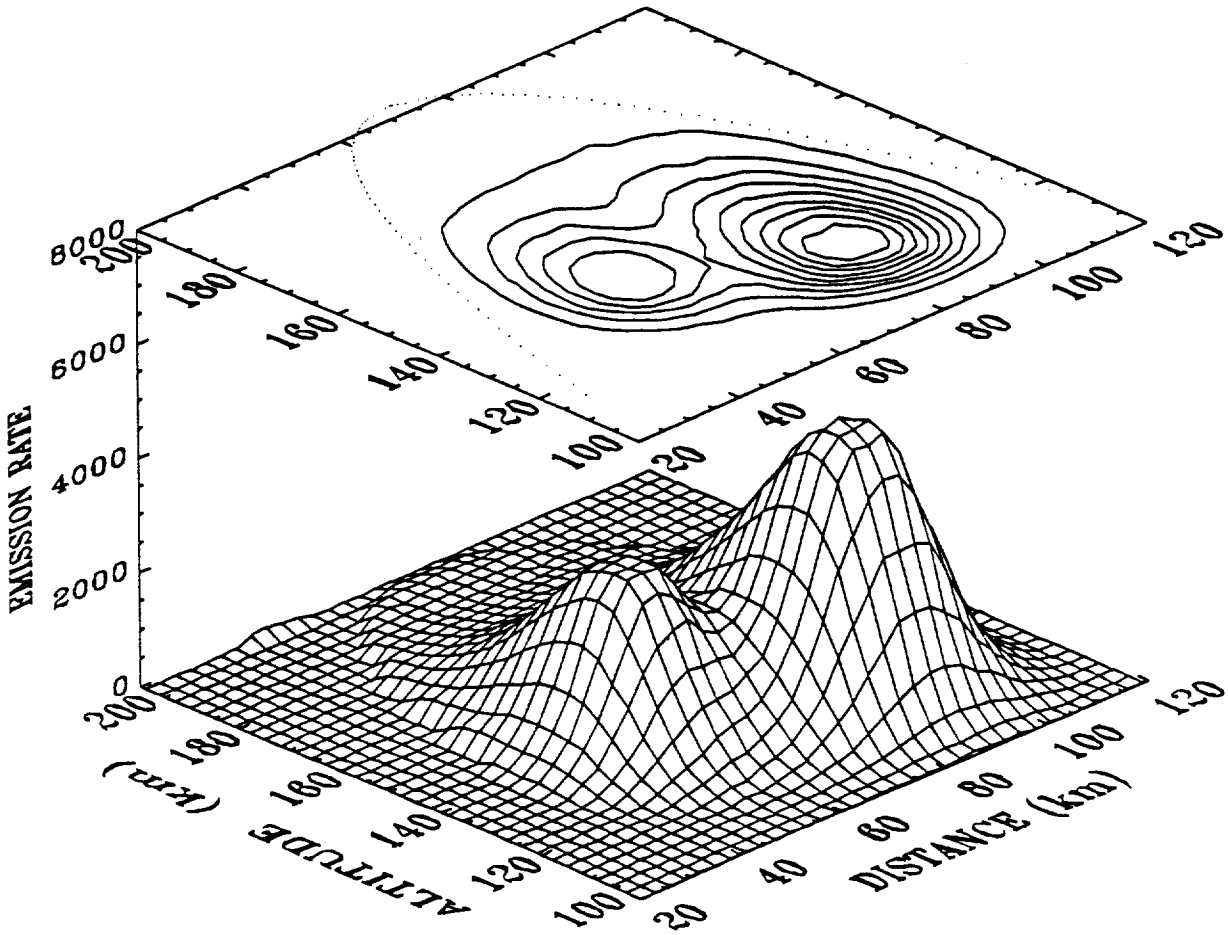

Fig. 5. The auroral emission rate distribution recovered at the end of the 12th iteration of the 'maximum probability' inversion of the 'noise-free' test data described in the text. This recovered distribution should be compared with the 'true' distribution shown in Figure 3. The emission rates are expressed in units of photons cm^{-3} sec^{-1} and the contour lines are drawn at equal intervals of 500 photons cm^{-3} sec^{-1}. The emission rates recovered for the elements lying outside of the plotted region were essentially zero.

'LEAST SQUARES' RECOVERY FROM 'NOISE-FREE' DATA

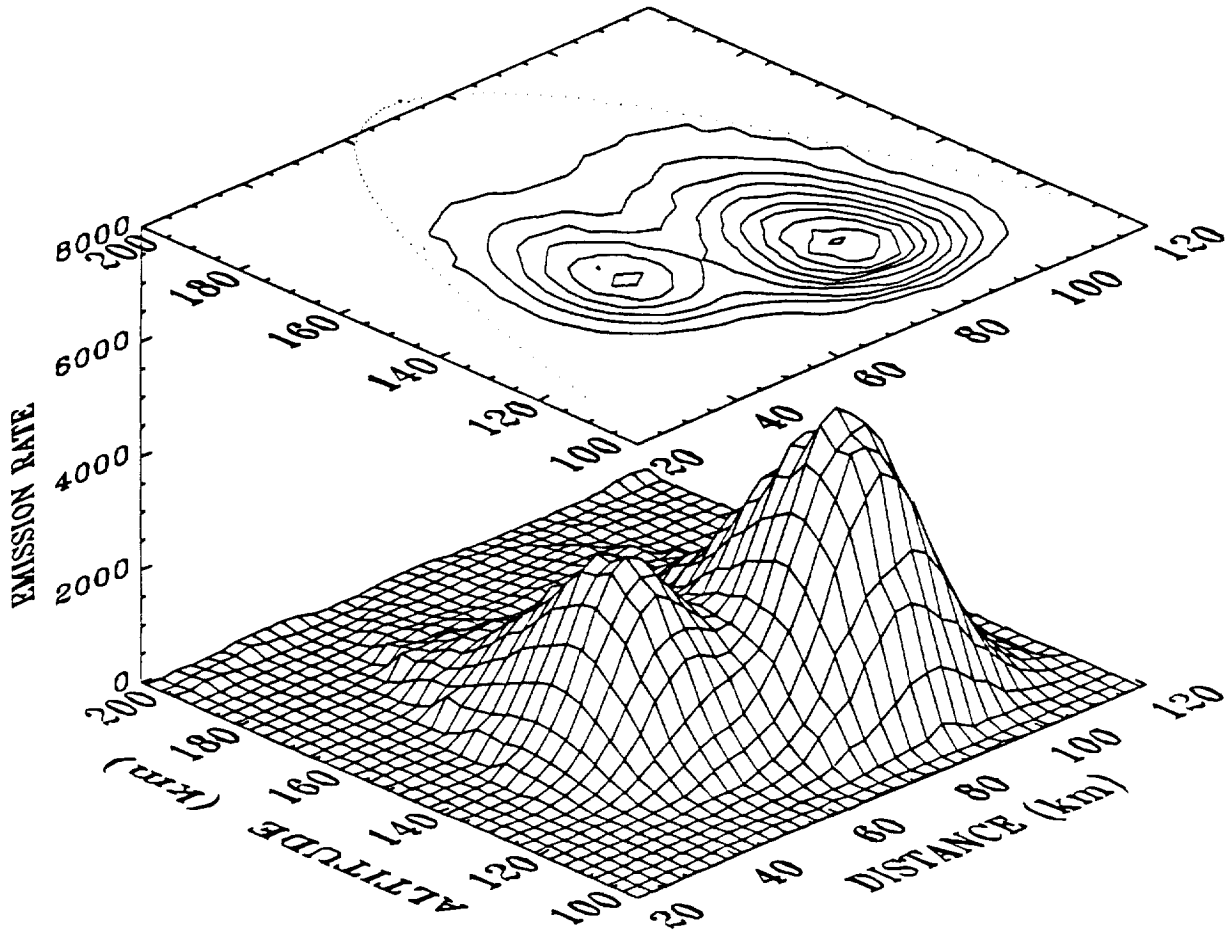

Fig 6. The auroral emission rate distribution recovered at the end of the 18th iteration of the 'least squares' inversion of the 'noise-free' test data described in the text. This recovered distribution should be compared with the 'true' distribution shown in Figure 3. The emission rates are expressed in units of photons cm^{-3} sec^{-1} and the contour lines are drawn at equal intervals of 500 photons cm^{-3} sec^{-1}. The emission rates recovered for the elements lying outside of the plotted region were essentially zero.

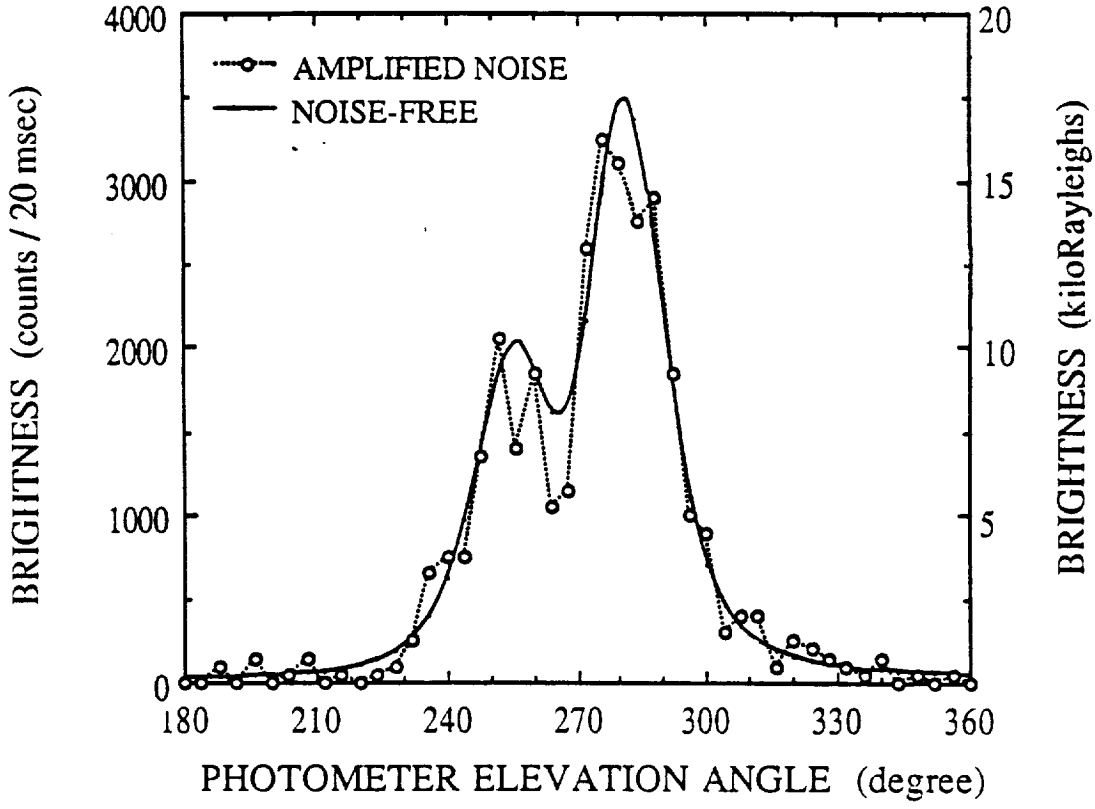

Fig. 7. Examples of the 'noise-free' and 'amplified noise' simulated observations described in the text. These observations represent the downward viewing half of a scan made at apogee and were generated from the test distribution and trajectory shown in Figure 3.

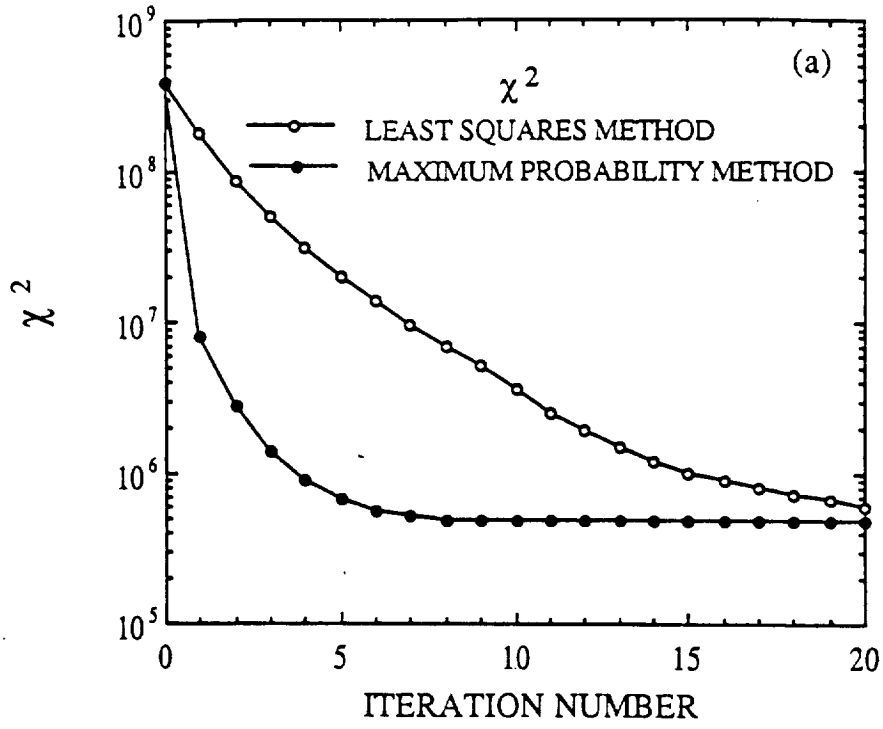

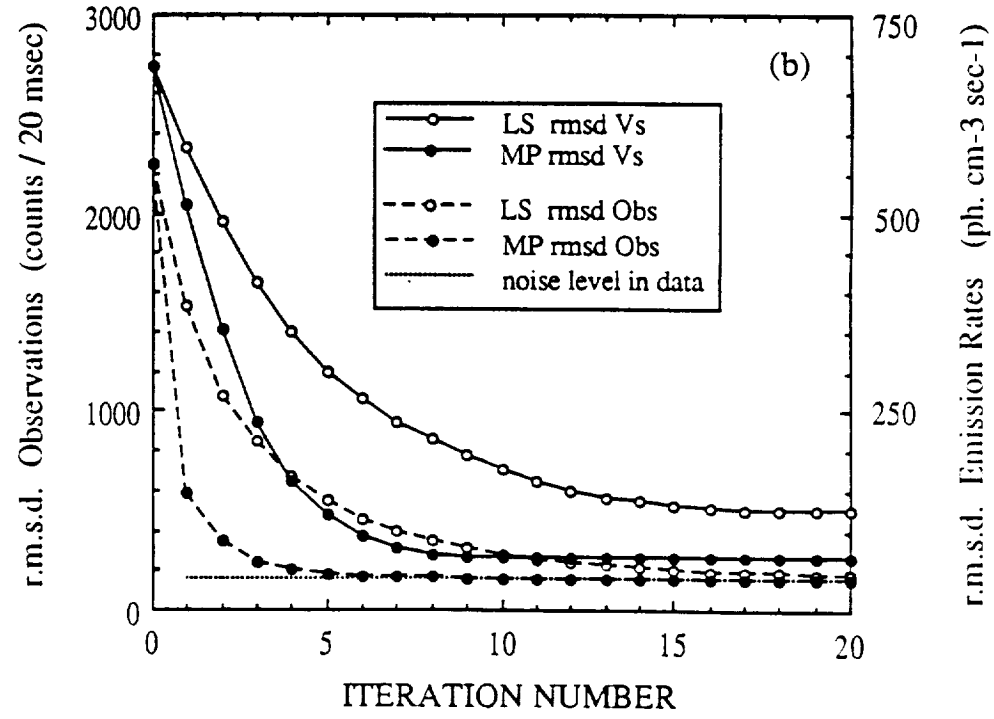

Fig 8. The variation of (a) χ^2 and (b) *rmsd Obs* and *rmsd Vs* recorded during the 'maximum probability' (MP) and 'least squares' (LS) inversions of the 'amplified noise' simulation described in the text. The horizontal dashed line in panel (b) shows the root mean square difference between the 'noise-free' and 'amplified noise' simulations.

'MAXIMUM PROBABILITY' RECOVERY FROM 'AMPLIFIED NOISE' DATA

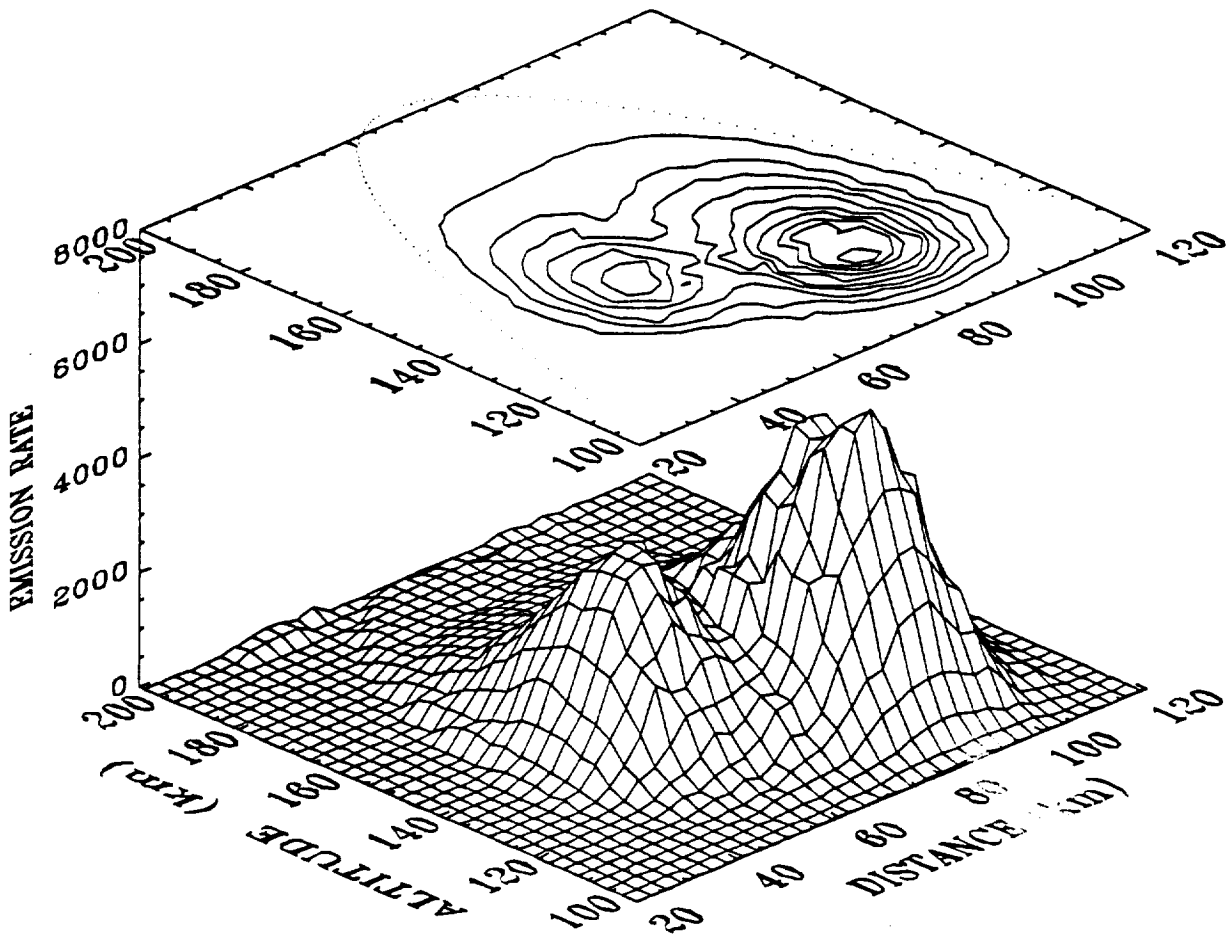

Fig9. The auroral emission rate distribution recovered at the end of the 12th iteration of the 'maximum probability' inversion of the 'amplified noise' test data described in the text. This recovered distribution should be compared with the 'true' distribution shown in Figure 3. The emission rates are expressed in units of photons cm^{-3} sec^{-1} and the contour lines are drawn at equal intervals of 500 photons cm^{-3} sec^{-1}. The emission rates recovered for the elements lying outside of the plotted region were essentially zero.

'LEAST SQUARES' RECOVERY FROM 'AMPLIFIED NOISE' DATA

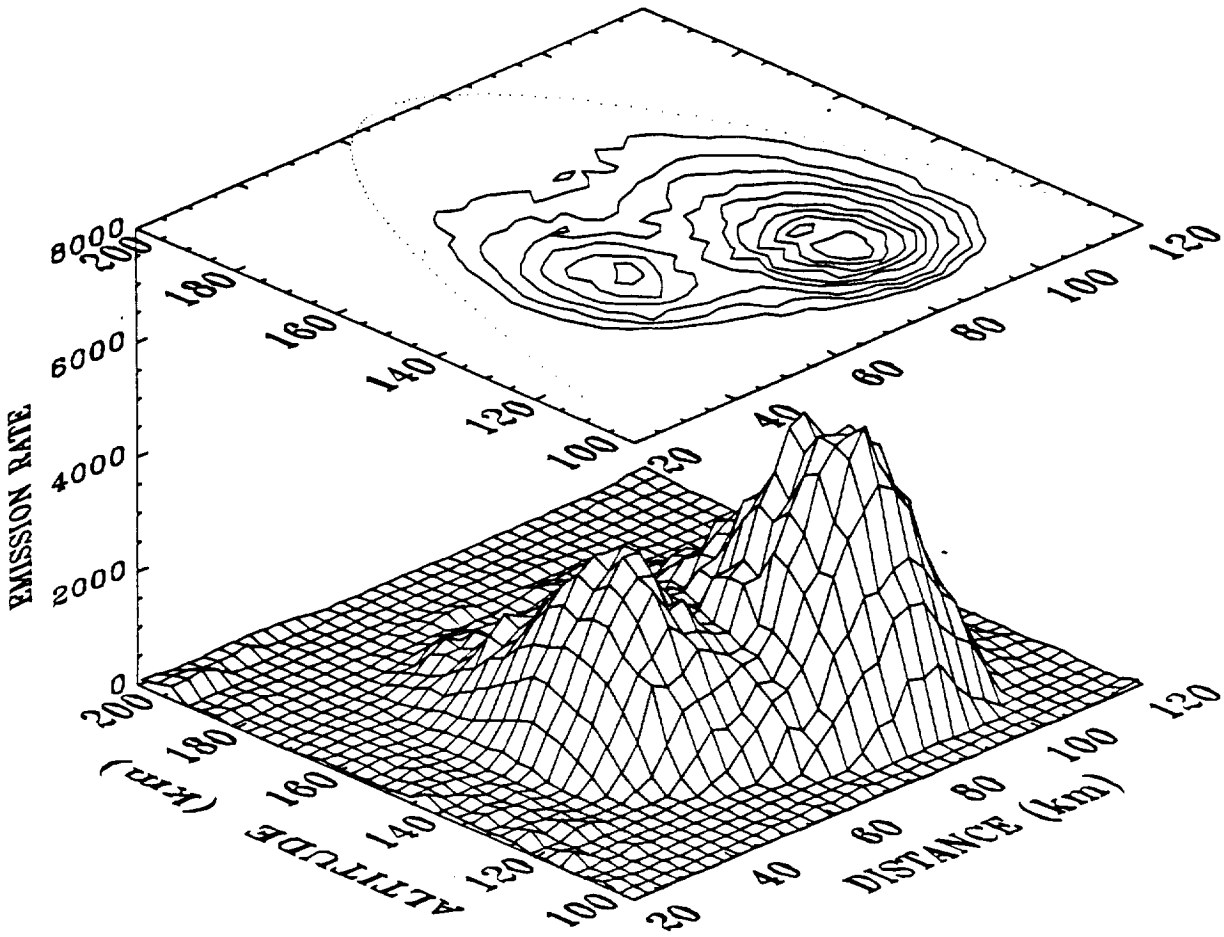

Fig A10. The auroral emission rate distribution recovered at the end of the 18th iteration of the 'least squares' inversion of the 'amplified noise' observations described in the text. This recovered distribution should be compared with the 'true' distribution shown in Figure 3. The emission rates are expressed in units of photons cm^{-3} sec^{-1} and the contour lines are drawn at equal intervals of 500 photons cm^{-3} sec^{-1}. The emission rates recovered for the elements lying outside of the plotted region were essentially zero.

AURORAL PENETRATION TEST DISTRIBUTION

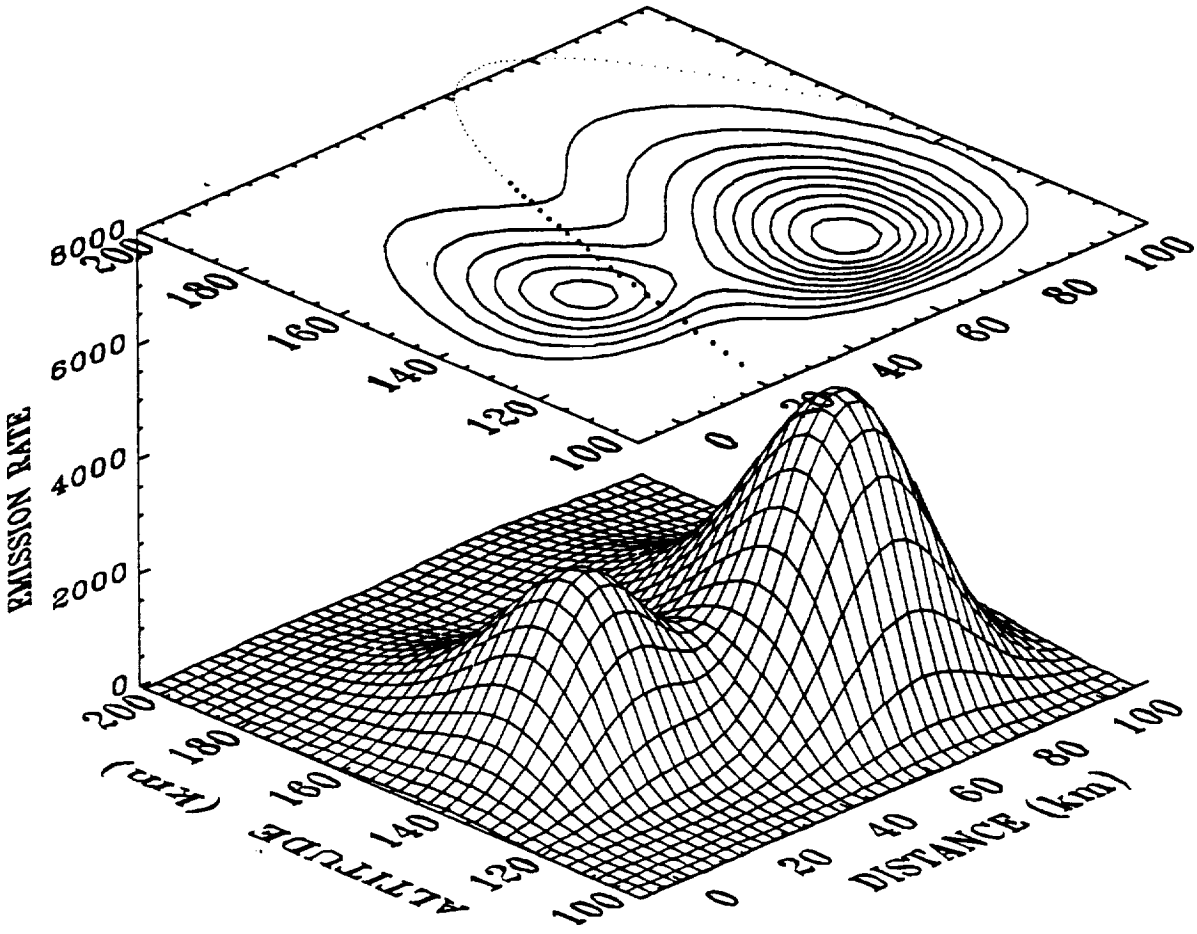

Fig A11. The 'true' auroral emission rates and the rocket flight trajectory used to investigate the effects of rocket penetration of the auroral form. The emission rates are expressed in units of photons cm^{-3} sec^{-1} and the contour lines are drawn at equal intervals of 500 photons cm^{-3} sec^{-1}. The dotted curve projected onto the contour plot shows the rocket flight trajectory.

AURORAL PENETRATION RECOVERED DISTRIBUTION

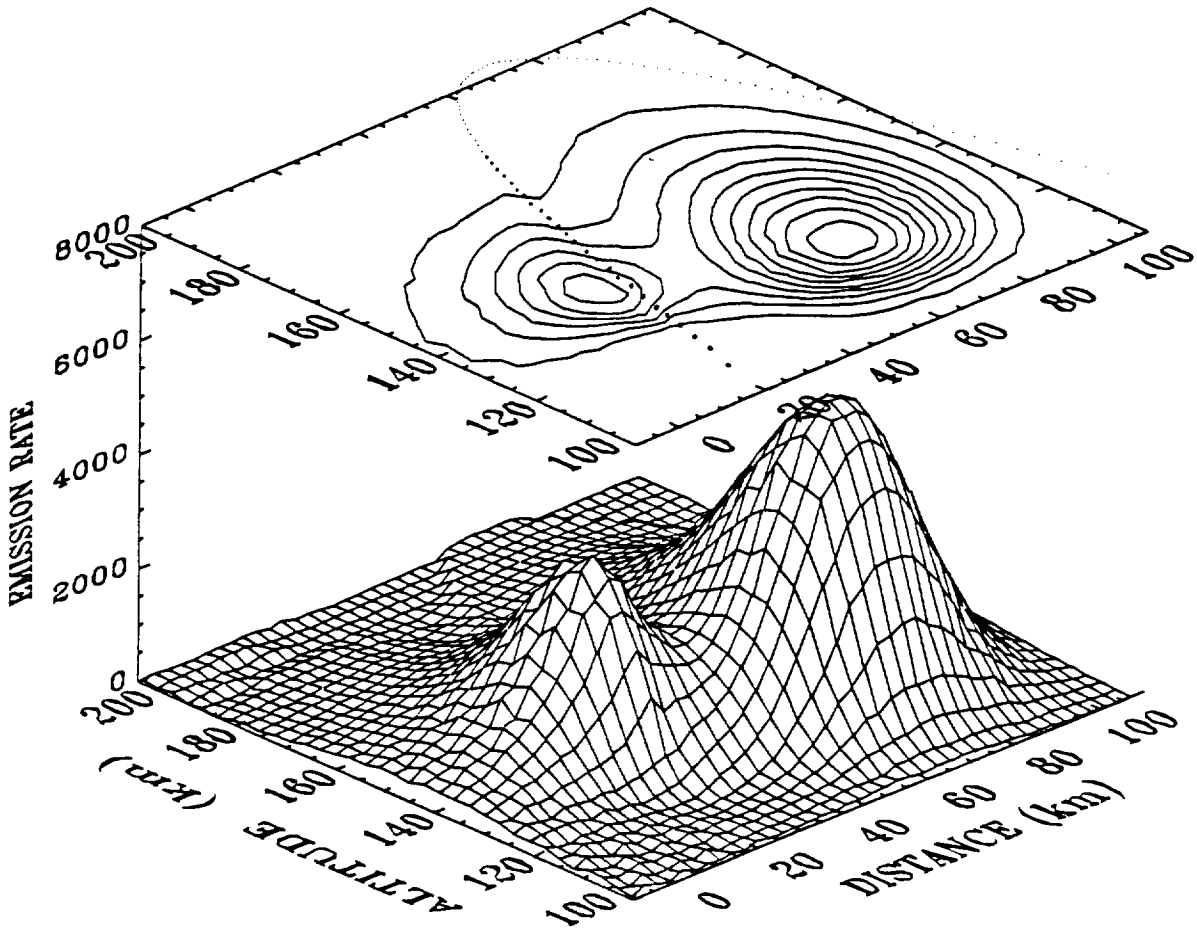

Fig. 12. The emission rate distribution recovered at the end of the 12th iteration of the 'maximum probability' inversion of the data simulating rocket penetration of the auroral form. This recovered distribution should be compared with the 'true' distribution shown in Figure 11. The contour lines are drawn at equal intervals of 500 photons cm^{-3} sec^{-1}. The dotted curve projected onto the contour plot shows the rocket flight trajectory.

STANDARD INVERSION OF SMEARED DATA

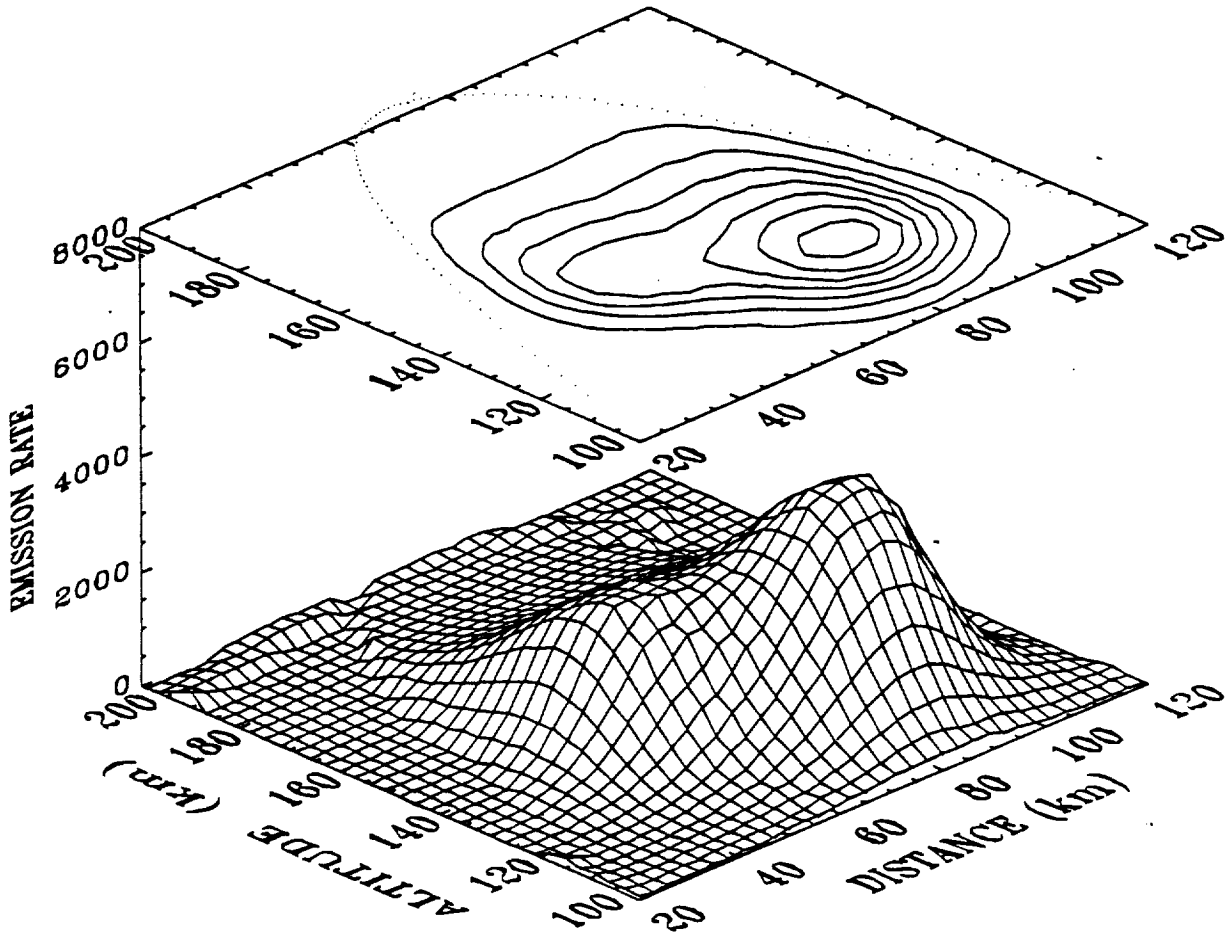

Fig. 13. The emission rate distribution recovered at the end of the 12th iteration of the standard 'maximum probability' inversion of the simulated observations that were smeared with an effective field of view of 20° FWHM. This recovered distribution should be compared with the 'true' distribution shown in Figure 3. The contour lines are drawn at equal intervals of 500 photons cm^{-3} sec^{-1}.

'FIELD WEIGHTED WEIGHTS' INVERSION OF SMEARED DATA

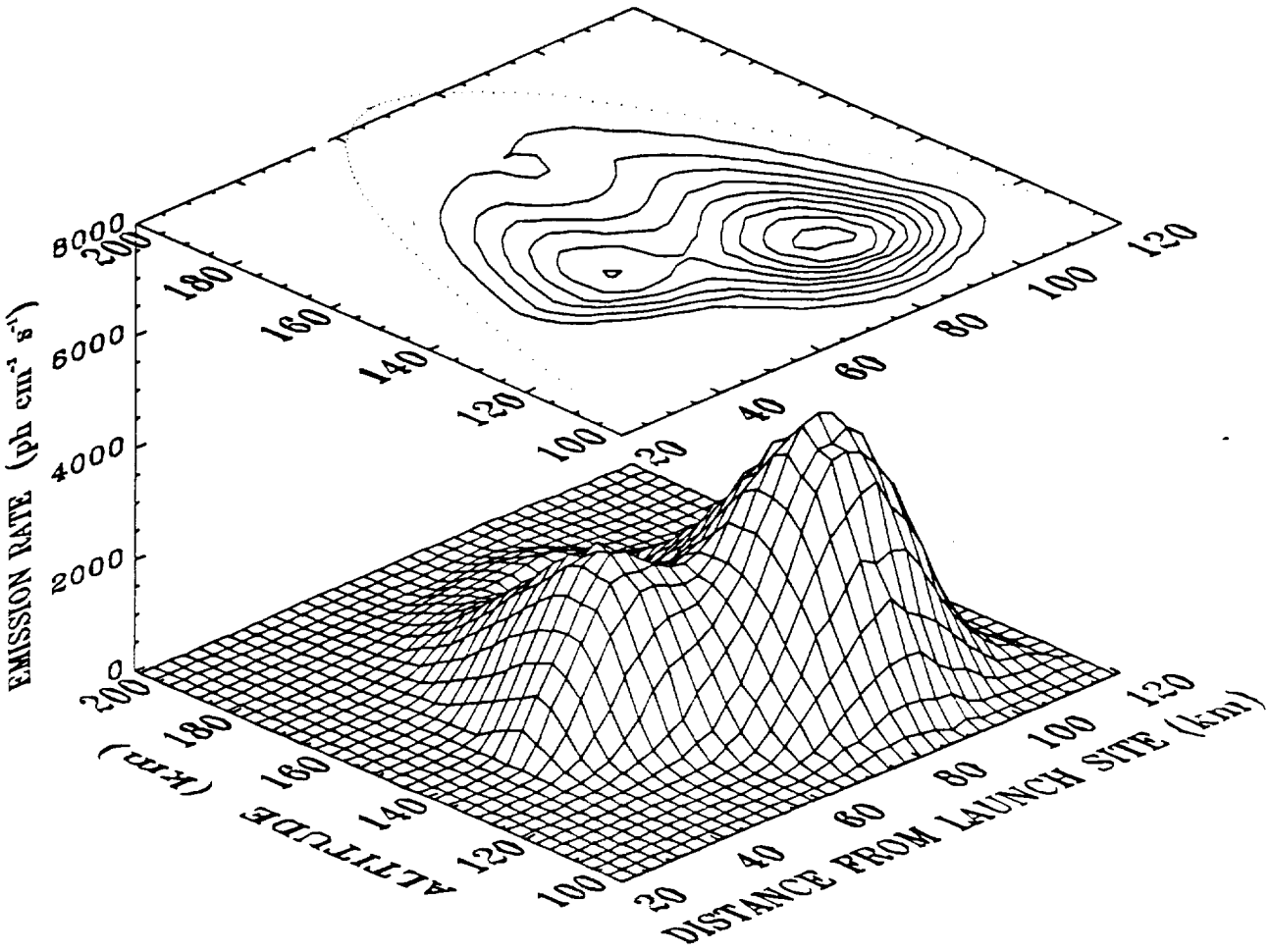

Fig A14. The emission rate distribution recovered at the end of the 12th iteration of the 'field weighted weights' 'maximum probability' inversion of the simulated observations that were smeared with an effective field of view of 20° FWHM. This recovered distribution should be compared with the 'true' distribution shown in Figure 3 and the standard recovery shown in Figure 13. The contour lines are drawn at equal intervals of 500 photons cm^{-3} sec^{-1}.

'TRUE' DISTRIBUTIONS IN TIME-DEPENDENT AURORA

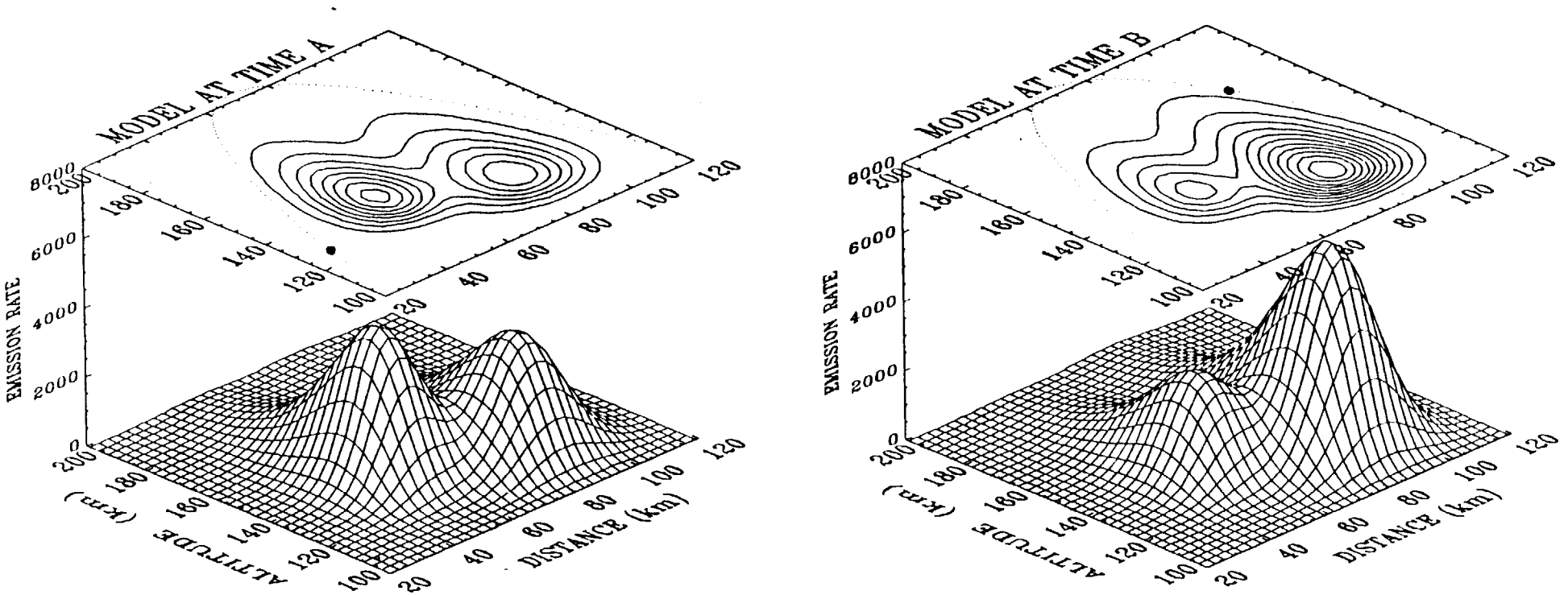

Fig. 15. The 'true' emission rate distributions at two specific times during the time dependent aurora simulation described in the text. Panel (a) shows the 'true' distribution when the rocket was at an altitude of ~125 km on the upleg, panel (b) shows the 'true' distribution when the rocket was at ~170 km on the downleg. The contour lines are drawn at equal intervals of 500 photons cm^{-3} sec^{-1}.

'RECOVERED' DISTRIBUTIONS IN TIME-DEPENDENT AURORA

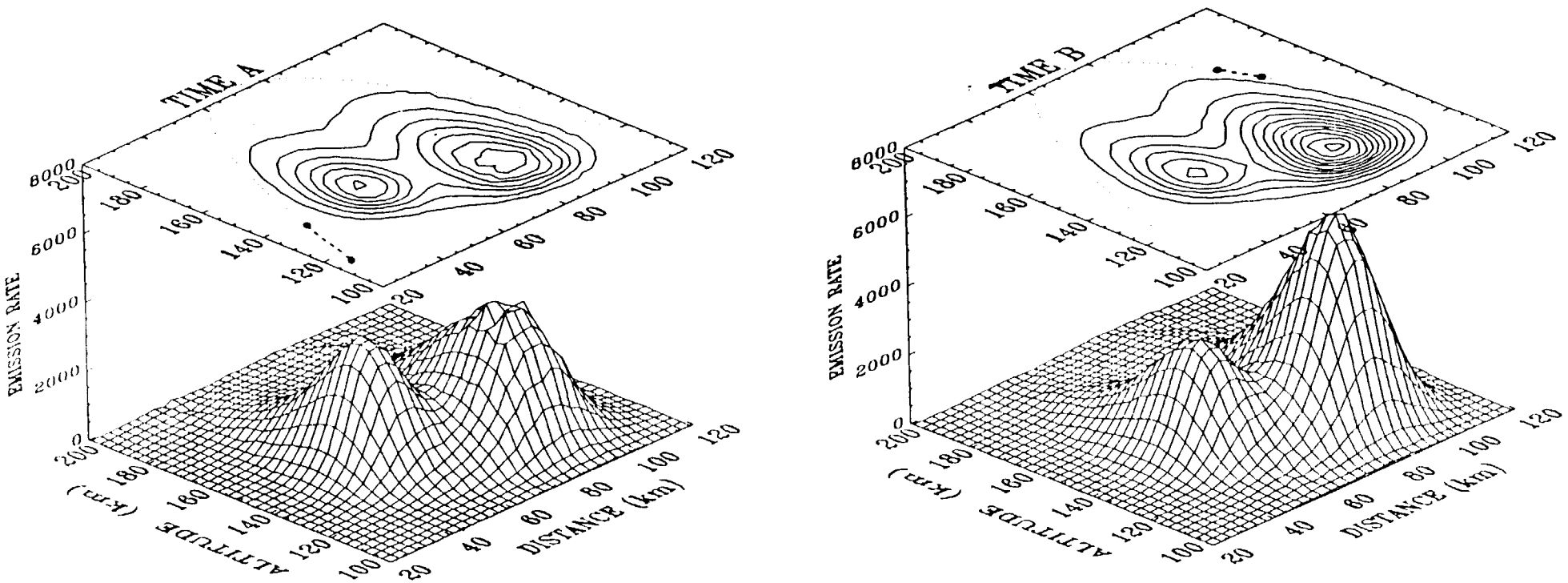

Fig. 16. The emission rate distributions recovered after the 4th iteration of the 'maximum probability' inversions of two 15 second segments of the simulated observations generated for the time dependent aurora. The inversions were initiated with the mean distribution described in the text. The two segments of the data correspond to the observations made between (a) 115 and 134 km on the upleg and (b) 175 and 163 km on the downleg. These distributions should be compared with the 'true' distributions shown in Figure 15. The contour lines are drawn at equal intervals of 500 photons cm^{-3} sec^{-1}.

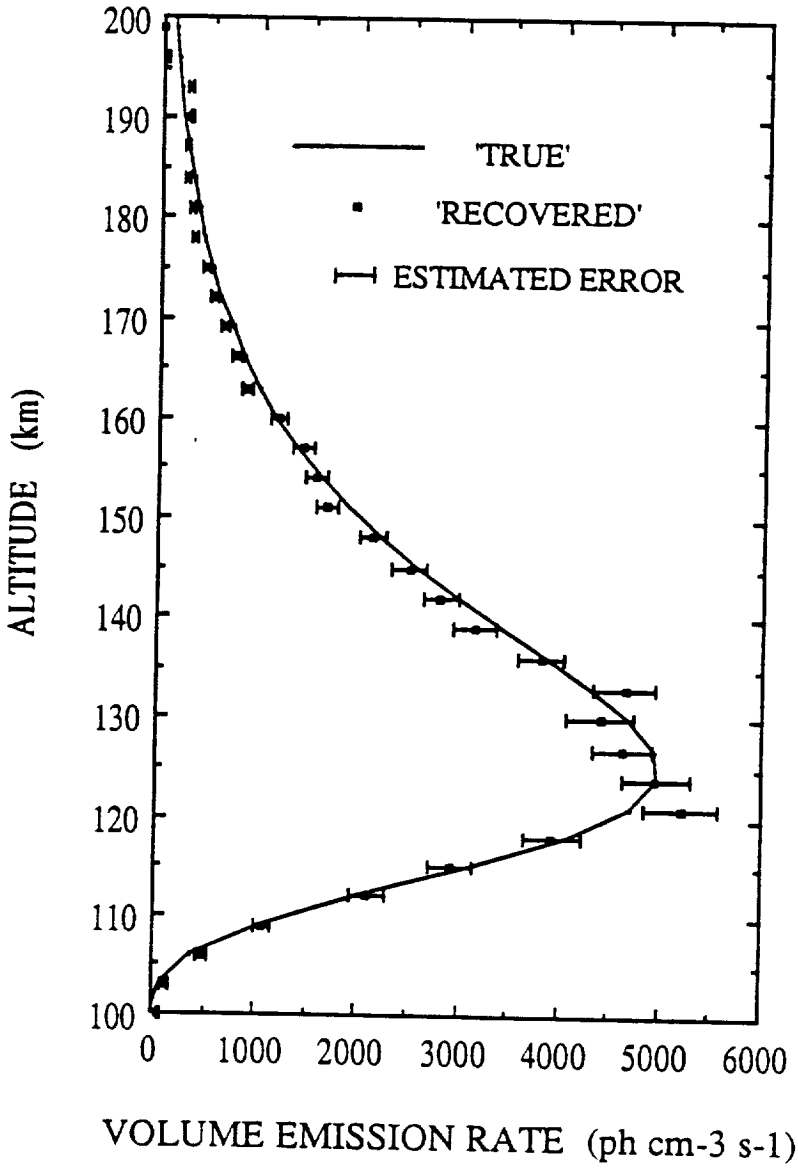

Fig.A17. Illustration of the relationship between the 'true' emission rates, the 'recovered' emission rates, and the estimated uncertainties in the 'maximum probability' recovery. The 'true' and 'recovered' emission profiles are vertical slices through the 'true' and 'recovered' distributions shown in Figures 3 and 9 passing through the 'true' emission maximum. The error bars show the confidence intervals that would be expected on the basis of 2× the σ_{V_j} given by equation (12).

THE ANALYSIS OF A ROCKET TOMOGRAPHY MEASUREMENT OF THE N_2^+ 3914Å EMISSION AND N_2 IONIZATION RATES IN AN AURORAL ARC

NASA Grant No. NAG5-670

FINAL REPORT

APPENDIX 'B'

"A Rocket Tomography Measurement of the N_2^+ 3914Å Emission Rates within in an Auroral Arc"

I. C. McDade
Space Physics Research Laboratory
Department of Atmospheric, Oceanic and Space Sciences
University of Michigan

and

N. D. Lloyd and E. J. Llewellyn
Institute of Space and Atmospheric Studies
Department of Physics, University of Saskatchewan

Accepted for publication in *Planetary and Space Science*, 1991.

Abstract - A rocket tomography experiment designed to measure the 2-dimensional distribution of the N_2^+ 3914Å volume emission rates within an auroral arc is described. A simple filter photometer on board a sounding rocket, which was launched during the ARIES auroral campaign, was used to measure the 3914Å auroral brightnesses at elevation angles ranging from 0^o to 360^o in the plane of the rocket trajectory. The measured auroral brightnesses have been tomographically inverted to recover the local 3914Å volume emission rates as a function of both altitude and latitude within the arc. The tomographic inversion procedure, which is based upon a maximum probability algebraic reconstruction approach, is described and the implications of the results for studies of auroral excitation processes are briefly discussed.

1. INTRODUCTION

During February of 1984 a major international field campaign, known by the acronym ARIES and described in more detail by Vallance Jones *et al.* (1990), was carried out from northern Manitoba, Canada, to study auroral excitation processes. As part of this campaign a Black Brant sounding rocket, equipped with various particle detectors and optical instruments, was launched towards and over an east-west aligned auroral arc. A major goal of the rocket borne experiments, and coordinated ground-based observations, was to obtain information about the internal structure of such an auroral form. In this paper we present the results of one of the rocket experiments which was designed to measure the volume emission rates of the $N_2^+(B^2\Sigma_u^+\text{-}X^2\Sigma_g^+)$ first negative (0-0) band as a function of both altitude and latitude within the arc.

2. THE ROCKET OBSERVATIONS

The ARIES 'B' rocket (ADD VC-10), from which the present observations were made, was launched from Churchill Rocket Range (58.7°N, 266.2°E) at 03:53:44 UT on 28 February 1984. The rocket was launched southwards over an east-west aligned auroral form along a trajectory that was nearly coincident with the local magnetic meridian. At 3:57:37 UT the vehicle reached its 203 km apogee 72 km downrange from the launch site. At an altitude of 75 km on the flight upleg a vehicle manœuver was initiated to orientate the rocket roll axis so that it would be perpendicular to the horizontal and vertical components of the local magnetic field. The desired vehicle attitude was achieved, to a good approximation, at an altitude of 118 km and maintained throughout the rest of the flight until the rocket began to tumble upon re-entry at an altitude of ~70 km. During the period of controlled flight the rocket was spinning about the roll axis with a period of 0.405 seconds. The filter photometer used to make the N_2^+ 3914Å measurements was a photon

counting device of conventional design with a half-cone field of view of 2.5°. The photometer was mounted in a side-look configuration with its optical axis perpendicular to the rocket roll axis. During each rocket roll, therefore, the line of sight of the photometer essentially scanned through elevation angles ranging from 0° to 360° in a plane that was nearly coincident with the plane of the trajectory and perpendicular to the east-west aligned auroral form. The photometer counts were recorded at a frequency of 200Hz (5 msec bins) and this resulted in a ±2.2° smear in the measured brightnesses; this smear was comparable to that of the photometer field of view. The filter transmission function was 50Å wide (FWHM), peaked at 3915Å and captured between 90% and 93% of the $N_2^+(B^2\Sigma_u^+ - X^2\Sigma_g^+)$ (0-0) band over the range of rotational temperatures expected at auroral altitudes. The sensitivity of photometer was calibrated before the flight using a standard low brightness source; this procedure provided a calibration factor of 13 counts sec^{-1} per Rayleigh of $N_2^+(B^2\Sigma_u^+ - X^2\Sigma_g^+)$ (0-0) band emission. Unfortunately, a post-flight calibration check could not be performed because the instrument was seriously damaged upon re-entry and impact. However, a comparison of the measurements made along similar lines of sight from the ground and from the rocket indicates that the rocket photometer must have been approximately 3 times more sensitive during the flight than the calibration had suggested. Although no errors have been found in the original calibration calculations we have tentatively adopted a revised calibration factor of 39 counts sec^{-1} per Rayleigh.

The 3914Å photometer provided good data from rocket altitudes of 180 km on the flight upleg to approximately 70 km on the downleg. For reasons discussed below, this paper will focus mainly on the measurements that were made between rocket altitudes of ~190 km and ~80 km on the downleg of the flight. This data is summarized in Fig.1 which shows a shifted stack plot of the measured brightnesses as a function of photometer elevation for a number of consecutive roll scans. Fig.1 illustrates that when the rocket was

at 200 km most of the auroral emission originated from below the rocket in the northern and southern-nadir quadrants. As the rocket descended through the 200 km to 140 km region one feature labelled N in Fig.1 moved away from the nadir (elevation 270°), passed through the north horizontal viewing direction (elevation 180°) and finally merged with a broader feature apparently developing in the zenith (elevation 90°). During this period a more southerly feature (labelled S in Fig.1) simply faded as the broad feature in the zenith developed. The elevations of the two other prominent features in Fig.1, labelled A and B, varied only slightly during the flight; as the rocket descended feature A drifted slowly towards the north horizontal (elevation 180°) and feature B broadened and moved towards, and through, the south horizontal (elevation 360°). It will be demonstrated below that the features A and B in Fig.1 arose from latitudinally extended auroral, or nightglow, sources viewed in a limb enhanced mode, and that the features N and S arose from the more localized auroral sources of 3914Å emission.

Although it is not perhaps immediately apparent, the data shown in Fig.1 do contain a great deal of information about the spatial distribution and temporal variations of the 3914Å emission rates within the auroral arc. For example, if temporal variations are neglected, then a simple triangulation analysis, illustrated in Fig.2, would suggest that the feature labelled S in Fig.1 probably arose from a southerly auroral core at an altitude close to 130 km, and that the feature N in Fig.1 arose from a more northerly core at higher altitude. In the following analysis we demonstrate how quantitative information about the spatial distribution and the temporal variations of the N_2^+ 3914Å emission rates within the arc may be extracted from the observational data.

3. A TOMOGRAPHIC INVERSION OF THE ROLL SCAN MEASUREMENTS

Several tomographic inversion techniques have been developed to deal with the problem of recovering 2-dimensional volume emission rate distributions from surface brightness measurements made under conditions similar to those of the ARIES rocket experiment. The most successful tomographic techniques fall into two main categories; those based on 2-dimensional algebraic reconstruction and those based on 2-dimensional filtered transform methods. An algebraic reconstruction technique was first applied to aeronomic observations by Thomas and Donahue (1977) in their analysis of OGO-6 satellite data and techniques based on filtered transform methods have been used in the analysis of Atmospheric Explorer satellite data (Solomon *et al.*, 1984; 1985; 1988). In the present work we have applied an algebraic reconstruction technique which allows for the Poisson noise associated with the photometer photon counting statistics. As with other algebraic reconstruction techniques, the relevant region of the atmosphere is divided into a number of volume elements. Within each element the photon emission rate is assumed to be uniform and isotropic, and the surface brightness observed in a particular direction is assumed to be the sum of the contributions from all elements which intersect the line of sight. The number of elements is chosen so that the problem is overdetermined i.e. the number of elements for which volume emission rates are to be recovered is less than the total number of different line of sight observations. From a consideration of the changing viewing geometry during the flight a system of linear equations is generated from the observational data set. This system of equations, which will not neccesarily be consistent because of noise in the photometric data, is 'solved' in the present work using a maximum probability approach to provide a best estimate of the volume emission rate distribution.

3.1. *Geometry of the contributing elements*

In order to achieve a successful inversion of the observations the array of volume elements that are allowed to contribute to the observed brightnesses must be carefully selected. For the analysis of the ARIES rocket data a primary array of 3075 elements was located within a rectangular grid which conservatively enclosed the main auroral form as determined from ground-based observations. This grid was divided into 75 columns and 41 rows of square elements with sides of 3 km. This grid lay in the plane of the rocket trajectory which was, to a good approximation, coincident with the plane of the photometer scan. The coordinate system of the grid was in the same frame as the rocket radar trajectory data i.e. the rows and columns of the grid were parallel to the local horizontal and vertical directions at the launch site. Within this reference frame the primary grid enclosed the region of space lying between 80.5 km and 203.5 km in altitude and extended from 18.5 km downrange to 243.5 km downrange of the launch site; this corresponds to approximately 2^{o} of ground latitude. To extend this primary array to an altitude of ~215 km, where only weak emission is anticipated, an additional row of 75 rectangular elements each 12 km high and 3 km wide was placed on top of the primary grid. Since regions of space located well beyond the primary grid limits were viewed during each photometer scan, contributions from distant auroral or airglow sources of 3914Å emission must be considered. In addition, the photometer line of sight intersected the solid earth for many (~45%) of the observations made during each scan and so contributions from the ground and tropospheric albedo must also be taken into account.

Clearly, allowance for the more distant sources of 3914Å emission cannot be made by simply extending the primary grid *ad infinitum* and a compromise has to be found between extending the grid and ensuring that the problem remains overdetermined. This compromise was achieved by assuming that the contributions from any distant sources

could be modelled as having arisen from stratified airglow layers. The contributions from these layers were assigned to an additional 72 spatial elements. Each element was represented by a 3 km thick earth centered annulus; 36 of these annuli were located to the north of the primary grid and 36 to the south. The altitudes represented by the annuli ranged from 80.5 km to 188.5 km.

To allow for the albedo contributions it has been assumed that the snow covered surface and lower atmosphere behaved like a Lambertian surface. The ground lying in the plane of the photometer scan between 5° north and 5° south of the centre of the primary grid was divided equally into 150 ground element bins; each ground bin was therefore approximately 7 km wide. It should be recognized that from an altitude of ~150 km the solid earth horizon is displaced from the rocket position by ~12° in ground latitude. Consequently, during the flight the photometer did occasionally view regions of the ground lying outside the range of the ground array elements. However, because of the non-linear dependence of the sampled ground displacement upon photometer elevation, the vast majority of the observations which intersected the solid earth did so within the ±5° ground element range.

The geometric distribution of the 3222 volume elements, for which emission rates are to be recovered, and the 150 ground elements, for which surface brightnesses are to be determined, is summarized in Fig.3.

3.2. *The tomographic inversion algorithm and the recovered volume emission rates*

Under the algebraic reconstruction approach the surface brightness measured along a particular line of sight, identified by the index 'i', may be expressed as

$$O_i = \sum_j L_{ij} V_j + \sum_k \delta_{ik} B_k \qquad (1)$$

where V_j is the emission rate within the volume element 'j'; L_{ij} represents the path length of the line of sight 'i' through the element 'j'; B_k is the surface brightness of the ground element 'k'; δ_{ik} is unity if the line of sight intersects the ground element 'k' and zero otherwise. This formulation does not take into account the finite field of view of the photometer or the angular smearing resulting from the change in viewing direction during the photometer count integration period. Although allowance can be made for the finite field of view and angular smear, the physical dimensions of the chosen array elements are sufficiently large to allow these effects to be safely ignored for most viewing directions.

Using the rocket position data, available from the ground radar measurements, and the vehicle attitude information provided by the onboard gyro systems, the photometer line of sight at any particular time during the flight may be determined. From this the L_{ij} weighting factors and the values of the δ_{ik} in equation (1) may be calculated for each observation made during the flight. This results in a system containing tens of thousands of linear equations in the 3222 unknown V_j's and 150 unknown B_k's. The tomographic inversion then reduces to the problem of solving this overdetermined set of equations. However, this formulation assumes that the V_j's and B_k's remained constant during the time taken to acquire all of the observations. Coordinated ground-based measurements (Vallance Jones *et al.*, 1990) indicate that this was not strictly the case for the aurora under investigation. The requirement of time invariant V_j's and B_k's could of course be satisfied by considering only the observations made during a small segment of the flight, however, such observations would have been made over a limited range of viewing positions and would therefore contain little tomographic information. To compromise this situation we first consider the data acquired between rocket altitudes of ~190 km and ~80 km on the downleg of the flight. During this part of the descent 265 complete photometer scans were performed between 3:58:31 UT and 4:00:19 UT and 21,500 brightness measurements were made over a significant range of viewing positions. The resulting system of 21,500

equations in 3372 unknowns has been solved to provide an estimate of the mean distribution of the 3914Å volume emission rates within the aurora during this time period.

The algorithm used to solve this system of linear equations is based upon a maximum probability approach which takes into account the Poisson noise associated with the photon counting statistics of the photometer. The algorithm and its implementation have been described in detail by Lloyd and Llewellyn (1989). Essentially, an arbitrary set of initial volume emission rates, V_j's, and ground surface brightnesses, B_k's, is used along with equation (1) to calculate an expected brightness for each of the 21,500 different lines of sight along which measurements were made. Each of the expected brightnesses (expressed in units of counted photons per photometer integration period) is then compared with the corresponding measured brightness. Any discrepancy between the measured and expected counts is treated as having arisen from random fluctuations (Poisson noise) in the number of photons, P_{ij}, actually received from each element, j, along the line of sight, i. For an observation of O_i counts from n_i contributing elements there are $(n_i+O_i-1)!/\{(n_i-1)!O_i!\}$ different possible sets of P_{ij}'s. However, these $(n_i+O_i-1)!/\{(n_i-1)!O_i!\}$ different permutations are not all equally probable and the most likely set of contributions, P_{ij}^{max}, is found using equation (15) of Lloyd and Llewellyn (1989). For each observation a record is kept of how much each contributing V_j or B_k would have to be changed in order to make the expectation value of its contribution to observation i, $L_{ij}V_j$ or $\delta_{ik}B_k$, identical to its maximum likelihood contribution, P_{ij}^{max}. When all 21,500 expected and measured brightnesses have been compared, each of the initial V_j and B_k values is changed by an amount corresponding to the mean value of its implied changes. For the ground surface brightnesses this adjustment is based upon a simple average and for the volume emission rates the adjustment is based upon a weighted mean of the implied changes using the pathlength of each observation i through the element j as the weighting factor. This adjustment procedure results in an improved estimate of the volume emission rates and

ground surface brightnesses. This process is then repeated in an iterative manner until the set of V_j and B_k values converges. Using the 190 km to 80 km data set the solution had essentially converged after the ninth iteration. The mean distribution of the 3914Å volume emission rates thus obtained is shown in panel (a) of Fig.4 which represents the two dimensional distribution of emission that would be most consistent with the observations if there were no temporal variations during the data acquisition period. It is clear from the contours shown in Fig. 4a that the volume emission rates in elements that lie along the parabola of the rocket trajectory are slightly enhanced or depleted relative to their nearest neighbours with which they should be highly correlated. This slight distortion along the trajectory may be suppressed by resetting the volume emission rates of each of the on-trajectory elements to the mean of their two nearest horizontal neighbours. The mean distribution obtained after resetting the on-trajectory elements is shown in panel (b) of Fig. 4.

Clearly, the distributions of 3914Å emission shown in Fig.4 are quite consistent with the qualitative expectations discussed in Section 3. The arc exhibits a primary core at an altitude of ~130 km located ~120 km down range from the launch site, a secondary core is to be found some 30 km to the north at an altitude of ~140 km. The contour lines are clearly more closely spaced below the peak emission than above it - as would be expected for the auroral 3914Å emission - and the adopted primary grid does appear to enclose most of the auroral form. The small region of enhanced emission close to the rocket trajectory along the upper boundary of the grid may be real but a similar enhancement of the emisson rates along the lower boundary of the grid below the main auroral core is more likely to be an artifact.

As discussed above, the coordinated ground-based measurements (Vallance Jones *et al.*, 1990) did indicate that there were temporal variations in the aurora as the rocket descended through the 190 km to 80 km region. To assess the possible impact that these temporal variations may have had on the recovered distribution it is instructive to compare a number

of actual photometer scans with scans reconstructed from the mean distribution for the 3:58:31 UT to 4:00:19 UT period. In Fig.5 we show the measured and reconstructed brightnesses for scans performed at 3:58:56 UT, 3:59:33 UT and 3:59:58 UT when the rocket was at 175 km , 140 km and 110 km respectively. Although the mean distribution does reproduce fairly well the qualitative and quantitative aspects of the scans made at these particular times, some discrepancies do exist between the measured and re-constructed brightnesses. For example, the brightness measured at a photometer elevation of 300° from 175 km is less than the brightness expected from the mean distribution which suggests that the southern core was somewhat weaker earlier in the flight.

In an attempt to allow for temporal variations in the aurora we have investigated the possibility of using the mean distribution derived from the 190 km to 80 km data set as the starting point for a number of independent inversions based on sets of observations made over smaller time intervals. For example, if we use the mean distribution shown in Fig. 4 for the initial set of V_j and B_k values and apply the inversion algorithm to only the 15 seconds of observations centred on the rocket altitude of 175 km the distribution shown in Fig.6 is obtained. Using this approach the solution had basically converged after three or four iterations. The distribution of Fig.6 does provide an improved fit to the observations centred on the rocket altitude of 175 km (see Fig.7) and indicates that the volume emission distribution during the 3:58:48 UT to 3:59:03 UT period had a stronger northern core and a weaker southern core than the distribution shown in Fig. 4. The distributions, and scan re-constructions, obtained in a similar manner using 15 seconds of observations centred on rocket altitudes of 140 km and 110 km are shown in Figs.8 through 11. Here again the approach results in better agreement between the measured and reconstructed brightnesses and confirms that the northern core weakened and the southern core intensified during the rocket's descent.

Although the temporal evolution of the aurora, implied by Figs. 6, 8 and 10, is quite consistent with the information available from the ground-based observations (Vallance Jones *et al.*, 1990), it is difficult to assess the level of confidence that should be placed in the recovered volume emission rate distributions. However, an examination of the ground surface brightnesses that were recovered along with the volume emission rates does lend support to their validity. When considering the recovered ground surface brightnesses we should point out that these quantities are obtained from the inversion algorithm independently of the volume emission rates, i.e. the ground brightnesses, or B_k's, are free parameters that are not in any way constrained to the values of the overhead V_j's. Physically, however, the ground surface brightnesses are determined by the distribution of volume emission rates. Consequently, a comparison of the recovered V_j's and B_k's provides an important means of testing the reliability of the entire inversion procedure.

The relationship between the brightness of a scattering surface, assumed in this case to be Lambertian, and the distribution of luminosity above it has been considered within the context of auroral photometry by Hays and Anger (1978). With the assumption that the aurora under investigation extended uniformly in the east-west direction, we have used the formulation described by Hays and Anger (1978) to calculate the ground surface brightnesses that would be expected to accompany the 3914Å volume emission rate distribution shown in Fig.10. The distribution of ground surface brightnesses thus obtained, assuming initially a 3914Å surface albedo of unity for all ground elements, is similar in shape to the ground brightness distribution that was recovered along with the volume emission rates of Fig.10. The normalization factor required to match these two distributions, as shown in Fig.12, corresponds to an effective 3914Å albedo of 0.65. This ground albedo compares quite favorably with the value of 0.8 usually adopted for this spectral region (Hays and Anger, 1978). Further evidence to support the validity of the recovered volume emission rates emerges from an inspection of the volume emission rates

assigned, by the inversion procedure, to the northern and southern arrays of stratified layers.

In Fig.13 we show the volume emission rates assigned to the stratified arrays by the inversion of the 15 seconds of observations centred on a rocket altitude of 110 km. The bulk of the 3914Å emission originating from the northern limb is restricted to a narrow layer lying between altitudes of 80 and 100 km. In contrast, the emission originating from the southern limb is much stronger and shifted to altitudes that are more typical of auroral emissions. This marked north/south asymmetry is quite typical of what would be expected in the vicinity of a discrete auroral arc. Equatorward of discrete arcs a number of diffuse auroral forms, distributed over several degrees of latitude, are usually observed. To the north the level of optical auroral activity is usually much weaker. It should also be noted that the shape of the emission profile recovered for the northern stratified layers closely resembles a quiescent O_2 nightglow emission profile (Murtagh *et al.*, 1986a; 1986b). It is tempting to suggest, therefore, that the northern limb emission is due to the O_2 nightglow rather than auroral N_2^+. The 3914Å photometer filter would have captured only a small fraction of the total O_2 nightglow emission, but the relatively strong (5-3) and (3-2) bands of the $O_2(A^3\Delta_u \rightarrow a^1\Delta_g)$ Chamberlain system fall within the passband of the 3914Å filter. We have considered the filter capture functions for the various O_2 nightglow systems and find that for typical nightglow intensities of 500, 100 and 200 Rayleighs in the Herzberg I, Herzberg II and Chamberlain systems (Murtagh *et al.*, 1986a; 1986b), the total zenith intensity captured by the photometer would have been ~20 Rayleighs. The northern limb emission profile shown in Fig. 13 represents a captured zenith intensity of ~25 Rayleighs. It seems likely, therefore, that most of the northern limb emission did arise from the O_2 Chamberlain band system. It may at first seem surprising that a nightglow profile could have been resolved, or partially resolved, from airglow limb scan observations made with a photometer with a 2.5^o degree field of view. However, the rocket did pass through the

airglow layer upon descend and the scans made late in the flight would have provided side look observations etc. that the inversion algorithm would automatically deconvolve.

4. DISCUSSION AND CONCLUSIONS

The N_2^+ 3914Å volume emission distributions obtained in the previous section for three selected times during the descend of the ARIES 'B' rocket, represent a rather unique data base for investigations of auroral excitation processes. When considered along with the comprehensive energetic particle measurements that were made during the flight (Vallance Jones *et al.*, 1990) the data should allow various auroral models to be tested in a manner not usually afforded by a single rocket experiment. Conventional rocket auroral photometry experiments can only provide information about the excitation and ionization rates occurring along a single field line involving incident electrons with a particular energy spectrum - or more strictly a number of field lines upon which the incident spectra and fluxes are assumed to be the same. The measured profiles can then only be compared with model expectations for that particular incident electron spectrum. In contrast, the results of the ARIES experiment will allow comparisons to be made with a number of profiles measured along field lines involving different incident spectra. An additional advantage of this approach is that the analysis of these essentially different precipitation events can be performed with the knowledge that they all occurred under otherwise identical atmospheric conditions.

Examples of the 3914Å emission profiles that may be extracted from the recovered 2-dimensional distributions are shown Fig.14. The profile labelled 'North' in Fig. 14 is a slice through the distribution of Fig. 6 and corresponds to a field line passing through the rocket at ~180 km and close to the centre of the northern auroral core. The profile labelled 'South' in Fig. 14 is a slice through the distribution shown in Fig. 8 and corresponds to a field line passing through the rocket at ~130 km and close to the centre of the southern

auroral core. Clearly, the energy spectra of the electrons incident upon these two field lines must have been quite different. In a companion paper by Vallance Jones *et al.* (1990) these 3914Å emission profiles are compared with theoretical profiles calculated using various auroral excitation models and the in-situ energetic particle measurements.

Acknowledgements - The authors would like to thank Drs. A. Vallance Jones and R.L. Gattinger for many valuable discussions and their encouragement to pursue the tomographic studies presented here. We also wish to express our gratitude to the National Research Council of Canada Space Division personnel, particularly Mr. Hal Roberts, for their efforts to ensure the success of the ARIES campaign and the rocket launch. This work was supported at the University of Michigan by internal funds from the Space Physics Research Laboratory and by the National Aeronautics and Space Administration grant NAG5-670. At the University of Saskatchewan the work was supported by Grants-In-Aid from the Natural Sciences and Engineering Research Council of Canada.

REFERENCES

Hays, P.B. and Anger, C.D. (1978) Influence of ground scattering on satellite auroral observations. *Appl. Opt.*, **17**, 1898.

Lloyd, N.D. and Llewellyn, E.J. (1989) Deconvolution of blurred images using photon counting statistics and maximum probability. *Can. J. Phys.*, **67**, 89.

Murtagh, D.P., McDade,I.C., Greer, R.G.H., Stegman, J., Witt, G. and Llewellyn, E.J. (1986a) ETON 4: An experimental investigation of the altitude dependence of the $O_2(A^3\Sigma_u^+)$ vibrational populations in the nightglow. *Planet. Space Sci.*, **34**, 811.

Murtagh, D.P., Witt, G.and Stegman, J. (1986b) O_2 -triplet emissions in the nightglow. *Can. J. Phys.*, **64**, 1587.

Solomon, S.C., Hays, P.B. and Abreu, V.J. (1984) Tomographic inversion of satellite photometry. *Appl. Opt.*, **23**, 3409.

Solomon, S.C., Hays, P.B. and Abreu, V.J. (1985) Tomographic inversion of satellite photometry. Part 2. *Appl. Opt.*, **24**, 4134.

Solomon, S.C., Hays, P.B. and Abreu, V.J. (1988) The auroral 6300Å emission: observations and modelling. *J. geophys. Res.*, **93**, 9867.

Thomas, R. J., and Donahue, T.M. (1977) Analysis of Ogo 6 observations of the OI 5577Å tropical nightglow. *J. Geophys. Res.*, **77**, 79.

Vallance Jones, A., Gattinger, R.L., Creutzberg, F., Harris, F.R., McNamarra, A.G., Yau, A.W., McEwan, D.J., Llewellyn, E.J., Lummerzheim, D., Rees, M.H., McDade, I.C., and Margot-Chaker, J. (1990) Characterization and modelling of an evening auroral arc observed from a rocket and a ground-based line of meridian scanners. *Planet. Space Sci..*, to be submitted 1990.

Figure Captions

FIG. 1. A sequence of photometer scans illustrating the data obtained from the 3914Å photometer between altitudes of 200 km (top) and 70 km (bottom) on the downleg of the ARIES 'B' flight. To produce this plot the raw photometer counts were collected into equal elevation angle bins, then averaged over four consecutive scans and shifted in the ordinate for clarity. The count rate is expressed in counts per 5 msec integration period.

FIG. 2. Polar plots of the 3914Å brightnesses measured during two single photometer scans made at 3:58:56 UT and 3:59:58 UT when the rocket was at altitudes of ~175km and ~110km respectively. The plots are centred on their respective positions along the flight trajectory which is shown by the dotted line. The intersections labelled "N" and "S" should qualitatively locate the strongest features in the spatial distribution of the 3914Å emission.

FIG. 3. A summary of the spatial distribution of the 3222 volume elements and 150 ground elements considered in the tomographic inversion.

FIG.4 (a) The distribution of 3914Å emission obtained as described in the text from an inversion of the observations made between 3:58:31 UT and 4:00:19 UT. The recovered N_2^+ 1N (0-0) band volume emission rate contours are drawn at equal intervals of 100 photons cm^{-3} sec^{-1}. The dotted curve shows the rocket trajectory.

(b) Same as shown in panel (a) with the emission rates along the trajectory modified as described in the text.

FIG. 5. The measured brightnesses (data points) and the brightnesses reconstructed from the distribution of Fig.4b (histograms) for the photometer scans made at 3:58:56 UT, 3:59:33 UT and 3:59:58 UT when the rocket was at 175 km, 140 km and 110 km respectively. The data points represent the observations made during 1 second or approximately 2.5 rolls. The count rate is expressed in counts per 5 msec integration period.

FIG. 6. The distribution of 3914Å emission obtained as described in the text from an inversion of the observations made during the 15 second interval centred on 3:58:56 UT when the rocket was at an altitude of 175 km. The recovered N_2^+ 1N (0-0) band volume emission rate contour lines are drawn at intervals of 100 photons cm^{-3} sec^{-1}. The dotted curve shows the rocket trajectory.

FIG. 7. The measured brightnesses (data points) and the brightnesses reconstructed from the distribution of Fig.6 (histogram) for a photometer scan made at 3:58:56 UT when the rocket was at an altitude of 175 km. The data points represent the observations made during a 2 second interval centred on the time of interest. The count rate is expressed in counts per 5 msec integration period.

FIG. 8. The distribution of 3914Å emission obtained as described in the text from an inversion of the observations made during the 15 second interval centred on 3:59:33 UT when the rocket was at an altitude of 140 km. The recovered N_2^+ 1N (0-0) band volume emission rate contour lines are drawn at intervals of 100 photons cm^{-3} sec^{-1}. The dotted curve shows the rocket trajectory.

FIG. 9. The measured brightnesses (data points) and the brightnesses reconstructed from the distribution of Fig.8 (histogram) for a photometer scan made at 3:59:33 UT when the rocket was at an altitude of 140 km. The data points represent the observations made during a 2 second interval centred on the time of interest. The count rate is expressed in counts per 5 msec integration period.

FIG. 10. The distribution of 3914Å emission obtained as described in the text from an inversion of the observations made during the 15 second interval centred on 3:59:58 UT when the rocket was at an altitude of 110 km. The recovered N_2^+ 1N (0-0) band volume emission rate contour lines are drawn at intervals of 100 photons cm^{-3} sec^{-1}. The dotted curve shows the rocket trajectory.

FIG. 11. The measured brightnesses (data points) and the brightnesses reconstructed from the distribution of Fig.10 (histogram) for a photometer scan made at 3:59:58 UT when the rocket was at an altitude of 110 km. The data points represent the observations made during a 2 second interval centred on the time of interest. The count rate is expressed in counts per 5 msec integration period.

FIG. 12. The ground surface brightnesses (circles) recovered along with the volume emission rates shown in Fig.10 and the theoretical ground brightnesses (solid curve) calculated as described in the text with an effective 3914Å albedo of 0.65.

FIG. 13. The volume emission rates assigned to the northern and southern stratified layers by the inversion of the observations centred on 3:59:58 UT. The emission rates are expressed in terms of Rayleighs captured by the photometer.

FIG. 14. N_2^+ 1N (0-0) band volume emission profiles extracted from the distributions shown in Figs.6 and 8. The profile labelled 'North' corresponds to a field line passing through the rocket at ~180 km and close to the centre of the northern auroral core in Fig. 6. The profile labelled 'South' corresponds to a field line passing through the rocket at ~130 km and close to the centre of the main auroral core in Fig. 8.

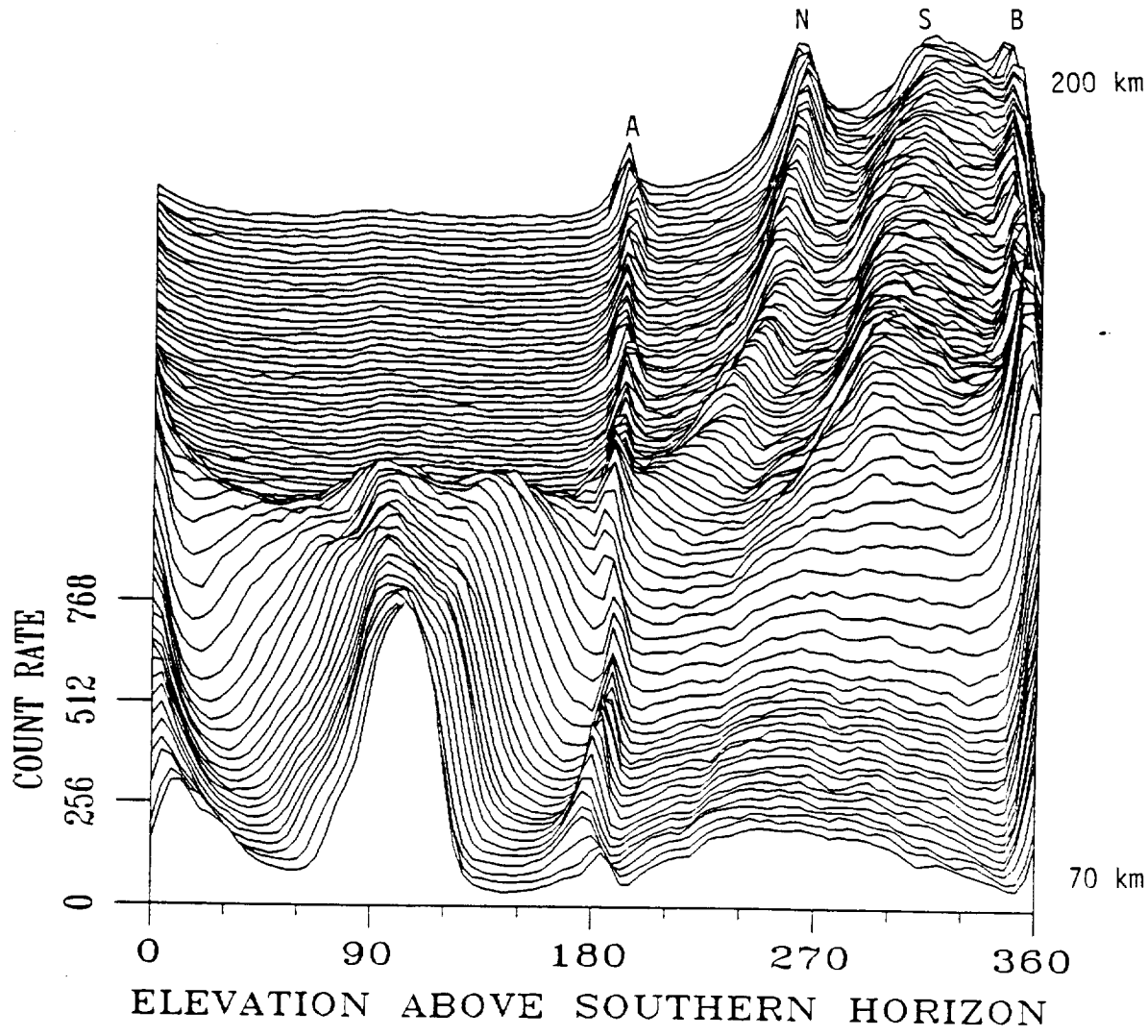
ARIES B 3914 downleg 200-70 km
N
S
B
A
200 km
70 km
COUNT RATE
0
256
512
768
0
90
180
270
360
ELEVATION ABOVE SOUTHERN HORIZON

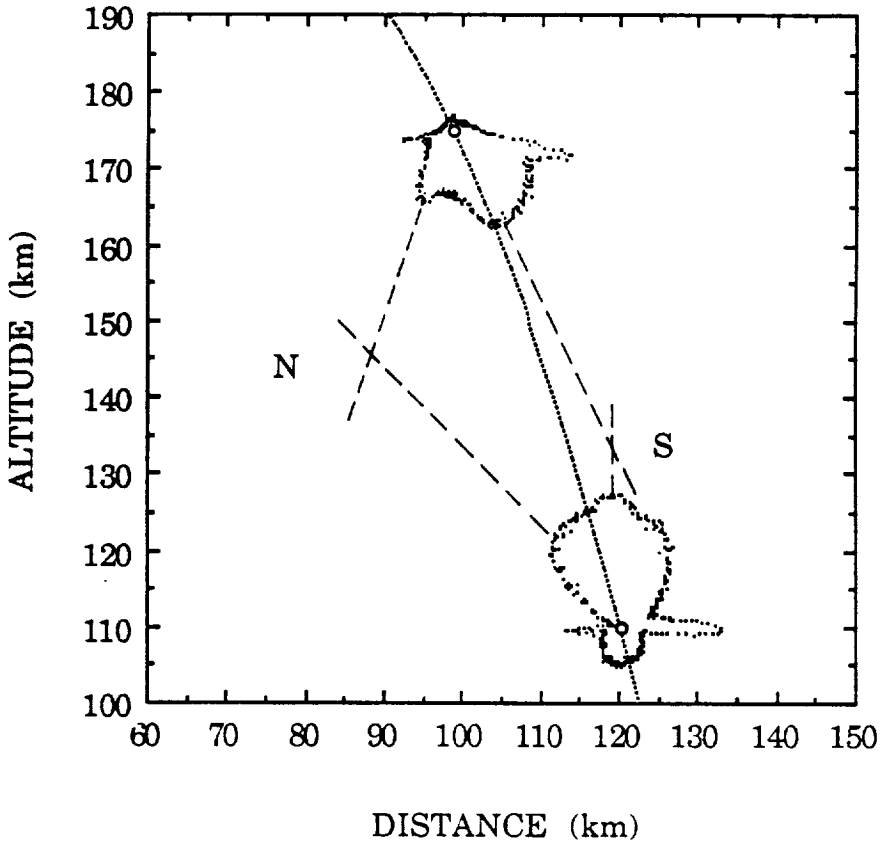
190
180
170
160
150
140
130
120
110
100
ALTITUDE (km)
60
70
80
90
100
110
120
130
140
150
DISTANCE (km)
N
S

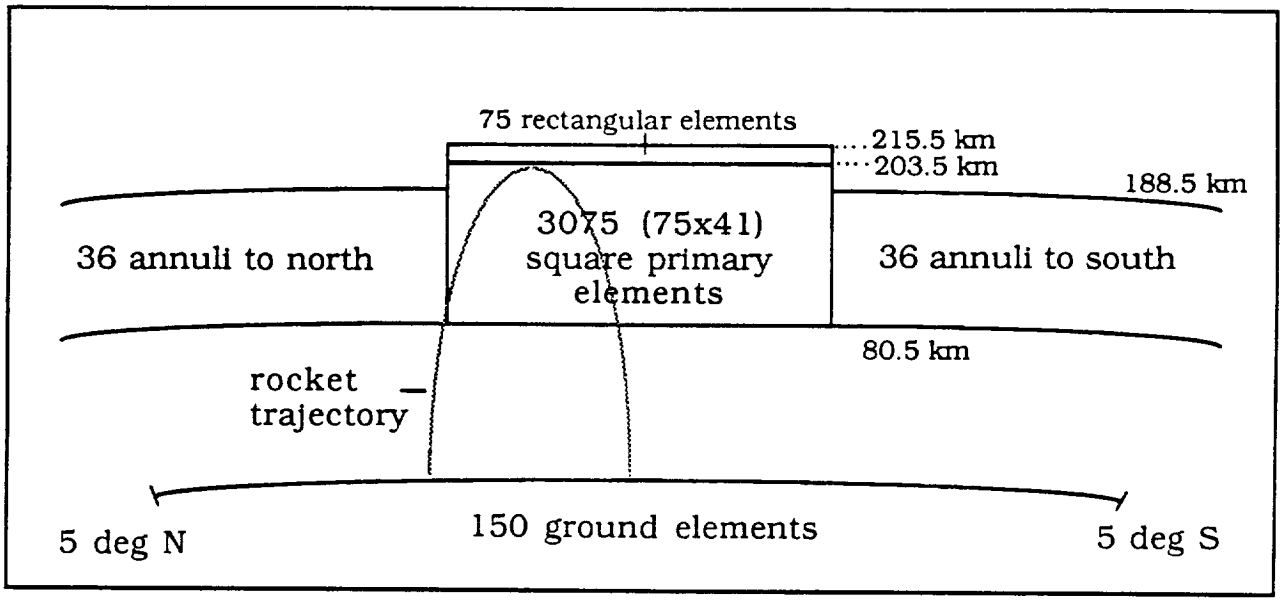
75 rectangular elements
215.5 km
203.5 km
188.5 km
36 annuli to north
3075 (75x41)
square primary
elements
36 annuli to south
80.5 km
rocket
trajectory
5 deg N
150 ground elements
5 deg S

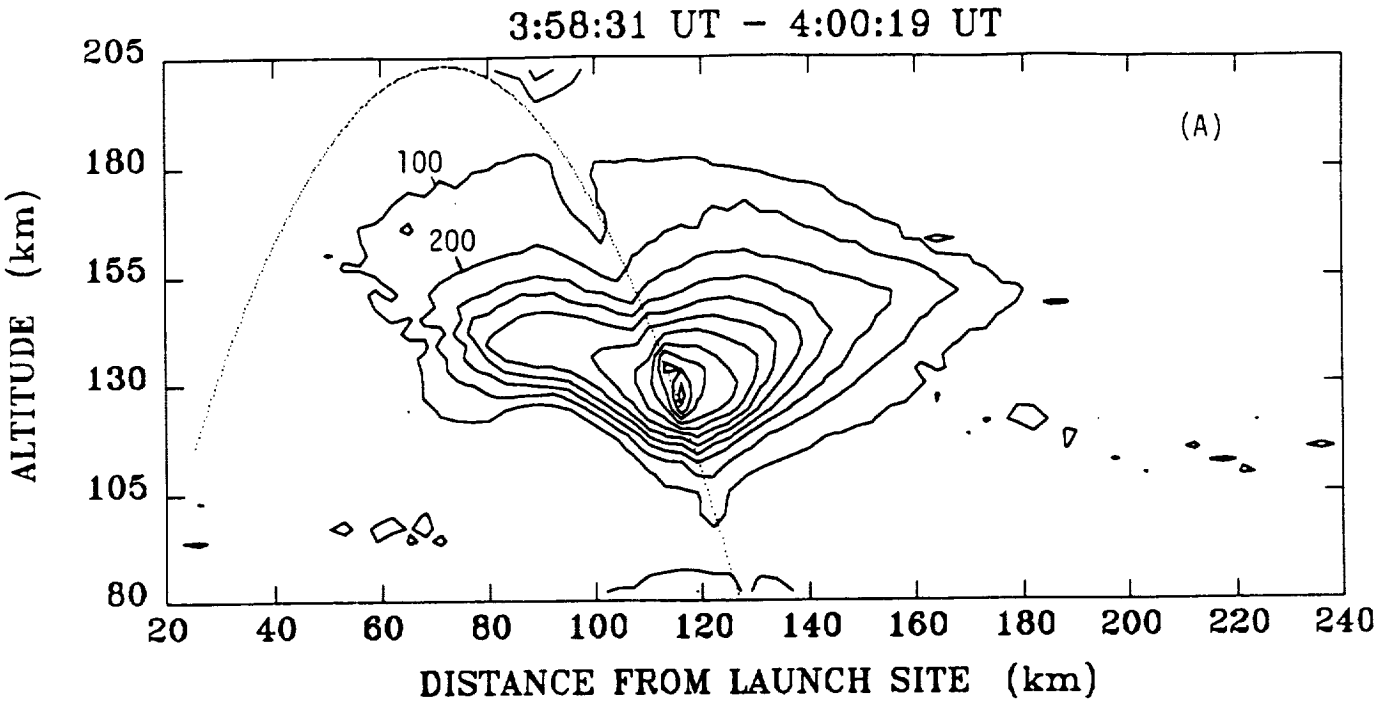
3:58:31 UT – 4:00:19 UT
(A)
100
200
ALTITUDE (km)
205
180
155
130
105
80
20
40
60
80
100
120
140
160
180
200
220
240
DISTANCE FROM LAUNCH SITE (km)

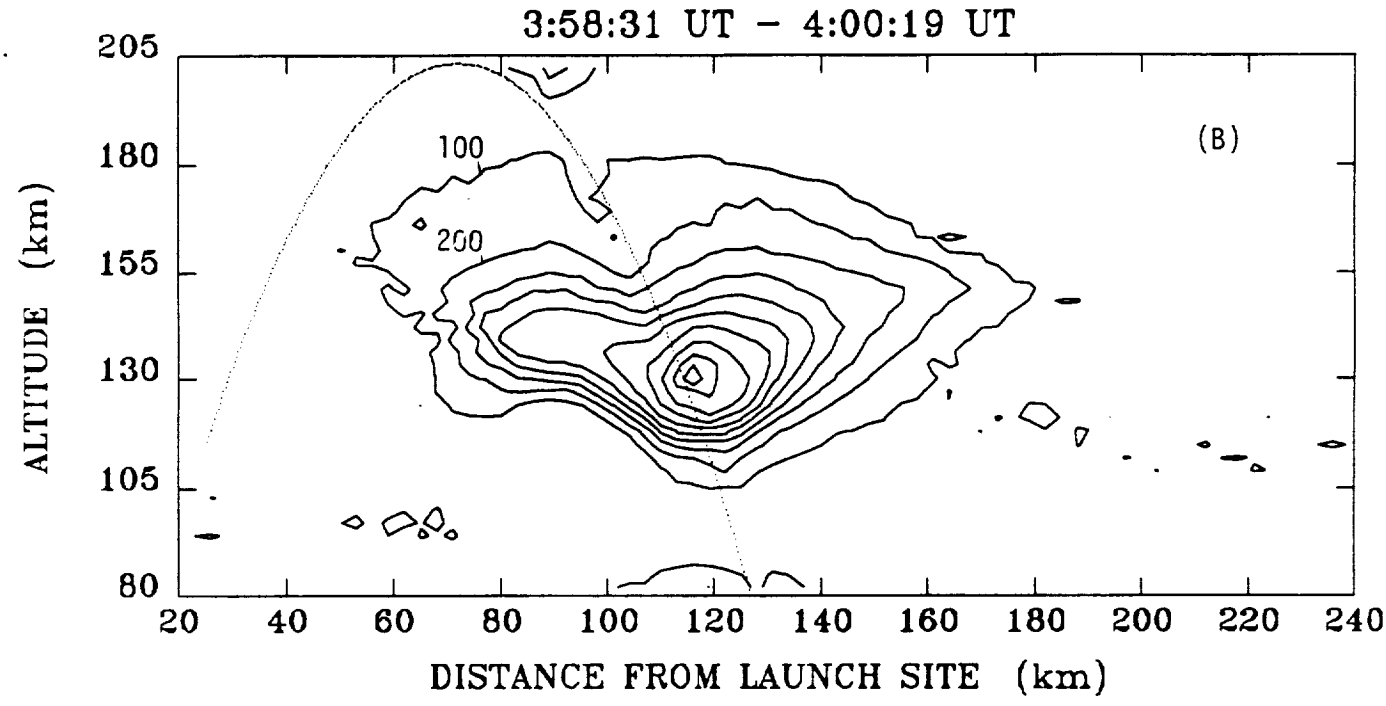
3:58:31 UT – 4:00:19 UT
(B)
100
200
ALTITUDE (km)
205
180
155
130
105
80
20
40
60
80
100
120
140
160
180
200
220
240
DISTANCE FROM LAUNCH SITE (km)

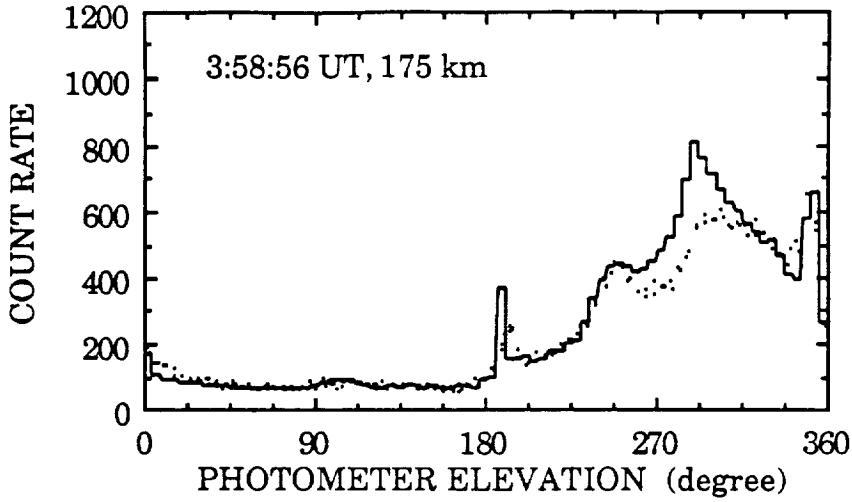
3:58:56 UT, 175 km
COUNT RATE
1200
1000
800
600
400
200
0
0
90
180
270
360
PHOTOMETER ELEVATION (degree)

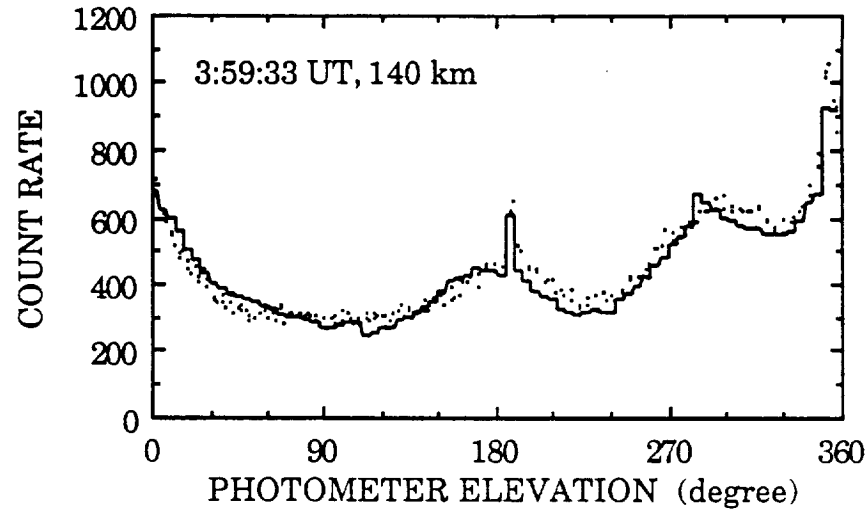
3:59:33 UT, 140 km
COUNT RATE
1200
1000
800
600
400
200
0
0
90
180
270
360
PHOTOMETER ELEVATION (degree)

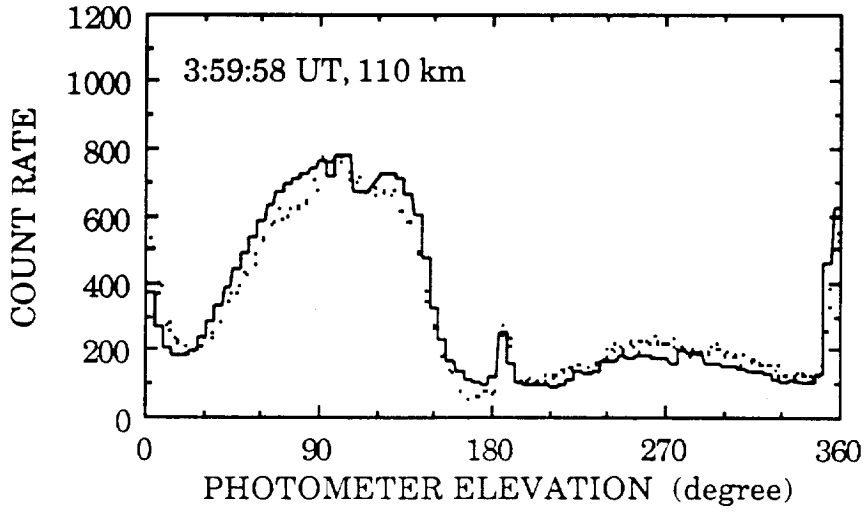
3:59:58 UT, 110 km
COUNT RATE
1200
1000
800
600
400
200
0
0
90
180
270
360
PHOTOMETER ELEVATION (degree)

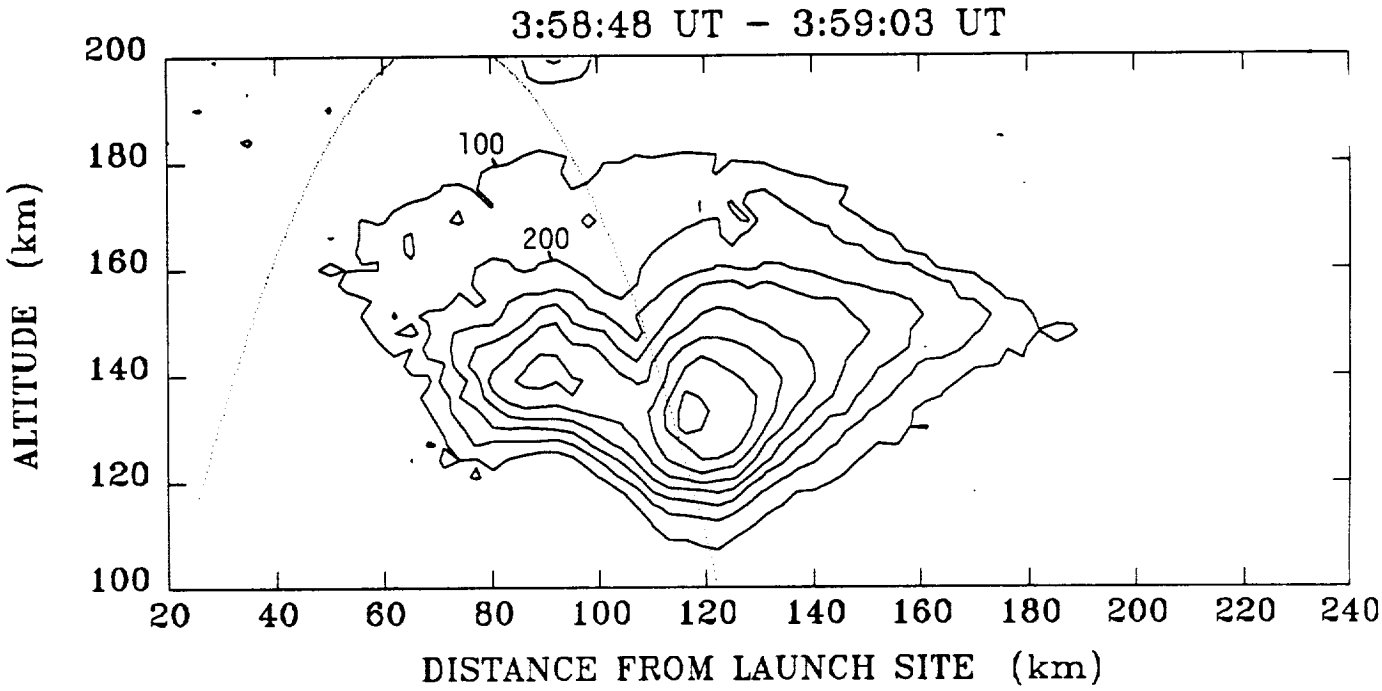
3:58:48 UT - 3:59:03 UT
200
180
160
140
120
100
ALTITUDE (km)
100
200
20
40
60
80
100
120
140
160
180
200
220
240
DISTANCE FROM LAUNCH SITE (km)

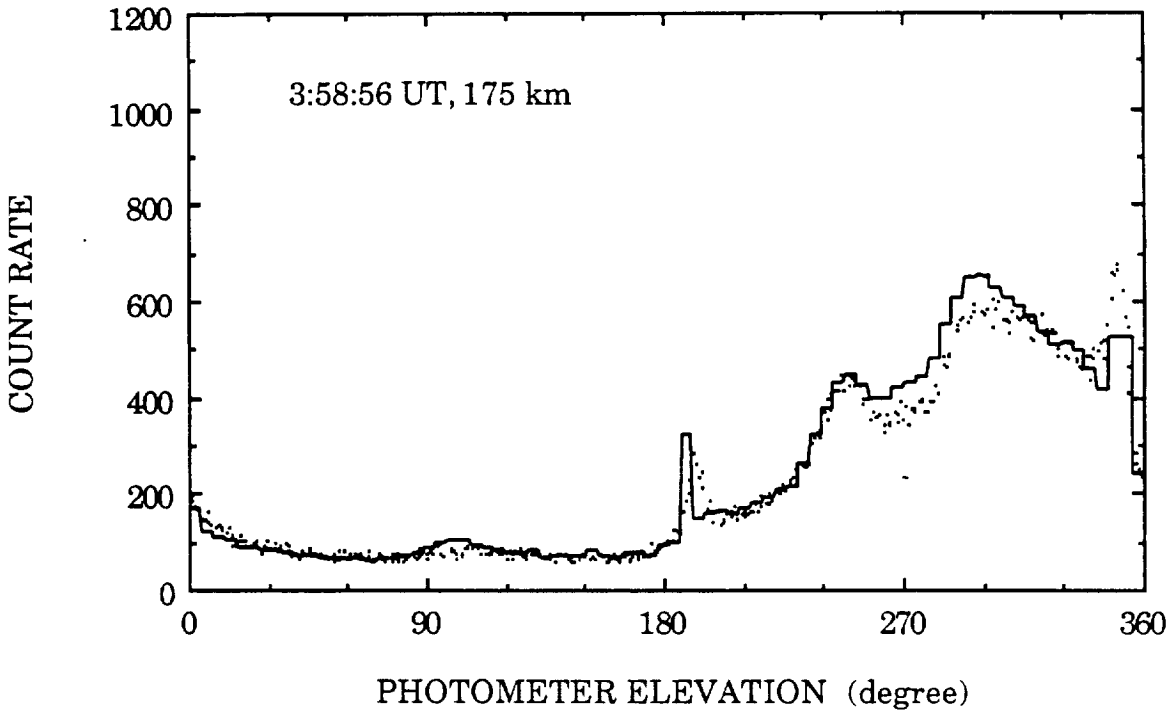
3:58:56 UT, 175 km
COUNT RATE
1200
1000
800
600
400
200
0
0
90
180
270
360
PHOTOMETER ELEVATION (degree)

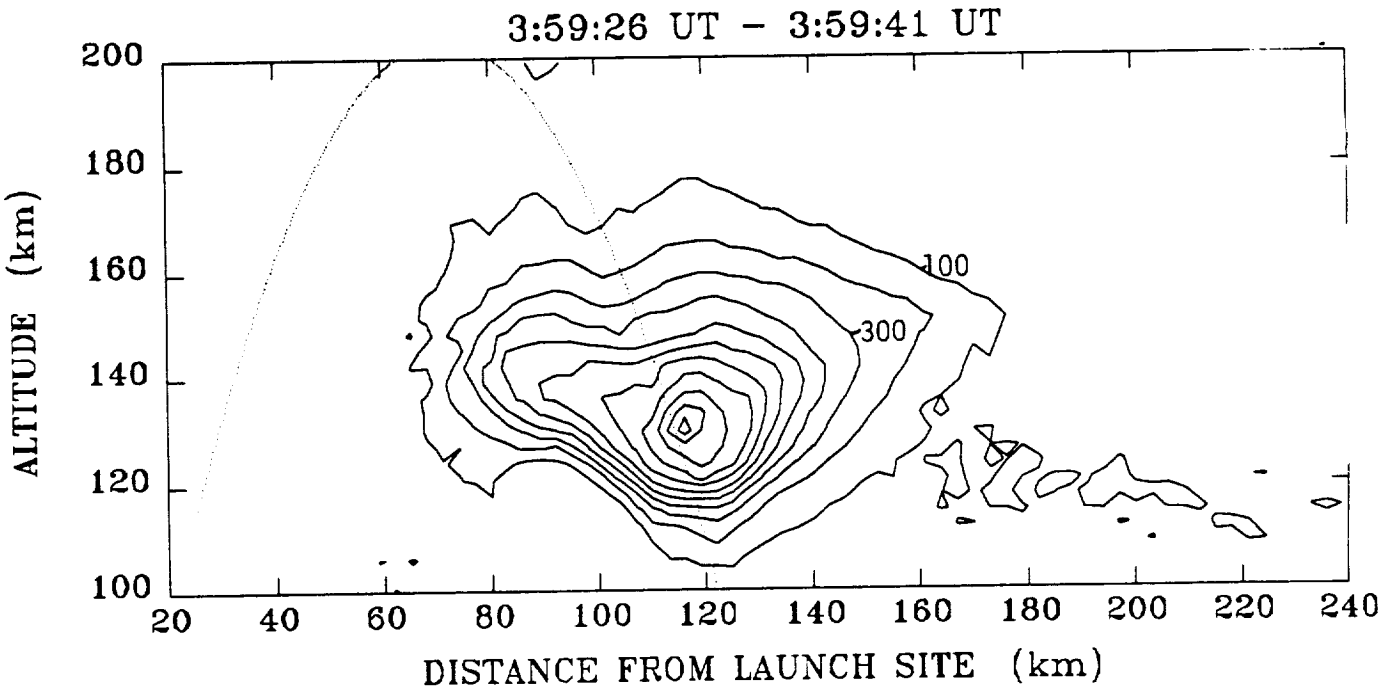
3:59:26 UT - 3:59:41 UT
ALTITUDE (km)
200
180
160
140
120
100
20
40
60
80
100
120
140
160
180
200
220
240
DISTANCE FROM LAUNCH SITE (km)
100
300

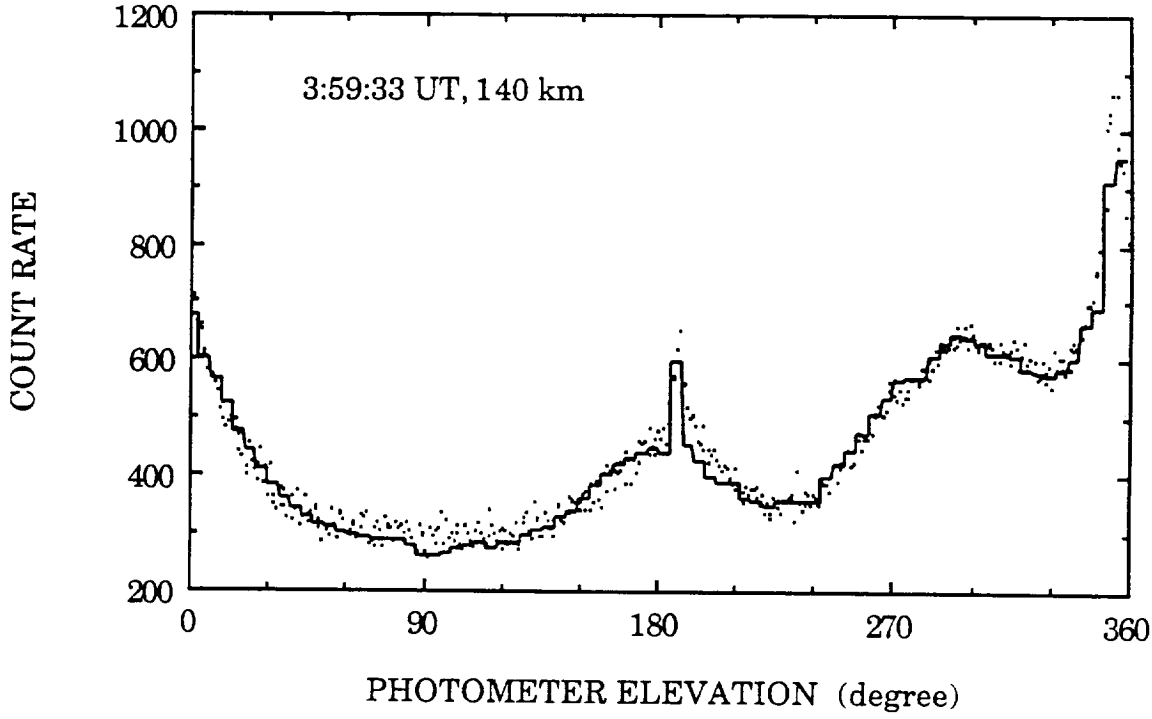
3:59:33 UT, 140 km
COUNT RATE
1200
1000
800
600
400
200
0
90
180
270
360
PHOTOMETER ELEVATION (degree)

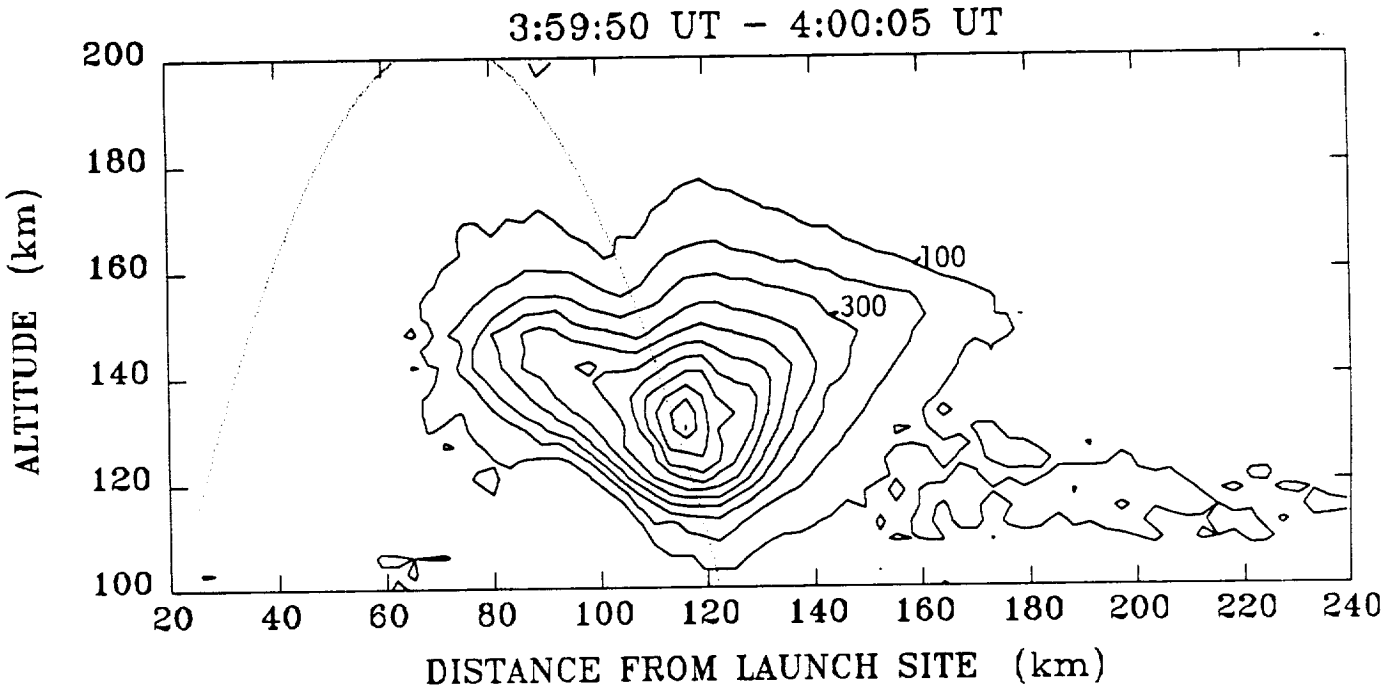

NAGS-670 'B' 31

FIG 10

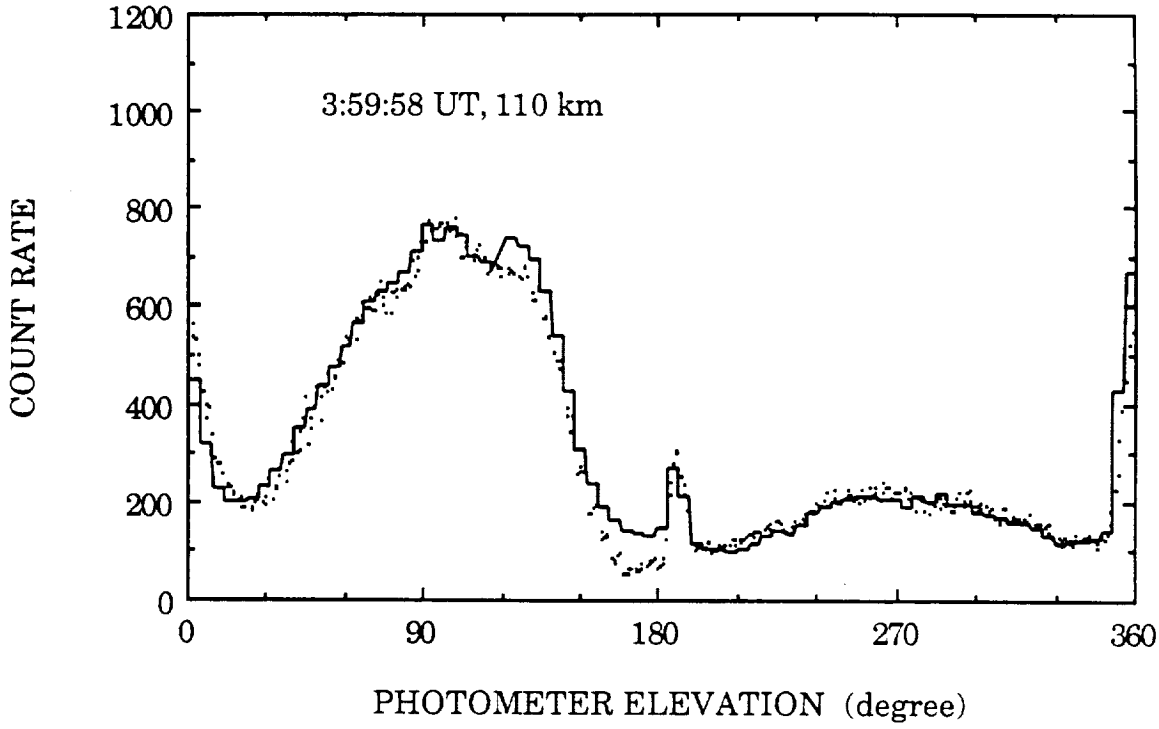
3:59:58 UT, 110 km
COUNT RATE
1200
1000
800
600
400
200
0
0
90
180
270
360
PHOTOMETER ELEVATION (degree)

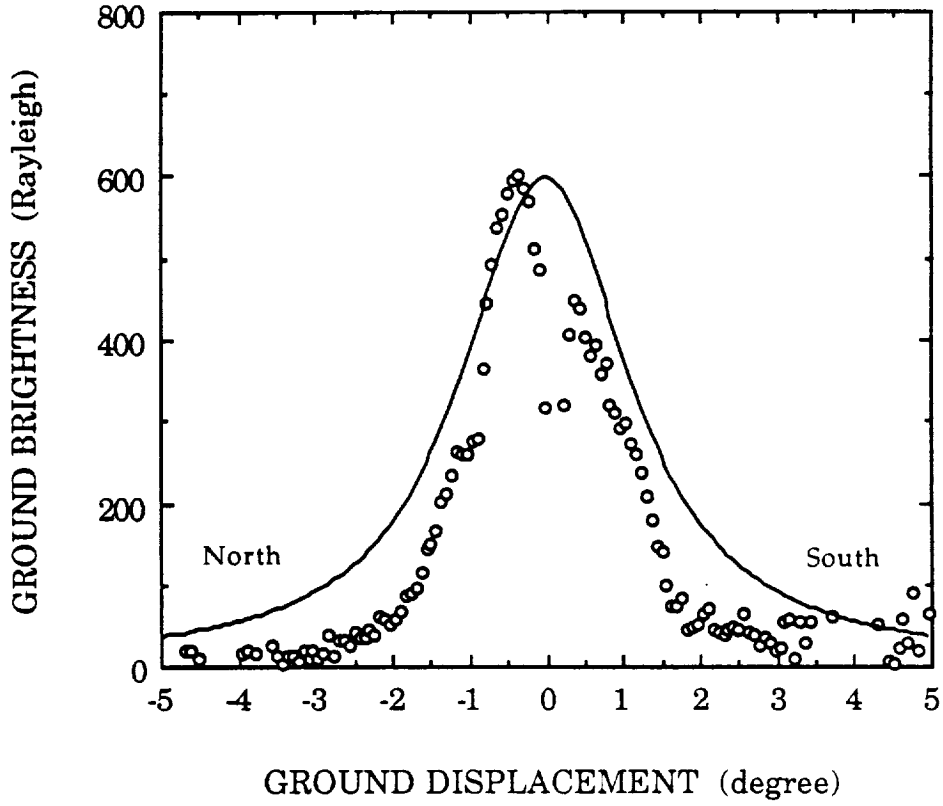
GROUND BRIGHTNESS (Rayleigh)
800
600
400
200
0
North
South
-5
-4
-3
-2
-1
0
1
2
3
4
5
GROUND DISPLACEMENT (degree)

FIG. 12

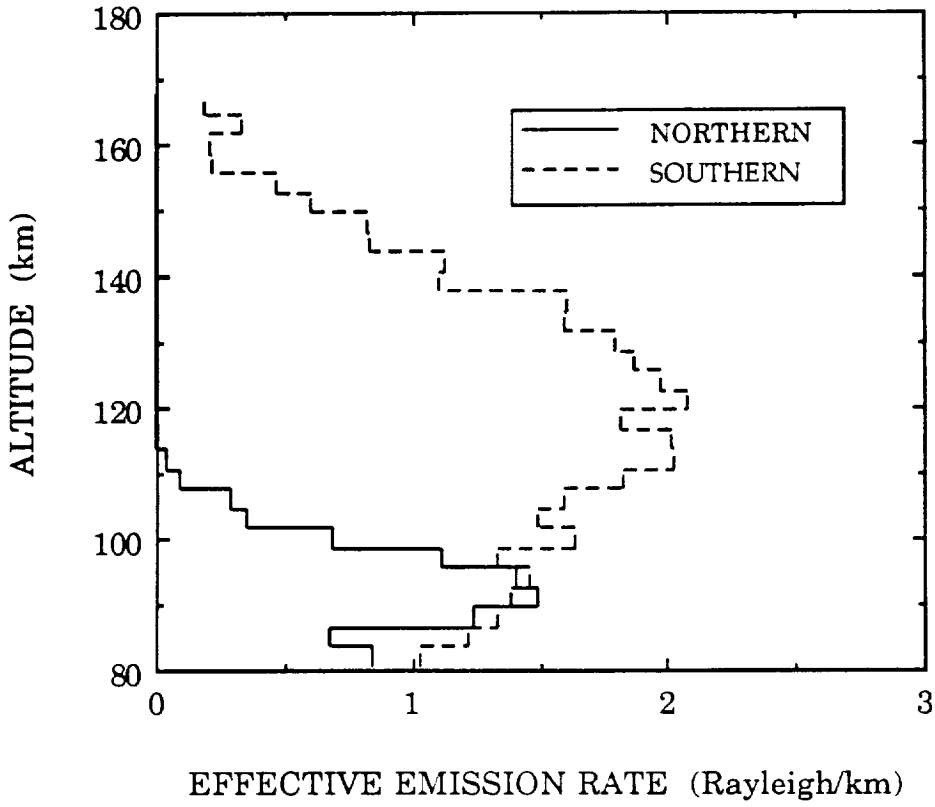
180
160
140
120
100
80
0
1
2
3
ALTITUDE (km)
NORTHERN
SOUTHERN
EFFECTIVE EMISSION RATE (Rayleigh/km)

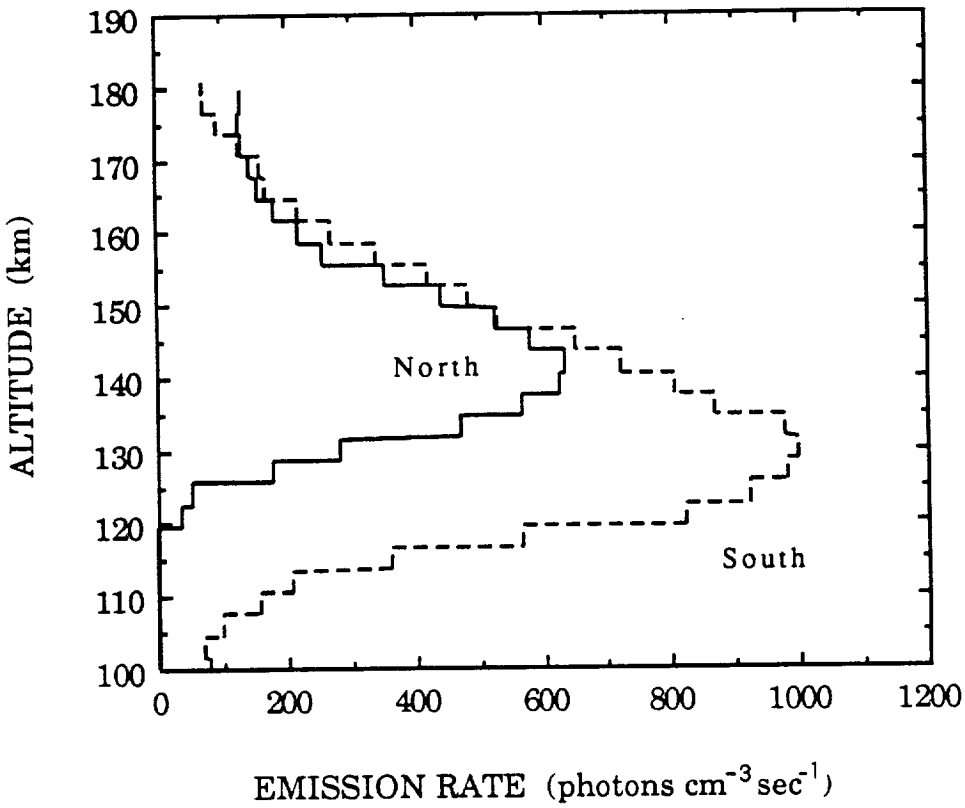
190
180
170
160
150
140
130
120
110
100
0
200
400
600
800
1000
1200
ALTITUDE (km)
North
South
EMISSION RATE (photons cm^{-3} sec^{-1})

THE ANALYSIS OF A ROCKET TOMOGRAPHY MEASUREMENT OF THE N_2^+ 3914Å EMISSION AND N_2 IONIZATION RATES IN AN AURORAL ARC

NASA Grant No. NAG5-670

FINAL REPORT

APPENDIX 'C'

"The ARIES Auroral Modelling Campaign: Characterization and Modelling of an Evening Auroral Arc Observed from a Rocket and a Ground-Based Line of Meridian Scanners"

A.Vallance Jones, R.L. Gattinger, F. Creutzberg, F.R. Harris
A.G. McNamara, and A.W. Yau
Herzberg Institute of Astrophysics, National Research Council Canada

E.J. Llewellyn
Institute of Space and Atmospheric Studies,University of Saskatchewan

D. Lummerzheim and M.H. Rees
Geophysical Institute, University of Alaska

Ian C. McDade
Space Physics Research Laboratory
Department of Atmospheric, Oceanic and Space Sciences
University of Michigan

J. Margot
Departement de Physique, Universite de Montreal

Accepted for publication in *Planetary and Space Science*, 1991.

Abstract - An auroral arc system excited by soft electrons, was studied with a combination of *in situ* rocket measurements and optical tomographic techniques using data from a photometer on a horizontal, spinning, rocket and a line of three meridian scanning photometers. The ground-based scanner data at 4709Å, 5577Å, 8446Å and 6300Å were successfully inverted to provide a set of volume emission rate distributions in the plane of the rocket trajectory with a basic time resolution of 24 seconds. Volume emission rate profiles, derived from these distributions peaked at about 150 km for 5577Å and 4709Å while the 8446Å emission peaked at about 170 km with a more extended height distribution. The rocket photometer gave comparable volume emission rate distributions for the 3914Å emission as reported in a separate paper by McDade et al. (1991). Instruments on the rocket measured the primary electron flux during the flight and in particular, the flux precipitating into the auroral arc overflown at apogee (McEwen et al. 1991). The local electron density and temperature were measured by probes on the rocket (Margot and McNamara (1991). The electron density measurements on the downleg were modelled using ion production rate data derived from the optical results. Model calculations of the emission height profile based on the measured electron flux agree with the observed profiles. The height distribution of the N_2^+ emission in the equatorward band through which the rocket passed during the descent, was measured by both the rocket and the ground-based tomographic techniques and the results are in good agreement. Comparison of these profiles with model profiles indicates that the exciting primary spectrum may be represented by an accelerated Maxwellian or a Gaussian distribution centered at about 3 keV. This distribution is close to what would be obtained if the electron flux exciting the poleward form were accelerated by a 1 to 2 kV upward potential drop. The relative height profiles for the volume emission rate of the 5577Å OI emission and the 4709Å

N_2^+ emission were almost indistinguishable from each other for both the forms measured, with ratios in the range 38 to 50; this is equivalent to I(5577)/I(4278) ratios of 8 to 10. The auroral intensities and intensity ratios measured in the magnetic zenith from the ground during the period before and during the rocket flight are consistent with the primary electron fluxes and height distributions measured from the rocket. Values of I(5577)/I(4278) in the range 8 to 10 were also measured directly by the zenith ground photometers over which the arc system passed. These values are slightly higher than those reported by Gattinger and Vallance-Jones (1964) and this may possibly indicate an enhancement of the atomic oxygen concentration at the time of the flight. Such an enhancement would be consistent with our result that the observed values of I(5577) and I(8446) are also significantly higher than those modelled on the basis of the electron flux spectrum measured at apogee.

1. INTRODUCTION

The modelling of auroral emissions involves the calculation of the evolution of a flux of down-coming primary electrons penetrating into the atmosphere. Once the height distribution of this electron flux is derived, the volume emission rate of various auroral features may be calculated, for possible direct and indirect excitation processes, provided sufficient information on excitation cross sections and reaction rates is available.

Methods of testing excitation models include comparison with observed optical emissions as well as with *in situ* measurements of the electron flux and electron and ion concentrations. Other important quantities such as the electron and ion temperature may be derived from the models and compared with measured values. The object of these studies is to identify the important excitation processes and to understand fully other processes in the auroral ionosphere.

Four main methods of comparison between theory and observation may be distinguished and are listed below. In many cases, more than one of these tests have been applied to the same set of observations.

1.) Comparison of height-integrated intensities of emission features with predicted values based on satellite or rocket measurements of the primary particle flux above the auroral form.

2) Comparisons for internal consistency of models and observations e.g. consistency between modelled or observed profiles of well understood emissions such as the N_2^+ or N_2 bands with predicted profiles of less well understood emissions such as OI 5577Å, OI 6300Å or bands of O_2.

3) Comparisons between model profiles based on directly observed primary electron spectra measured above auroral forms and emission profiles

measured by flying a rocket through the aurora.

4) Rocket measurement of the primary particle flux by over-flying an auroral form combined with external methods to measure the emission profiles such as ground, rocket or satellite triangulation or tomography.

One of the first detailed comparisons of the height profile of auroral emissions and a theoretical model was made by Rees et al. (1967). In that work the height profile of the 5577Å, 6300Å and 3914Å emissions was obtained from optical photometer observations from two ground stations, one almost beneath an isolated auroral arc and the other to the south so that the two-dimensional distribution of the volume emission rate could be derived.

Since the first rocket flight (Cummings et al. 1966) carrying particle detectors and optical photometers, there have been many attempts to make detailed comparisons between the emission profiles of auroral emissions predicted from observed particle energy spectra and observed profiles measured from the ground or from rocket or satellite-borne instruments. Donahue et al. (1968), Parkinson et al. (1970), Parkinson and Zipf (1970) and Parkinson (1971) reported and analysed an epoch-making series of well instrumented Aerobee rocket flights which addressed the problem of the excitation mechanism the 5577Å auroral green line. Parkinson and Zipf suggested the energy transfer process from $N_2(A^3\Sigma_u^+)$ to atomic oxygen as the principal mechanism but were diverted from this possibly correct explanation in part because the then current laboratory value for the reaction was almost an order of magnitude too low. These rocket studies called into question the apparently satisfactory excitation mechanism for the 5577Å emission derived by Rees, Walker and Dalgarno (1967), namely electron impact on atomic oxygen supplemented by an important contribution from dissociative recombination of O_2^+. The results of the rocket measurements seemed to show that the

abundance of O_2^+ in aurora was insufficient and that the low energy electron flux was likewise too weak to excite the observed green line. Indeed by 1972 it appeared that no suggested process could explain the rocket measurements.

Feldman and Doering (1975) reported results from a further important 1972 Aerobee flight in which careful measurements of the low energy electron spectrum above 3 eV were made. This measurement and an independent one by Sharp and Hays (1974) indicated that the electron flux about 5 eV was almost an order of magnitude less than predicted by the current models. Feldman (1978) reported an analysis of the optical emission profiles obtained on the same flight which traversed steady aurora and like the earlier Aerobee studies used an up-down photometer, (Dick and Fastie, 1969), to eliminate the effects of residual temporal intensity variations. This analysis confirmed the dominant role of energy transfer from $O(^1D)$ to O_2 in the excitation of the Atmospheric O_2 band and confirmed the difficulty of understanding the excitation $O(^1S)$.

Rees et al. (1976) compared rocket observations of incident electron fluxes and ground-based photometer measurements of 4278Å and 5577Å. Good agreement was found between the Rees and Jones (1973) model for 4278Å but not for 5577Å for which the calculated value was only about 1/3 of that observed; the result was attributed to some lack of understanding of excitation or quenching. A comparison of a coordinated satellite-rocket-ground observation by Rees et al. (1977) gave satisfactory agreement for the 5577Å and 6300Å OI emissions based on the "classical" excitation schemes but had some difficulty with 3914Å. However a further analysis by Sharp, Rees and Stewart (1979) using *in situ* data from the rocket flight for the same coordinated observation, led to the conclusions that the $N_2(A)/O$ reaction was needed to get agreement for 5577Å and that there was a deficit in the model

for 6300Å. The main reason for the change between the two analyses was the use of the measured low energy electron fluxes below 10 eV rather than the theoretically calculated values. Both the Rees and Jones model and a discrete energy loss model predicted up to 10x more flux than observed in the 1 to 10 eV region. Sharp and Torr (1979) re-examined the same measurements from a different point of view and also concluded that the $N_2(A)/O$ mechanism can account for the observed excitation. A further rocket flight giving emission profiles by passing through an auroral form was analysed by Deans and Shepherd (1976, 1978) and by Yau and Shepherd (1979). These authors also concluded that the $N_2(A)/O$ mechanism was important and necessary.

The apparent failure of the models to predict correctly the low energy electron flux and hence to over-estimate the contribution of direct electron impact excitation was to some extent compensated by an over-estimate of the importance of quenching of $O(^1S)$ by O. This error was pointed out by Slanger and Black (1981). Studies by Gattinger et al. (1985) and Gerdjikova and Shepherd (1987) show that the $N_2(A)/O$ mechanism, combined with the revised quenching rate, can provide a satisfactory explanation of the excitation of $O(^1S)$. The energy transfer process from $O_2(c^1\Sigma_u^-)$ proposed by Solheim and Llewellyn (1979) may, as noted by Vallance Jones et al. (1985), still be viable.

Major improvements in modelling methods have been developed over the past decade by Strickland et al. (1976) and Stamnes (1980,1981). Applications of these methods have resulted in work on the prediction of auroral intensity profiles by Strickland et al. (1983), Daniell and Strickland (1986), Hecht et al. (1989), Rees and Lummerzheim (1989) and Lummerzheim et al. (1989). Recent work by Strickland et al. (1989) and Solomon

et al. (1988) seems to show that the excitation of the 6300Å emission can be explained by the "classical" mechanisms. This implies that the apparent theoretical surplus of 5-10 eV electrons discussed above may really indicate a deficit at higher energies.

The ARIES campaign was intended to carry out further critical tests of excitation theory by using carefully coordinated rocket and ground-based measurements. It is difficult to compare the modelled and observed profiles in a straightforward and rigorous manner because, on the one hand, the measured particle fluxes and the optical profiles cannot usually be obtained simultaneously and consequently time variations may cause the two not to be strictly comparable. Moreover, it is not easy to make reliable simultaneous measurements of neutral atmospheric composition to use in the theoretical modelling. An important objective for ARIES was to make local measurements of atmospheric neutral composition so as to make the interpretation less dependent on neutral atmosphere models. Unfortunately experimental problems prevented reliable composition measurements. Nonetheless, the two rocket flights and the ground measurements of the campaign, provide useful tests of the theory for two contrasting situations, namely aurora excited by a soft flux producing maximum emission in 130-150 km range and a hard flux with a maximum below 100 km. The ARIES campaign was intended to obtain comprehensive data by means of techniques 3) and 4) described above.

The first technique was the classical one in which the optical emission profile is measured by a rocket-borne photometers viewing upwards along the direction of the earth's magnetic field along which the rocket trajectory is aligned as closely as possible. The emission profiles are derived by differentiation of the total measured intensity with respect to height while the exciting particle spectrum is measured directly by particle spectrometers

carried on the rocket. Provided that the auroral emission is sufficiently stable and uniform, a theoretical profile based on the particle spectrum obtained near apogee (where it is least influenced by atmospheric absorption) can be directly compared with the height profile measured during the ascent or descent through the emitting region. In addition to the work described in the previous paragraphs, auroral height profiles have been measured in this way by Bogdanov et al. (1981), Tarasova et al. (1981) and Yagodkina et al. (1981). In principle, direct measurements of the neutral composition, in and above the emitting region, may be made from the rocket. Time and spatial changes in auroral intensity can be corrected if the upward measured intensities are normalized to the sum of the intensities measured in the upward and downward directions (Dick and Fastie, 1969). This method can compensate for changes in particle flux provided the energy spectrum remains constant. The ARIES-A rocket flight employed this technique and the results are reported in a separate paper.

The second technique was foreshadowed by the ground-based triangulation study of Belon, Romick and Rees (1966) and the analysis of this by Rees et al. (1967). More recently Velichko et al. (1981) have reported height profiles and 2-dimensional intensity distributions for 4278Å, 5577Å and 6300Å using a chain of three ground-based meridian scanning photometers. Another interesting forerunner was the study of Evans et al. (1972) in which triangulation was attained by combining the measurements of a ground scanning photometer, a rocket photometer and the latitudinal location of an auroral form as given by the particle measurements. As employed in the present study, this technique, in principle, overcomes the problem of temporal variation by making continuous measurements of the emission height profiles by means of a line of meridian scanning photometers on the ground while the particle spectrum is measured from the rocket.

The ARIES-B payload was launched on February 28 1984, to fly over an evening auroral arc system drifting equatorwards over the observing region. The aurora proved to be of an interesting type excited by relatively soft electrons characterized by IBC 1-2 bands with peak emission heights in the 130-150 km range.

The geometry for the ARIES-B experiment is shown to scale in Figure 1. To a good approximation, the ground photometer line and the plane in which these photometers scan, is also the plane of the rocket trajectory for which the azimuth is chosen in the direction of the horizontal component of the magnetic field. Consequently measurements of the rocket instruments can be directly related to optical emissions in the plane of observation. In addition to the ground photometers, the rocket carried photometers pointing perpendicular to the spin axis which was oriented perpendicular to the trajectory plane. Thus, the photometers obtained "meridian scan" data from which the auroral intensity distribution in the plane of the trajectory may be derived. In the ideal case, the rocket should be flown over a simple stable arc so that the information from the either the ground or rocket photometers would be sufficient to define the auroral intensity distribution. For the normal real situation, the aurora may be expected to move during the rocket flight so that the additional information from the ground photometers can be used to refine the solution for the intensity distribution to correlate with the particle measurements. This was the technique which was employed in the ARIES-B flight. The array of experiments carried was highly redundant, so that despite the failure of some instruments, the flight was highly successful in characterizing the height profile of an evening auroral arc and in comparing this profile with the predictions of an auroral excitation model.

Two types of comparison were possible. First, the primary electron spectrum measured near apogee was used to predict model profiles for the

4709Å or 3914Å N_2^+ bands and the 5577Å and 8446Å OI lines which were compared with the profiles derived from the ground-based photometer line and from the rocket photometers. Secondly the electron density measured along the trajectory on the downleg which passed through a second auroral band was compared with models based on the *in situ* measurements of the N_2^+ bands from the rocket and from the ground-based tomography.

All the experiments and results are summarized in this paper while detailed descriptions of the particle, photometer and plasma probe measurements on the rocket are given in other referenced papers, already published, in press or in preparation . The results and tomographic analysis from the chain of ground based photometers are described in detail in this paper as well as a simple modelling approach to the derivation of height profiles.

2. INSTRUMENTATION

2.1 Particle Detectors

Two electron spectrometers were provided by the Dr. D.J. McEwen of the University of Saskatchewan to measure electron fluxes. The first was a soft electron spectrometer which measured fluxes in the range from 28 eV to 22 keV with a scan period of 302 ms and a resolution of 0.15. The spectrometer viewed a 10° field perpendicular to the rocket spin axis which was almost exactly perpendicular to the terrestrial magnetic field and consequently the instrument obtained a complete pitch angle distribution for every rocket rotation (0.4 s). The second instrument was a suprathermal electron analyzer which measured fluxes in the range 0.7 to 234 eV in 64 steps every 0.3 s with a resolution of 0.05.

Additional measurements were made with an energetic particle detector package provided by the National Research Council of Canada (NRCC). This consisted of four electrostatic analysers measuring electron intensities at 0.10, 0.47, 1.7 and 7.7 keV, a solid state particle detector which measured integrated electron flux with energy thresholds of 20 and 37 keV and two electrostatic-analyser spectrometers for measuring 0.06 to 22 keV electron fluxes in 16 logarithmic steps. One of these was mounted at 45° and the other at 90° to the rocket spin axis.

A detailed account of these instruments will appear in a forthcoming paper by McEwen et al. (1991).

2.2 Rocket Photometers

Two radially pointing filter photometers were included in the payload. These were fixed photometers designed to perform scans in the

plane of the flight trajectory as a consequence the spin of the rocket. They were of conventional design with a full fields of view of 5° and passbands centered at 5577Å and 3914Å. The filter for the 3914Å photometer had a passband (FWHM) of 50Å. A full description of the 3914Å data is provided in the paper by McDade et al. (1991). The data from the 5577Å photometer suffered from some telemetry problems which have not yet been completely overcome.

2.3 Plasma probe experiment.

Plasma density and electron temperature measurements were obtained with a spherical electrostatic probe mounted on a boom extending perpendicular to the rocket. Details of the experiment and the analysis of the current-voltage data obtained are given by Margot and McNamara (1991).

2.4 1° Meridian Scanning Photometers (MSP's)

Three identical photometers were used at the three ground stations shown on Figures 1 and 2. These instruments had 12-in diameter f/4 plano-convex objective lenses which focussed the sky on to a circular 0.83 inch stop behind which a 12-channel filter wheel rotated at 20 Hz. The filter channels and their characteristics for the three 1°-photometers are listed in Table 1. The flux passing the filters was focussed on the Ga-As cathode of a Hammamatsu R94302 photomultiplier. Pulse-counting and gating electronics were used to separate the output of the channels and the data were recorded on tape for later analysis. The light from the sky was directed into the instrument by means of a rotatable plane mirror and baffle assembly driven by a stepping motor which provided the meridian scan. Each instrument has a circular field of view with a diameter of 1.0°. The stepping motor was controlled by a micro-processor to provide a scan rate of about 9°/sec so that adjacent samples are separated by 0.5°. The scan angle ranges of the photometers were adjustable. For the ARIES-B flight the two northern photometers were set

to scan a range of 90° in elevation angle and the southern one to 180°. In order to cover the the latitude region near the rocket trajectory, the starting elevation angles (measured from the north horizon) were set at 70°, 30° and 0° for the three photometers as indicated on Figure 1. The time for each complete data cycle was 24 sec which permitted the northern photometers to complete two scans and the southern one a single scan. The scan fly-back consumed about 17% of the observing time.

As noted above these instruments were set out on a line along the planned rocket trajectory direction which also lay close to the local direction of the horizontal component of the terrestrial magnetic field. The geometry in the plane of the trajectory is shown in Figure 1 while the location of the stations and trajectory are shown in the map reproduced as Figure 2.

2.5 Other ground-based photometers

Also deployed at the three ground stations, were the three meridian scanning photometers described by Vallance Jones et al. (1982). These provided meridian scans on the 6300Å [OI] line and Hβ as well as giving real-time scan data to help in selecting launch conditions. In addition the 15-channel zenith photometer described by Vallance Jones et al. (1987) was set up at Churchill. A further multi-channel meridian scanner was operated at Churchill by Dr. D.J. McEwen of the University of Saskatchewan.

2.6 All-sky TV system

The ISIT all-sky TV system described by Vallance Jones and Gattinger (1981), was set up at the launch site at Fort Churchill to assist in following the development of aurora and selecting launch conditions. A second all-sky TV was provided and operated at Churchill by Dr. D.J. McEwen of the University of Saskatchewan to assist in the interpretation of the Saskatchewan meridian scanner and rocket data.

2.7 Other experiments

Several other experiments were flown on the rocket and in some cases produced data which, however, were not used in the analysis either because the final data are not yet available or because of instrumental or telemetry problems. These included a two-channel auroral scanner, resonance lamps for the study of N and O atomic concentrations, 5200Å, 6300Å, 7320Å and 1.27μ photometers and a polychromator to study far UV OI and N_2 LBH emissions. There was also a set of radially pointing photometers to measure O_2 Atmospheric bands in the 8600Å region.

3. GEOPHYSICAL CONDITIONS AND OVER-VIEW OF OBSERVATIONS

3.1 Auroral Conditions

The goal for the ARIES-B flight was to fly over a stable arc so that the rocket trajectory would enclose the region of aurora, preferably with the arc conjugate to the rocket at apogee. This is difficult because more than 4 minutes must elapse between the decision to launch and the arrival of the rocket at apogee. A review of earlier meridian scanner records suggested that the most predictable auroral arcs are those which occur in the evening and which often move steadily equatorwards. This motion is however not always uniform and fluctuations in intensity do occur.

Satisfactory conditions occurred on the night of February 28. The general development of the display, as measured by the 1° meridian scanner from Churchill is shown in Figure 3. which covers the period from 03:30 to 04:18. (Throughout this paper all times will be given in Universal Time.) The general pattern is that of an arc system, drifting equatorward with an average velocity of about 100 m/s. The figure shows that, between about 03:38, when the band was just north of the Churchill zenith, and 04:00 when it reached the Lee Lake zenith, there were intensifications centered around 03:38, 03:53 and 04:01 with weaker periods in between. At 03:50 and 03:57 additional bands appeared equatorwards of the main northern band and moved polewards to coalesce with the main band at about 03:54 and 04:00. By 03:52 the arc had reached an intensity of 8.6 kR of 5577Å and was located about 13° south of the Churchill zenith. The rocket was launched at 03:53:44.2 and reached apogee at 03:57:37. The general development of the aurora is shown again in the 1°-meridian Churchill scanner records reproduced in Figure 4. The rocket descended through the 100 km level at 04:00. As explained in the previous

section, the meridian scanner viewing-direction lies close to the rocket trajectory plane and consequently Figure 4 gives a quantitative summary of the aurora sampled by the rocket instruments. Figure 4 shows that the main arc had increased in intensity to about 10 kR as the rocket rose through the 118 km level but then decreased in intensity to about 7 kR by 03:55:46 when rocket had reached 146km. About this time a second arc of about the same intensity is clearly visible just equatorward of the northern form. At the time of apogee the footprint of the rocket was directly over the northern arc which had maintained its intensity. A new arc further south had replaced the earlier second form. From apogee down to 120 km the main arc moved equatorwards in step with the rocket footprint while the equatorward form moved northward so that the two forms appear almost to merge into one as the rocket passed through. The intensity had increased slowly from a minimum of about 6 kR just before apogee to about 13 kR during the downward passage through the aurora.

A sequence of pictures obtained from the ISIT all-sky TV camera which was used both to select the desired launch conditions and to document the aurora, is reproduced in the paper by Margot and McNamara (1991). This confirms that the overall pattern of the aurora was that of a band system moving equatorward during the time of the flight.

3.2 Rocket Trajectory and Manoeuvres.

The ideal geometry for the experiment, as described in the introduction, was closely approximated. The rocket trajectory is plotted on Figures 1 and 2 as described in 2.4 above. Figure 2 shows the location of the the ground stations and the projection of the rocket trajectory during the flight. This projection lies within 1.0° of the direction of the local magnetic field of which the declination between apogee and the 100 km magnetic footprint of apogee was close to 1.0° according to the GSFC980 model

(Wallis, private communication) A SAAB S19 guidance system was used to ensure both the precision of flight azimuth and to satisfy safety requirements. A Space Vector attitude control system was used to orient the spin axis of the rocket into a direction perpendicular to the plane of the rocket trajectory. This manoeuvre was completed at 03:55:21, at a height of 118 km, and from that time the roll axis azimuth was close to 268.5° with an elevation angle of -2.3°. The direction of the magnetic field and the rocket spin axis in the horizontal plane are shown by the arrows in Figure 2.

The planned spin period was 2 sec but the value attained was 0.405 sec. This increased spin rate was favourable to the performance of the 5577Å and 3194Å radially pointing photometers and the particle detectors. These instruments had high signal count rates and high telemetry sampling rates and consequently the temporal resolution was improved without loss of spatial resolution.

3.3 Particle measurements

The NRCC and the University of Saskatchewan energetic particle detector experiments both worked well and obtained data on angular and energy distributions during the flight. The data from the NRCC fixed energy particle detectors are summarized in Figure 5 which shows variations with time at energies of 0.1 0.5 and 1.7 keV. Detailed results of the particle measurements are given in the paper by McEwen et al. (1991) The electron flux spectra measured by the two electron spectrometers are discussed later.

3.4 Rocket optical photometers

The 3914Å radial photometer operated well and produced good data throughout the flight. The data reduction for the 3914Å photometer is described in the paper by McDade et al. (1991).

3.5 Ground-based photometers

The 1° meridian photometers along the Churchill-Lee Lake-Bird line

produced good data during the entire flight. These data contain scans for 5577Å with excellent signal-to-noise ratios. The 4709Å and 8446Å channels also produced useable data for tomographic analysis. The 4° field meridian photometers operated well and data from these instruments were used for the 6300Å emission.

The zenith photometers at Churchill provided measurements of the intensities in 15 channels as the arcs observed drifted southward before the rocket flight. Similar magnetic zenith data were obtained from the 4° meridian scanner records at Gillam for the period of the rocket flight.

3.6 Plasma probes

The plasma probe operated well during the flight. Profiles for both electron density and temperature were obtained on the downleg passage through the southern arc. The results are described in the paper by Margot and McNamara (1991). Comparison of the electron density results with modelled values are described below.

4. INTERPRETATION

4.1 Tomography from ground-based data

In this section we present the results of a determination of the two-dimensional volume emission rate distribution in the plane of the trajectory, from the data obtained from the meridian scans of the three ground stations. These data are complemented by meridian scans from the rocket with the radially pointing 3914Å photometer. In principle, it might be possible to combine the information provided by the rocket and ground photometers to provide the best overall solution. However because of the temporal changes in the aurora during the flight, the approach chosen was to perform the analysis separately for the ground-based and rocket data and then to compare the results.

4.1.1 Tomographic inversion procedure

The method used to invert the ground-based data, is based on the procedure described by Thomas and Donahue (1972) and Wasser and Donahue (1979). First, a set of 1 km x 1 km cells covering the region viewed by the ground photometers was defined and filled with an initial set of equal volume emission rates. Next, the volume emission rate in each cell along each line of sight from the first ground station was scaled so that the integrated value along the line matched the observed intensity in that direction. The new array was then smoothed horizontally and vertically. Next, these steps were repeated for the second and the third ground stations. The whole procedure was then iterated until a stable solution was obtained. In the calculation of the results presented, no corrections were made for extinction and scattering. One of us (RLG) has carried out extensive numerical

modelling tests of the effects of extinction and scattering for a variety of auroral distributions and on the basis of these, some corrections to the observed meridian scans were attempted. However, these corrections did not appear to improve the results of the inversion procedure and consequently the corrections were omitted in the final data analysed. It should be noted that, as may be seen from Figure 1, the elevation angles from the photometers to the important parts of the forms analysed were never less than 30°.

The method was applied to the signals from the 5577Å, 4709Å and 8446Å channels from the 1° photometers and for the 6300Å data from the other meridian photometers described in 2.5. Because the 1° photometer data is obtained during 24 sec cycles, the solutions apply to these predetermined scan intervals.

The result of the inversion procedure, applied, as an example, to the data from a time interval before the rocket launch, is reproduced in Figure 6. The dashed curves in the left hand panel show the observed meridian scans for the three ground stations. In this case, the scan from Churchill shows that the band was very close to the zenith and exhibited a simple, almost Gaussian, brightness profile in latitude. The views from Lee Lake and Bird approximate the classical auroral profile with a sharp lower border and a more extended upper region. The result of the tomographic inversion is shown in the right hand panel and, as might be expected, show a simple volume emission rate profile with a maximum near 133 km. The solid curves on the left hand panel show, for the three ground stations, the angular intensity distributions regenerated from the contours of the left hand panel. The solid and dashed curves are almost identical. Since any physically realistic change in the derived height or latitude distribution of the volume emission rate would degrade this agreement, one can be fairly confident that the tomographic contours derived are close to

being correct. A further detailed comparison of the original data, the regenerated data and the tomographic solution is presented later for the more complicated situation when the rocket was near apogee.

4.1.2 Application to the time of the rocket flight

Figure 7 summarizes the derived volume emission rate contours of the 5577Å emission, for a sequence of consecutive 48-second time intervals during the rocket flight. The contours for the 48-second intervals were obtained by averaging the results of the inversion of the data from two consecutive 24-second scans. This appeared to give better results than averaging the scans before performing the inversion.

The first two plots, for the time intervals from 3:55:36 to 56:24 and from 3:56:24 to 57:12, show the development of the aurora during the upleg part of the flight. As the rocket passed up through the northern edge of the aurora, the main band beneath the trajectory was double with the northern component peaking at about 160 km accompanied by a slightly lower and stronger equatorward component. In the second plot, centered at 3:56:48, as the rocket was approaching apogee, both forms weakened slightly and a separate arc strengthened south of the trajectory. This southern arc had a peak height of about 140 km.

The next two plots, for 3:57:12 to 58:00 and 3:58:00 to 58:48, show the development of the aurora during the key period when the rocket was near apogee and located centrally above the electron flux producing the northern band. By this time the latter had become single again with a peak-volume emission rate height in the neighbourhood of 150-160 km. The previously noted southern band persisted strongly through the time near apogee and the height of its maximum appeared to lie between 130 and 140 km. A second southern arc appeared briefly at about 56.5°N latitude during the 3:57:00 to 58:00 interval.

The data plotted on Figure 4 show that the aurora remained rather stable from 3:57:22 to 58:10 except for a steady southward drift of the northern band. The electron fluxes of Figure 5 were also rather stable around this time, particularly from 3:57:36 to 58:24. It was a remarkable coincidence that, because the horizontal velocity matched the southward drift of the form, the rocket remained quite close to the field line connected with the arc (as seen from Figure 3).

The rocket remained close to apogee during this period, and consequently the time interval from 3:57:36 to 58:24 was chosen for a detailed comparison of the observed height distribution with the theoretical distribution calculated by the theoretical model from the observed electron flux. This comparison is presented in 4.3.

The last two frames of Figure 7, derived from scans obtained during the middle and lower parts of the descent phase, show that the northern peak weakened and almost coalesced with the southern form which itself continued to grow stronger. It appears likely that the *in situ* measurements obtained during the time interval of the last frame of Figure 7 correspond to the southern band. Clearly, the rocket did not intercept the particle flux exciting the southern form until it entered the edge of this form at a height below 140 km between 03:59:36 and 04:00:00. The measurements during this period of the flight are more fully discussed in 4.4.

The inversion procedure, described above, was applied to the meridian scans obtained simultaneously in the 5577Å and 8446Å OI lines and the 4709Å N_2^+ band for all the time intervals of Figure 7. In Figure 8, we reproduce the set of volume emission rate contour plots for the time near apogee selected for study i.e. between 3:58:36 and 3:59:24. A plot for 6300Å OI is also included in Figure 8. The differences between the distributions for the four wavelengths will be discussed in 4.3. In a manner

similar to Figure 6, we show in Figure 9 comparisons between the observed meridian scans from the three stations for each wavelength and the reconstructed scans recovered from the two 24-second tomographic inversions which were averaged to give the plots of Figure 8.

4.2 Tomography and height analysis of the rocket photometer data and comparisons with ground-based tomography.

The inversion of the data from the 3914Å radial rocket photometer is fully discussed in the paper by McDade et al. (1991). The results of this analysis may be compared with the ground results for the interval centered on 0359:34 when the rocket was near 140 km. The rocket result is shown in Figure 8 of McDade et al. At this time the rocket is between the two forms and the rocket photometer signal should be quite sensitive to the height distribution of the emission. The height profiles derived by McDade et al. and reproduced in their Figure 14, give peak volume emission rate heights of about 130 km for the southern form and 140 km for the northern one. Their height profile for the northern form is derived from their Figure 6 which gives a volume emission rate plot for a period centered on 03:58:57 when the rocket was at a height near 174 km. Their data for the southern form are reproduced by the open circles on Fig 10 while those for the northern form are reproduced in the same way on Figure 11.

Two other methods were used by McDade et al. (private communication) to obtain height profiles from the rocket data. Both these methods should give valid height profiles, corrected for variations in primary particle number flux, provided the there is little temporal variation in the energy distribution pattern.

The first method which was applied to the emission north of the rocket, was to use the northward horizontal signal versus height (with a correction for variations in total up-down intensity) to determine directly a profile

for the northern form. The validity of this method is dependent on the circumstance, (established by the ground data of Figure 7), that there is no appreciable additional auroral emission north of the rocket and the absence of significant temporal variation during the downleg below 160 km. This method gave a peak volume emission rate height of about 142 km. The profile obtained is reproduced as the solid curve on Fig 11.

The second method, applicable to the descent through the southern form, was to derive the volume emission rate profile by differentiation of the "up" signal after a correction for total intensity changes was made by dividing by the "up"+"down" signal This is essentially the method originated by Dick and Fastie (1969). This procedure gave a peak very close to 130 km; the complete profile so obtained is reproduced as the solid curve in Figure 10. It should be noted that the profile was scaled to the maximum "up-down" sum observed on the downleg and therefore represents the brightest profile crossed during the descent i.e. a vertical slice through the core of the southern form. This is to be distinguished from the height distribution of the local volume emission rate derived and discussed in 4.4.2 below.

The profile, for the southern arc, abstracted from the ground-based tomography described in 4.1, is also plotted on Figure 10. (The method for the ground-based profiles is described below in 4.3.3). The observed rocket profiles for 3914Å were converted to the volume emission rate for 4709Å by dividing by the transition probability ratio between the 0,0 and 0,2 bands. The profiles derived by the three methods agree well and indicate that the three techniques provide a good measurement of the height profile of the southern form at the time of the downleg passage through the aurora. The profile obtained by the ground-based method is slightly broader as might be expected as a

consequence of atmospheric scattering. The second maximum in the rocket profile obtained by the height differentiation method is not real but is a consequence of the rocket having sampled the higher altitude northern band as it descended through the 200 to 160 km region (see Figure 7). The tomographic rocket height profile is possibly affected by the temporal changes in the volume emission rate distribution documented in Figure 7.

Figure 11 shows a comparison, for the northern band, between the results of the two rocket techniques discussed above, (based on measurements during the downleg descent below 180 km), and the ground-based tomographic profile obtained earlier during the time near apogee. Because the latter curve refers to an earlier time it is likely that much of the difference between the rocket and ground-based curves is real. Moreover, the sidelook profile seen northward from the rocket, corresponds to the northern form with some contribution, at lower altitudes, from the southern band through which the trajectory passed. However, the ground-based results shown in Figure 7 do not indicate that the peak of the northern form ever dropped below 147 km so that there is a definite difference between the rocket profiles shown in Figure 11 and the final contour plots of Figure 7 which, we are inclined to believe, may be due to scattering from the stronger southern form as the two bands merge with one another. The ground tomography should be much more reliable at apogee time when the northern and southern forms were well separated. It should be noted that during the time interval when the rocket was near apogee, it did not move far enough to provide a great enough change in viewpoint for good tomography.

4.3 Modelling of height profiles of the northern arc observed near apogee

4.3.1 Apogee electron flux spectra

The ground and rocket tomography provide a good basis for selecting the time for a critical comparison of auroral properties, predicted by excitation

models, and the optical and other observations. As noted in 4.1, the time interval 0357:36 to 0358:24 is favourable since the rocket is close to apogee and magnetically conjugate with the northern arc. Electron energy spectra for this time interval are reproduced in Figure 12. This shows data, averaged over the pitch angle ranges 0-90° and 90-180°, both from the University of Saskatchewan soft electron spectrometer (McEwen, private communication) and from the NRCC electrostatic analyser. The data from the two instruments are identified as from Instruments A and B, respectively on Figure 12. According to the NRCC data, the pitch angle distribution is isotropic from 0-60° for the flux at 1.7 keV but has decreased by an order of magnitude by 120° while at 0.5 and 0.1 keV it is close to isotropic. The absolute accuracy of the data from the instrument A which was carefully calibrated before and after the flight is estimated to be about 10% (McEwen, private communication) while the calibration of instrument B is less certain but is believed to be accurate within a factor of 2.

In fact, the two sets of measurement agree to within a factor of 2 both in the magnitude of the differential flux and spectral distribution. The NRCC downward spectrum shows a peak at about 1.5 keV. This peak, although reproducible from one scan to another, does not appear in the more accurate data from the other spectrometer; the origin of the discrepancy is not clear.

In the modelling reported below, we have used both the McEwen downward electron spectrum which is identified as Spectrum A and the NRCC downward spectrum identified as Spectrum B. The differences in the calculated volume emission rates and peak heights for the two electron spectra provide an indication of the sensitivity of the profiles to the details of the primary electron spectrum.

4.3.2 Auroral excitation model

In order to make some preliminary comparisons between the observed profiles and theoretical predictions is was convenient to use the model described by Vallance Jones (1975). From this model, profiles for ion production rates, electron densities and some auroral feature emission rates may be calculated by means of the method described by Rees and Jones (1973). This procedure which is based on the assumption that the energy given to secondary electrons is deposited locally, is reasonably accurate at heights below 150 km for ion production rates and emissions from excited ions such as the N_2^+ 1N bands. This is illustrated by a comparison, in Figure 13 between profiles calculated in this way and by the more physically correct electron transport method which was developed by Strickland et al. (1976, 1983) . In this test the same model atmosphere (Jacchia (1977) with 1000° exospheric temperature) and the same electron fluxes were used. The results in Figure 13 show that, for total ionization rates, the local energy deposition model described gives satisfactory results within the range of energies and heights concerned in this study.

The application of the model to 5577Å and 8446 OIÅ OI emissions may not be so satisfactory. For the former, uncertainty as to the mechanisms for the excitation of this emission renders the modelled profile less reliable than for 4709Å N_2^+(1N). The theoretical profile was calculated by the method described by Gattinger et al. (1985) with the important production processes of $O(^1S)$ being collisional excitation of O by secondary electrons and energy transfer from $N_2(A)$ with an empirically chosen value of 20% for the yield of $O(^1S)$ in the $N_2(A)/O$ quenching reaction. There is no theoretical or laboratory justification for the latter choice except that it does give reasonable values for the $I(5577Å)/I(N_2^+(1N))$ ratio and reproduces an approximately constant ratio for the corresponding volume emission rates with height as has often been observed. It should be noted

however that the laboratory measurements of the the yield for the $N_2(A)/O$ reaction are closer to 75% (Piper, 1982; De Souza et al., 1985). In the particular case examined in this paper, the agreement between model and observation would be improved by adopting a higher value for the yield factor (see Figure 16 *b*); unfortunately the model treatment of secondary electron fluxes is not rigorous enough nor is our knowledge of the atomic oxygen concentration sufficiently certain to justify fitting the results by adjusting the $O(^1S)$ yield factor.

The 8446Å profile was modelled by noting that the excitation cross section for electron impact (Gulcicek et al. 1988) is somewhat similar in shape to the cross section for $N_2(a)$ as used in the model. The 8446Å emission rate was obtained simply by proportion taking into account the ratio $[O]/[N_2]$ and the ratio of excitation cross section peaks for $N_2(a)$ and 8446Å OI. This procedure is no more than a first approximation, in that any differences in the 8446Å and $N_2(a)$ cross sections will lead to errors, as may radiative transfer effects in the cascade processes leading to the upper state of 8446Å OI.

Measured downward electron spectra from Figure 12 were used as input to the model. An MSIS86 atmosphere (Hedin, 1987) for the time of the flight was used.

No primary ion particle measurements were made but optical measurements of Hβ show that the contribution from proton excitation was small. Hβ measurements from Bird indicate that the zenith intensity in the region of the forms measured in this study, was about 35R. According to the calculations of Van Zyl et al. (1984), the ratio I(Hβ)/I(4709) should be about 4 for protons of average energy 10 keV and 1.0 for 100 keV protons. Thus if the Hβ emission were produced by 100 keV protons, 35R of the observed integrated 4709Å intensity 14) might be due to proton excited emission. This would represent a possibly

significant 22% of the observed emission according to the data of Figure 14. (The profiles of Figure 14 were derived from the contours of Figure 8 as described in the next section.) However 100 keV protons produce a peak ionization rate near 105 km (Eather, 1970; Jasperse and Basu, 1982). A 22% component with a peak at this height would be quite noticeable in the 4709Å profile of Figure 14. If the $H\beta$ were produced by 10 keV protons the profile would be similar to that observed but the total contribution to the integrated 4709Å intensity would be reduced to about 6% so that the effect would be negligible. For the 5577Å profile no reliable theoretical calculations are possible but the measurements of Eather (1968) indicate that the ratio $I(5577)/I(H\beta)$ is typically about 10 so that the the zenith intensity due to protons would again be about 6% of the observed 5.9kR. Consequently it appears justifiable to neglect proton impact excitation in the modelling comparisons.

4.3.3 Comparison with Tomographic measurements.

As noted in 4.1, Figure 8 shows contour plots, from ground-based tomography, of the volume emission rates of the 5577Å, 6300Å and 8446Å OI lines and the 4709Å N_2^+ band. The first three contour plots correspond exactly to the time interval selected for analysis (as noted above) for 3:58:36 to 3:59:24. The fourth plot gives the volume emission rate distribution obtained by the same method for the 6300Å OI line for the period from 03:58:00 to 03:59:36. As described above in 2.5, the 6300Å data were obtained with a different set of meridian scanning photometers with an angular resolution of 4° (or better) and a scan repetition time of about 30 sec. Consequently, the results shown are not exactly comparable to those of presented in the first three panels of the figure. However, because of the longer radiative lifetime of the $O(^1D)$ state and the much more broader height profile of this emission the results shown should still be useful for comparison with those for the other

emissions.

Inspection of the plots of Figure 8 show that the contours for 5577Å OI and 4709Å N_2^+ are rather similar except that the latter are more noisy. The contours for the 8446Å OI emission peak at higher altitude and decrease more slowly with height than those for 5577Å OI and 4709Å. Although the contour plot for 6300Å is quite noisy the general distribution of 6300Å emission is centered over that of the other emissions but with profile which has a very broad maximum in the 180 to 250 km region.

As a final step in the analysis of the observations, field aligned profiles for the four emissions were calculated from Figure 8 by averaging the volume emission rates as a function of height along the magnetic field lines connecting to the rocket during the interval of the ground based observation. The positions of the rocket during the time period are shown by the black dots on the trajectory on Figure 8.

The observed tomographic profiles for the emissions are reproduced together in Figure 14. Intensity values, integrated up to 300 km, are given on the plots; the values in brackets are integrated to 200 km for comparison with the theoretical values which have an upper limit of 200 km, the height at which the particle measurements were made. It is striking that the observed 5577Å and 4709Å profiles are very similar, with a value of close to 37 for the I(5577)/I(4709) ratio which corresponds to about 7.4 for I(5577)/I(4278) on the basis of the 0,1/0,2 band transition probabilities.

An overview of the model profile results is given by Figure 15 which shows respectively the theoretical profiles for the 4709Å N_2^+(1N) band and the 5577Å, 8446Å and 6300Å OI lines. The profiles were calculated using the model described in 4.3.2 and the downward primary spectrum measured by Instrument A as reproduced in Figure 12. Because the measurements were made near 204 km, the flux was assumed to be incident at the 200 km level

in the model.

The scales for the 4709Å curves are the same in both the observed and model profiles. Apart from some irregularities in the tomographic profile the two height distributions are very similar in magnitude and general height distribution. The value of the ratio I(5577)/I(4709) of about 25 is somewhat lower that the observed value noted above. The model prediction for 8446Å shows a profile displaced upward by a significant amount and this is matched within experimental error by the observed profile. More detailed comparisons for each emission will next be described.

4.3.4 Detailed comparison of modelled and observed profiles

In Figure 16*a*, the model profiles computed are compared with the observed profile for the 4709Å $N_2^+(1N)$ emission. The observed profile has a peak volume emission rate a little higher than the theoretical profile based on the electron spectrum A and a little less than the theoretical profile based on spectrum B as defined in 4.3.1. The height distribution is somewhat similar for the observed profile and that based on the spectrum A. The profile based on the spectrum B is narrower, no doubt as a consequence of the peak at 1.5 keV in this spectrum.

A similar comparison was made for the 5577Å OI emission and the results are presented in Figure 16*b*. The observed peak volume emission rate for 5577Å is about double the modelled values based on electron spectrum A and about 40% greater than that based on electron spectrum B. Again the profile based on the spectrum B is somewhat narrower in its height distribution.

The modelled and observed profiles are reproduced for the 8446Å OI emission are reproduced in Figure 16*c*. The height distribution of the profile based on spectrum A agrees much better with the observed one than does that based on the spectrum B. As in the case of λ5577, the predicted

intensity is lower than observed.

Modelled and observed profiles for λ6300 are reproduced in Figure 16*d*. In the region below 180 km where the model might be expected to be valid, the profiles are similar with the observed emission rates being somewhat higher than the modelled values.

The result that both I(5577) and I(8446) are approximately double the predicted values could indicate an enhancement of [O] over the MSIS86 value used in the modelling. This is a possibility which will be subject to test when the predicted values can be recalculated using a more accurate model. In principle the 8446A observations should settle the question of the correct value for [O] and then the 5577A result could provide guidance for deciding the question of the excitation processes for O(1S).

4.4 Analysis of data from the southern arc traversed on the downleg

The profile for the three emissions can likewise be extracted from the ground-based tomography results for the southern form traversed during the downleg passage. These are reproduced in Figure 17. Again the 5577Å and 4709Å profiles almost identical with an intensity ratio close to 48 i.e. I(5[illegible] I(4278)≃9.6.

This value differs somewhat from the value of 7.4 derived in 4.3.3 from the northern arc profiles of Figure 14. If the difference is real, the simplest interpretation would be to ascribe the change to the greater mean height of the northern arc combined with a hypothetical decrease with height in the ratio $\eta(5577)/\eta(4278)$. However, for the profiles of Figure 17 this ratio appears, if anything, to fall off slightly more slowly with height. In the case of Figure 14 there is some tendency for the ratio to decrease with height as expected. The aurora was comparatively weak so it is hardly likely that the difference between the ratio for the two arcs can be ascribed to gross composition effects, although the somewhat higher average value of the

ratio for the two arcs (compared to the data of Vallance Jones and Gattinger (1972)) could be a composition effect. Another possibility is that the difference between the ratios of the integrated intensities may be due to some subtle instrumental effect possibly arising from residual differences in the calibrations of the three photometers. For these reasons we prefer to regard the difference between I(5577)/I(4278) ratios for the two arcs as being within the range of experimental error of the tomographic method and to adopt a value of 8.5 ± 1.0 as the best estimate.

It is interesting that the peak of the 8446Å OI emission is no longer displaced significantly above that of 5577Å and 4709Å although its volume emission rate falls off much more slowly with height.

As noted above, Figure 10 shows that the profiles of the southern arc obtained by rocket tomography and by up-down analysis of data on the downleg are all very similar. It is of interest to attempt to determine what primary electron spectrum would be consistent with these height profiles.

4.4.1 Derivation of primary electron spectrum from downleg measurements.

In order to determine what input primary spectrum could reproduce the observed profiles, a comparison was made by adjusting the primary electron flux spectrum until a satisfactory match was obtained with the N_2^+ profiles. The results for the best match to the points of the rocket tomographic profile of Figure 10 are plotted on Figure 18. The theoretical profile is for a Maxwellian primary flux spectrum with a characteristic energy of 0.5 keV accelerated by 2.0 keV. This gives the spectral distribution shown on the insert in Figure 20. It might be described as a slightly broadened 3 keV flux. An almost equally good match is obtained with a Gaussian primary flux centered on 3.0 keV with a full width at half peak of 2.0 keV. As a further test, the matching procedure was performed for the points of the ground tomography profile of Figure 10.

In this case the best matching primary spectrum was Maxwellian with a characteristic energy of 0.7 keV and an acceleration energy of 1.0 keV. The result is shown in Figure 19.

It is of interest to note that energy spectrum which appears best to fit the southern form approximates what would be obtained by accelerating the flux exciting the northern arc by a 1 to 2 kV potential drop.

The model curves for the 4709Å, 5577Å, 6300Å and 8446Å emissions obtained with the quasi-monoenergetic flux of Figure 18 (inset) are shown in Figure 20. Although the ratio of the volume emission rates of the 8446Å and 4709Å features increases steadily with height, the profile is so sharply peaked in this case that there is little upward displacement of the maximum of 8446Å. This contrasts with the behaviour with the softer fluxes of the northern form.

Margot and McNamara (1991) found reasonable agreement between their observed downleg electron density profile and a modelled profile calculated for a 3 keV monoenergetic flux. They also found general agreement between their electron temperature profile and a modelled profile based on the same primary electron flux. This does not necessarily mean that the actual exciting flux was 3 keV monoenergetic because there may be spatial and temporal components in the observed profile along the trajectory. It does indicate that the observed local electron densities and temperatures meaured are consistent with one another since in the steady state both the electron density and the electron temperature are determined by the ionization rate.

4.4.2 Modelling of electron densities from optical data on the downleg

The plot given by Margot and McNamara (1991) for the downleg is reproduced as the dash-dot curves on the right hand panels of Figure 21. It is important to note that this plot gives the local electron density measured along the trajectory. The most interesting part of the

trajectory below 180 km is covered by the last two plots of Figure 7 i.e. from 03:58:48 to 04:00:00. The variation of electron density versus height is influenced by the rocket motion in latitude which carries it from a position almost above the northern arc , across the "valley" between the two forms and then finally to descend just north of the core of the southern form. Thus the curve in Figure 21*b* is by no means a simple plot of n(e) vs. h along a field line although it probably approximates such a plot in the region of peak electron density.

The calculations to be described in the next paragraphs were carried out to test whether the observed electron densities could be understood in terms of the results of the ground-based and rocket tomographic plots.

In principle, the electron density along the trajectory can be calculated from the optical volume emission rate data of Figure 7. from which the temporal variation of $\eta(4709)$ and hence the ion production rate can be derived at points along the trajectory over the period of the flight. The time variation of the electron density at each point can then be computed with the help of a time dependent ion chemistry model such as that described by Vallance Jones et al. (1987). Finally theoretical values for the electron density can be picked out for the instants in time at which the rocket would have reached each point on the trajectory. These values can then be compared with the measurements from the plasma probe.

An input dataset for points on the downleg trajectory was prepared from data similar to that of Figure 7 except that the volume emission rate distributions were derived for the longer period from 03:54:00 to 04:00:00 at intervals of 24 sec (the basic repetition rate of the ground photometers). The 5577Å data was used to give the best signal-to-noise ratio A constant value of 10 was taken for the ratio $\eta(5577)/\eta(4278)$ as derived in 4.3.3 and 4.4

from the tomographic profiles based on longer periods of integration. The derived values of $\eta(4278)$ were interpolated at 4 sec intervals to provide a smooth input to the model. Ion production rates were derived from the values of of $\eta(4278)$ by means of the equations given by Vallance Jones (1964).

The resulting ion production rates for points along the rocket trajectory are plotted at 24 sec interval on Figure 21*a* as the dashed curves. The solid curve gives the values of the ion production rate as seen from the rocket i.e. it presents values, (abstracted from the complete $\eta_i(h,t)$ dataset), for the ion production rate, η_i, at the instant the rocket reaches each height level.

The time dependent ion chemistry model was then run using the complete $\eta_i(h,t)$ dataset starting at 03:54:00 for each height and the electron densities derived plotted as the dashed curves on Figure 21*b* in a similar way to Figure 21*a* . Again, the solid line gives the theoretical electron density which should have been encountered on the downleg.

The dash-dot curve on Figure 21*b*, gives the actual variation of electron density measured by Margot and McNamara. Clearly the modelled trajectory profile is seriously in error.

To discover the reason for the discrepancy, a check on the model was first carried out by computing the approximate equilibrium electron density from the solid curve of Figure 21*b* and employing the approximate relation,

$$n_e = \sqrt{(\eta_i/\alpha)} \qquad (1)$$

where η_i is the total ionization rate and α is the effective electron recombination rate coefficient as given by Wickwar et al. (1975) The n_e profile so calculated from the instantaneous ionization rate profile shown on Figure 21*a* is plotted as the dotted curve on Figure 21*b*. This profile is quite similar to the model profile given by the solid line. This indicates

that the ion production rates were varying slowly enough for the electron density to be quite close to the steady state values given by equation (1) and provides a check that the reaction rates used in the model are consistent with the effective recombination rates given by Wickwar et al.

It appears from Figure 21b that the electron densities inferred from the optical data are low by about 30% at the electron density peak and high above 150 km. One must conclude that the corresponding optical volume emission rates are underestimated by a factor of 2 near the peak of the profile and overestimated in the region above 150 km. The inversion procedure was repeated several times from different initial conditions without any substantial change in the result. Thus the discrepancy does not appear to be due to any failure of the inversion algorithm to yield a unique solution.

Although the profiles of Figure 10 show that there is good agreement between the ground and rocket tomographic profiles of the N_2^+ emission, there is a small but significant difference in the location of the rocket trajectory, relative to the maximum of the volume emission rate contours, in the last panel of Figure 7 and the corresponding Figure of McDade et al. (1991). According to the latter the rocket passed very close to the point of maximum emission rate while in to former the maximum lies slightly to the south. Thus, the ionization rate along the rocket trajectory shown in Figure 21a is significantly underestimated near 130 km. The geometry is also unfavourable along the upper part of the trajectory which, as may be seen from Figure 7, lies in region of volume emission rate minimum between the north and south forms above 150 km. Consequently it is not surprising that the derived volume emission rates in this region are less accurate.

It was found that an improved prediction of the electron density along the trajectory could be achieved by combining the ground-based optical data

with those from the rocket photometer. As noted earlier, the optical observations from the rocket are are not subject to errors due to atmospheric scatter. Moreover, as shown below, a good estimate of the local volume emission rate of the N_2^+ emission along the trajectory can be obtained directly from the rocket photometer data. On the other hand, the ground data can better take account of the temporal variations in the 2-dimensional volume emission rate distribution. Thus we assume

i) that the ground-based data should give the best estimate of the temporal variation of the ionization rate at points on the trajectory over the whole time period considered, but

ii) local measurements from the rocket should be used to calibrate the absolute value of the ground-based estimates.

The required local values of $\eta(3914)$ were obtained directly by multiplying the "up-down" profile of Figure 10 by the "up-down" sum used in the normalization which preceded the height differentiation. This reintroduces, along the trajectory, the spatial and temporal variation removed in the normalization. The solid curve in Figure 21c gives the resulting trajectory profile for η_1 derived from the values of $\eta(3914)$. The dashed curves on this figure show the data of Figure 21*a*, "calibrated" according to the solid curve. The time dependent model was then run with the renormalized ionization rate profiles to produce the curves of Figure 21*d* which are thus corrected versions of those of Figure 21*b*. The solid curve again gives the predicted electron density for the downleg while the dotted curve gives the equilibrium value based on equation (1).

The correction of the height profile on the basis of the rocket data leads to better agreement between the predicted and observed electron density profiles in the region of the peak. Indeed the modelled profiles fall off somewhat more rapidly with height than the observed one up to 170 km. The

higher value of the modelled electron density in the 190-200 km region is probably due to temporal variations of electron flux or energy distribution.

The conclusion from this above analysis is that the measured electron densities in the region of the downleg maximum are consistent with the optical measurements. One cannot infer the primary electron spectrum from the electron density profile except on the assumption that there was no latitude variation in precipitation.

4.5 Ground-based magnetic zenith measurements.

4.5.1 Measurements from Fort Churchill and Lee Lake

The magnetic zenith measurements from the specialized zenith-pointing instrument at Churchill and from the 4°. scanner at Lee Lake, provide an independent set of data which can be related to the overall interpretation of the event studied.

In the case of the Churchill observation, the measurement is of the passage of the arc system through the local magnetic zenith in the period from 03:35 until 04:00 when the rocket had descended to 100 km. As may be seen from Figure 3, there is a period of intensification in the magnetic zenith from about 03:37 to 03:45 followed by a short strong brightening about 03:51. This behaviour is reflected in the magnetic zenith intensities for λ5577, λ6300, and λ4278 which are plotted in the lower panel of Figure 22.In the middle panel are plotted the ratios I(5577)/I(4278) and I(6300)/I(4278). The former ratio remains almost constant in the range of 8 to 10 with no obvious change during the intensification of the aurora. However, the ratio I(6300)/I(4278) shows a significant decrease correlated with the auroral intensification.

The data given in Figure 22, obtained from the Churchill photometer before the launch, cannot be compared with certainty with the primary electron characteristics determined during the rocket flight. Nevertheless, because of

the apparent continuity of existence of the equatorward drifting arc system, it is of interest to compare the electron energies inferred from the zenith optical ratios with those measured by the rocket. Average electron energies were estimated from the I(6300)/I(4278) intensity ratio using the relation adopted by Vallance Jones et al. (1987) and are plotted in the upper panel of Figure 22. Values obtained fall in the range 1.5 to 2 keV both during the zenith passage of the band about 03:39 and during the later brightening about 03:51. This is somewhat higher than the energies measured by the rocket instruments which gave average energies in the range 0.9 to 1.2 keV. It very possible that this aurora was more energetic since it was brighter (I(5577)=5-7 kR) compared to the arc traversed near apogee (Figure 15).

For Lee Lake, the zenith data cover the growth and decay of the southern arc between 03:56 and 04:04. As seen from Figure 7, this arc appeared south of the Lee Lake zenith, intensified and moved poleward into the zenith. This is the form through which rocket descended, so that additional *in situ* measurements are available.The data for λ5577, λ6300, and λ4278 are plotted in Figure 23. As for the Churchill data, the I(5577)/I(4278) ratio remains almost constant (but in the range of 6 to 8) with no obvious change during the intensification of the aurora, while again the ratio I(6300)/I(4278) shows a significant decrease correlated with the auroral brightening. The λ4278 intensity before and after the intensification is about 200R and consequently the value of I(6300)/I(4278) at these times is probably less trustworthy (because of the possibility of scattering and background contamination) but the value at the time of peak intensity around 03:58:30 should be reliable.

The measurements presented in Figure 23, again cannot be compared directly with the rocket observations because as noted above the electron flux exciting the southern form was not directly measured. The

average energy of the incident flux from the observed values for the ratio I(6300)/I(4278) are plotted in the top panel of Figure 23. At the time of peak intensity the inferred average electron energy is about 3.0 keV. As noted above, this value is in agreement with the value inferred in 4.4.1 from the height distribution.

4.5.2 Discussion and comparison with tomographic results

It should be noted that the data presented in Figure 22 cover the period before the rocket flight when the arc system drifted southwards across the Churchill zenith, while the Lee Lake observations of Figure 25 give zenith intensity measurements of the southern arc through which the rocket passed on the downleg. The plots of Figure 7 show that this arc was moving northward during the time of the flight and crossed the Lee Lake field line about 03:58. The difference between the values of I(5577)/I(4278) above Churchill and Lee Lake can hardly be real and falls within the 10-15% absolute accuracy of the ground photometers. There is also a similar difference between the ground-based value from Lee Lake of about 7 for this ratio and that of about 9.6 from Figure 17. The zenith intensity of λ5577in Figure 17 is about 14 kR compared to the maximum value of about 7 kR in Figure 23. However from Figure 7 it is clear that the southern arc brightened by about a factor of 2 after it moved north of the Lee Lake zenith.

5. SUMMARY AND CONCLUSIONS

1. An auroral arc system excited by soft electrons, was studied with a combination of *in situ* measurements and optical tomographic techniques using data from a photometer on a horizontal, spinning, rocket and three meridian scanning photometers set out in a line under the rocket trajectory. The analysis was simplified in that the magnetic

field direction was approximately in the plane of the rocket trajectory and because the spin axis of the rocket was held perpendicular to this plane by an attitude control system.

2. The ground-based scanner data was successfully inverted to provide a set of volume emission rate distributions in the plane of the rocket trajectory with a time resolution of 24 or 48 seconds during the rocket flight. Results were obtained for the 4709Å, 5577Å and 8446Å emissions with supplementary distributions at 6300Å. Volume emission rate profiles, derived from these distributions peaked at about 150 km for 5577Å and 4709Å while the 8446Å peaked at about 170 km with a more extended height distribution.

3. The rocket photometer gave comparable volume emission rate distributions for the 3914Å emission as reported in a separate paper by McDade et al. (1991).

4. Instruments on the rocket measured the primary electron flux during the flight and in particular the flux precipitating into the auroral arc overflown at apogee (McEwen et al. 1991). The local electron flux and temperature was measured by probes on the rocket (Margot and McNamara (1991). The electron density measurements on the downleg were modelled using ion production rate data derived from the optical results.

5. Model calculations of the emission height profile based on the measured electron flux agree with the observed profiles.

6. The height distribution of the equatorward band through which the rocket passed during the descent, measured by the ground and rocket tomographic techniques are in good agreement. Comparison of this profile with model profiles indicates that the exciting primary spectrum may be represented by an accelerated Maxwellian or a Gaussian distribution

centered at about 3 keV. This distribution is close to what would be obtained if the electron flux exciting the poleward form were accelerated by a 1- 2 kV upward potential drop.

7. The relative height profile for the volume emission rate of the 5577Å OI emission is very similar to that of the 4709Å N_2^+ band for both the forms measured. The ratio for I(5577)/I(4278), obtained by integration of the tomographic profiles, was about 7 for the northern arc overflown at apogee and 10 for the southern arc at the time of downleg passage. The difference between these values may not be significant and we prefer an average value of 8.5 for the best estimate of this ratio from the rocket data.

8. Although no critical direct comparison was possible, the auroral intensities and the values of the intensity ratio, I(6300)/I(4278) measured in the magnetic zenith from the ground during the period before and during the rocket flight are consistent with the primary electron fluxes and height distributions measured from the rocket. The measured values for the ratio, I(5577)/I(4278) remained in the range 6 to 8 for Lee Lake and 8 to 10 for Churchill. It is likely that the difference between the mean values for the two stations falls within the 10-15% calibration error for the two different instruments. The overall average value of I(5577)/I(4278) again falls near 8.5, in agreement with the rocket measurements. This value is slightly higher than those reported by Gattinger and Vallance Jones (1964) and this may possibly indicate an enhancement of the atomic oxygen concentration at this low level of auroral activity. The values of I(5577) and I(8446) modelled using the electron flux spectrum measured at apogee are also significantly lower than those observed. This also would be consistent with values of [O] above those of the model atmosphere.

9. It would be desirable to repeat the modelling calculations with a more

sophisticated model to take full advantage of the results obtained. This is particularly true of the 5577Å and 8446Å height profiles for which the model employed is no more than a rough approximation. The comparison for λ8446 should provide some guidance as to the true concentration of atomic O so that the comparison for λ5577 might then provide a more critical test of the excitation mechanism of $O(^1S)$.

6. ACKNOWLEDGEMENTS

It is a pleasure to acknowledge the assistance of the personnel of the Canadian Centre for Space Research of the National Research Council in the planning both of the rocket flight and the ground station logistics for the ARIES campaign. In particular the essential role played by Mr. Hal Roberts, the Mission controller in the development and launching of the payload and Mr. Dale Crook in setting up the Lee Lake ground station. Likewise personnel at the Churchill Research Range played a vital part. National Research Council technical personnel responsible for the vital task of operating the ground-based instrumentation include Dale Tyler, François Gauthier, Don Bradley and John Vollenweider. Contributions are acknowledged from a number of scientists who participated in the planning of the campaign and in the provision of rocket and ground instrumentation. These include Drs. G. Witt, I. Robertson, L. Cogger, R. Van Es, G. Shepherd, W. Morrow, M. Morrow,J. McConnell,P. Forsyth, D.Wallis, B. Solheim, W. Ward, R. Wiens, B. Whalen, J. Hecht, A. Christensen and J. McDougall. We are especially grateful to Dr. D.J. McEwen and David Strauss for providing electron spectrometer data and for many useful discussions. The analysis of the ARIES-B rocket photometer measurements was supported at the University of Michigan by NASA grant NAG5-670. Work at the University of Saskatchewan was supported by the Natural Sciences and Engineering Research Council of Canada.

Table 1 Characteristics of filter channels of 1°-meridian scanners

Identifier	Spectral features transmitted		Peak Wavelength Å	Band-pass Å	Notes 2
4709Å	0,2 N_2^+ 1N		4709-10	19-20	
5275Å	2,0 O_2^+ 1N1N		5722-74	18-19	
5577Å	[OI]		5577-78	15-17	
6680Å	5,2 N_2	1P	6682-90	19-20	
7690Å	1,1 O_2	Atm	7693-96	19-21	
7725Å	2,0 N_2	1P	7726-29	20-22	
7775Å	OI		7775-79	21-22	
8445Å	OI		8447-50	21-22	
8576Å	Background		8572-82	21-23	
8624Å	0,1 O_2	Atm	8526-27	22-23	1
8682Å	NI		8685-87	21-22	1
8710Å	2,1 N_2	1P	8706-09	18-20	1

Note 1. These features are blended together.

Note 2. The wavelength ranges given span the variations between the values for the MSP's at the three ground stations.

CAPTIONS FOR FIGURES

Figure 1 Scale drawing of rocket the trajectory, the ground stations for the meridian scanning photometer chain and the contours of an idealized auroral emission cross section. The scan ranges of the ground photometers are indicated. The rocket roll axis was oriented perpendicular to the plane of the figure so that the radially pointing rocket photometers scan continuously as the rocket rotated. As may be seen from Figure 2, the ground stations and the rocket trajectory are very close to being co-planar.

Figure 2 Map showing projection of rocket trajectory, footprint and location of ground stations. The black-headed arrow shows the direction of the horizontal component of the magnetic field at apogee and the open-headed arrow shows the direction of the roll axis the rocket. The coordinates of the Mercator projection are geographic.

Figure 3 Grey scale plot of general development of the display as recorded by the 1° meridian scanner at Fort Churchill. The black points show the rocket footprint for a height of 150 km. This is close to the height of maximum 5577Å emission.

Figure 4 Meridian scan plots for 5577Å intensity from the 1° meridian scanner at Fort Churchill. The mid-times and rocket height for each 24-second scan are indicated. The zero for each successive plot is displaced upward by 4000 R.

Figure 5. Summary of fluxes measured by the fixed energy particle detectors of the NRCC experiment. Times and corresponding rocket heights are indicated.

Figure 6. Sample of tomographic inversion results for 03:38:00 - 03:38:24 Right hand panel. ------ 5577Å Intensity measured by the meridian

scanning photometers of the ground station line; _____ 5577Å intensity derived from the left hand panel which gives the volume emission rate contours derived by the tomographic inversion as described in the text.

Figure 7. 5577Å volume emission rate contours determined as for Figure 6 for period of rocket flight above 100 km. Each panel gives the results from the 48 sec period as indicated. The rocket trajectory is plotted on each panel with black dots indicating positions of the rocket during the ground scans. Contours are marked with values in photons/cm^3.sec.

Figure 8. Volume emission rate contours for 4709Å, 5577Å and 8446Å emissions for the apogee period from 03:57:36 to 03:58:24. A plot for the closest available period (03:58:00 to 03:58:48) for 6300Å is given in the fourth panel. It should be noted that the first three plots were produced by averaging the separate solutions for the the periods 03:57:36 to 03:58:00 and 03:58:00 to 03:58:24.

Figure 9. A comparison of observed scans and synthetic scans derived from the tomographically derived volume emission rate distributions from which the plots of Figure 8 were prepared. The observed and reconstructed scans for the two 24 second periods described in the caption for Figure 8, are presented separately, as panels *a* and *b*.

Figure 10 Comparison of height profile measurements for the southern form by rocket and ground-based methods; _____ height differentiation of the total intensity corrected upward rocket photometer signal; ○ tomographic inversion of rocket photometer "meridian" scans; -------tomographic inversion of data from ground meridian scanner chain.

Figure 11 Comparison of height profile measurements of the northern form by

rocket and ground-based methods; _____ rocket horizontal view method; O rocket tomography ;------- tomographic inversion of data from ground meridian scanner chain.

Figure 12 Electron spectra obtained near apogee for the period 03:57:36 to 03:58:24. by McEwen (private communication; McEwen et al. (1991)) (labelled Instrument A) and the NRCC experiment (labelled Instrument B). In each case spectra are given as averages over the pitch angle ranges 0-90° (down) and 90-180° (up).

Figure 13 Comparison of ionization rate profiles calculated by a local energy deposition model (Vallance Jones, 1975) and electron transport model of Strickland et al. (1983) for Maxwellian fluxes with the characteristic energies indicated and a Jacchia (1977) atmosphere with an exospheric temperature of 1000K.

Figure 14 Observed emission profiles for the 4709Å $N_2^+(1N)$, 5577Å, 6300Å and 8446Å OI emissions derived from ground-based tomography for the northern arc for the period 03:57:36 to 03:58:24 UT. Magnetic zenith values for the emission intensities, integrated to 300 km, are given on the plot; the values in brackets are integrated to 200 km for direct comparison with the model results.

Figure 15 Modelled volume emission rate profiles for the same features as for Figure 14 for the observed primary spectrum A for the apogee period 03:57:36 to 03:58:24 UT. Magnetic zenith intensities, integrated to 200 km are given on the plot.

Figure 16a Modelled and observed volume emission profiles for the 4709Å $N_2^+(1N)$ emission. The modelled profiles were calculated for the downward primary electron spectra of Figure 12 (identified as described in 4.3.1). The points for the observed profile are replotted from Figure 14.

b Similar to Figure 16*a* for the 5577Å OI emission.

c Similar to Figure 16*a* for the 8446Å OI emission.

d Similar to Figure 16*a* for the 6300Å OI emission.

Figure 17 Observed emission profiles for the 4709Å $N_2^+(1N)$, 5577Å, 6300Å and 8446Å OI emissions derived from ground-based tomography for the southern arc during the downleg passage for the period 03:59:36 to 04:00 00 UT. Magnetic zenith values for the emission intensities, integrated to 300 km, are given on the plot; the values in brackets are integrated to 200 km for direct comparison with the model results.

Figure 18 Match of profile of $N_2^+(1N)$ emission observed by rocket tomography by McDade et al. (1991) with profile modelled with accelerated Maxwellian spectrum as described in 4.4.1. The rocket profile was converted to the volume emission rate for the 4709Å band. Each curve is normalized to 1 at its peak. The inset shows a plot of of the primary flux spectrum used in the modelling.

Figure 19 Similar to Figure 18 except that the match is to the profile of the $N_2^+(1N)$ band derived by ground-based tomography as described in this paper. The parameters of the matching spectrum are given on the plot.

Figure 20 Model curves, as for Figure 15, but for the primary electron spectrum of Figure 18. Magnetic zenith intensities, integrated to 200 km are given on the plot.

Figure 21*a*. The dashed curves give the ionization rate profiles along the rocket trajectory at 24-second intervals derived from the optical data of Figure 7. The solid line is interpolated from the same data using the time-height table for the rocket and so gives the local ionization rate which should have seen by the rocket.

b. Electron densities (dashed curves) along the rocket trajectory calculated by time dependent model from the ionization rate variation given by panel *a*; the solid curve is the electron density which would have been seen by the rocket as interpolated from the dashed curves. The dotted curve is the equilibrium electron density derived from the solid curve of panel *a*. The chain-dot curve is the observed electron density along the trajectory as measured by the plasma probe (Margot and McNamara, 1991).

c. Similar to panel *a* except that the absolute value of the ionization rate at each height was scaled to agree with the values observed on the downleg by McDade et al. as described in the text.

d. Similar to panel *b* but derived from the scaled input data of panel *c*.

Figure 22 Magnetic zenith intensities of 5577Å, 6300Å and 4278Å emissions from Churchill (lower panel). Corresponding intensity ratios are plotted in the middle panel and energies inferred from the relation of Vallance Jones et al. (1987) in the upper panel. The observations extend back to the period before the flight when the arc system drifted southwards through the station zenith.

Figure 23 Similar to Figure 22 but for zenith measurements from Lee Lake obtained from the 4° meridian scanning photometer.

REFERENCES

Baker, K. (1968) Coordinated rocket measurements of auroral parameters. *Ann. Geophys.* 24, 285.

Belon, A.E., Romick, G.J. and Rees, M.H. (1966) Electron energy spectra from luminosity profiles of aurora. *planet. Space Sci.* 14, 597.

Bogdanov, N.N., Yagodkina, O.I., Tarasova, T.M., Davidov, V.S., Morozov, B.I., and Lazarev, A.I. (1981) Comparison of the behaviour of first and second positive systems of molecular nitrogen in polar aurora, Results of Researches on the International Geophysical Projects (Publishing House "NAUKA", Moscow), *Aurora and Airglow* 28, 40.

Cummings, W.D., Laquey, R.E., O'Brien, B.J. and Walt, M. (1966) Rocket borne measurements of particle fluxes and auroral light, *J. geophys. Res.* 71, 1399.

Daniell, R.E. and Strickland, D.J. (1986) Dependence of auroral middle UV emissions on the incident electron spectrum and neutral atmosphere, *J. geophys. Res.* 91, 321.

Deans, A.J., Shepherd, G.G. and Evans, W.F.J. (1976) Rocket measurement of the $O_2(b^1\Sigma_g^+ - X^3\Sigma_g^-)(0\text{-}0)$ band in aurora, *J. geophys. Res.* 81, 6227.

Deans, A.J. and Shepherd, G.G. (1978) Rocket measurements of oxygen and nitrogen emissions in the aurora, *Planet. Space Sci.* 26, 319.

De Souza, A.R., Gousset, G., Touzeau, M. and Tu Khiet (1985) Note on the determination of the efficiency of the reaction $N_2(A^3\Sigma)+O(^3P) \rightarrow N_2+O(^1S)$ *J. Phys. B* 18, L661.

Dick, K.A. and Fastie, W.G. (1969) Up-down photometers for auroral profile studies, *Applied Optics*, 8, 2457.

Donahue, T.M., Parkinson, T. and Zipf, E.C. (1968) Excitation of the auroral

green line by dissociative recombination of the oxygen molecular ion: analysis of two rocket experiments, *Planet. Space Sci.* 16, 737.

Eather, R.H. (1968) Spectral intensity ratios in proton-induced auroras, *J. geophys. Res.* 73, 119.

Eather, R.H. (1970) Ionization produced by auroral proton precipitation, *Ann. Géophys.* 26, 609.

Evans, D.S., Jacobsen, T., Maehlum, B.N., Skovli, G. and Wedde, T., (1972) Low energy electron precipitation and the ionospheric F-region in and north of the auroral zone, *Planet. Space Sci.* 20, 233.

Feldman, P.D., Doering, J.P. and Moore, J.H. (1971) Rocket measurement of the secondary electron spectrum in an aurora, *J. geophys. Res.* 76, 1738.

Feldman, P.D. and Doering, J.P. (1975) Auroral electrons and optical emissions of nitrogen, *J. geophys. Res.* 80, 2808.

Feldman, P.D. (1978) Auroral excitation of optical emissions of atomic and molecular oxygen, *J. geophys. Res.* 83, 2511.

Gattinger, R.L., Harris, F.R. and Vallance Jones, A. (1985) The height, spectrum and mechanism of type-B red aurora and its bearing on the excitation of $O(^1S)$ in aurora, *Planet. Space Sci.*, 33, 207-221.

Gerdjikova, M.G. and Shepherd, G.G. (1987) Evaluation of auroral 5577-Å excitation processes using Intercosmos Bulgaria 1300 satellite measurements, *J. geophys. Res.* 92, 3367.

Gulcicek, E.E., Doering, J.P. and Vaughan, S.O. (1988) Absolute differential and integral electron excitation cross sections for atomic oxygen. 6. The $^3P \rightarrow ^3P$ and $^3P \rightarrow ^5P$ transitions from 13.87 to 100 eV. *J.geophys. Res.* 93, 5885.

Hecht, J.H., Christensen, A.B., Strickland, D.J. and Meier, R.R. (1989) Deducing composition and incident electron spectra from ground-based auroral

optical measurements: variations in oxygen density, *J. geophys. Res.* 94, 13553.

Hedin, A.E. (1987) MSIS-86 thermospheric model, *J. geophys. Res.* 92, 4649.

Jacchia, L.G. (1977) Thermospheric temperature, density and composition: new models. *Special Report 375, Smithsonian Astrophysical Observatory, Cambridge, Mass.*

Jasperse, J.R. and Basu, B. (1982) Transport theoretic solutions for auroral protons and H atom fluxes and related quantities, *J. geophys. Res.* 87, 811.

Lummerzheim, D., Rees, M.H. and Anderson, H.R. (1989) Angular dependent transport of auroral electrons in the upper atmosphere, *Planet. Space Sci.* 37, 109.

Margot, J. and McNamara, A.G. (1991) Comparison of plasma density and electron temperature profiles during the auroral modelling campaign ARIES, *Can. J. Phys.* (accepted for publication)

McDade, I.C., Lloyd, N.D. and Llewellyn, E.J. (1991) A rocket tomography measurement of the N_2^+ 3914Å emission in an auroral arc, *Planet. Space Sci.* (in press).

McEwen, D.J., Strauss, D.L., Whalen, B.A. and Yau, A.W. (1991) An analytical study of measured electron influx and optical intensity for a steady aurora. (In preparation)

Parkinson, T.D. and Zipf, E.C. (1970) Energy transfer from $N_2(A3 +u)$ as a source of $O(^1S)$ in the aurora, *Planet. Space Sci.*, 18, 895.

Parkinson, T.D. (1971) A phase and amplitude study of auroral pulsations, *Planet. Space Sci.* 19, 251.

Parkinson, T.D., Zipf, E.C. and Donahue, T.M. (1970) Rocket investigation of the auroral green line, *Planet. Space Sci.* 18, 187.

Piper, L.G. (1982) The excitation of $O(^1S)$ in the reaction between

$N_2(A^3\Sigma_u^+)$ and $O(^3P)$, *J. chem. Phys.* 77, 2373.

Rees, M.H. and Jones, R.A. (1973) Time dependent studies of the aurora: II Spectroscopic morphology, *Planet. Space Sci.* 21, 1213.

Rees, M.H., Romick, G.J., Anderson, H.R. and Casserly Jr., R.T. (1976) Calculation of auroral emissions from measured electron precipitation: comparison with observation, *J. geophys. Res.* 81, 5091.

Rees, M.H., Walker, J.C.G. and Dalgarno, A. (1967) Auroral excitation of the forbidden lines of atomic oxygen, *Planet. Space Sci.* 15, 1097.

Rees, M.H., Stewart, A.I., Sharp, W.E., Hays, P.B., Hoffman, R.A., Brace, L.H., Doering, J.P. and Peterson, W.K. (1977) Coordinated rocket and satellite measurements of an auroral event: 1. Satellite observations and analysis, *J.geophys. Res.* 82, 2250.

Rees, M.H. and Abreu, V.J. (1984) Auroral photometry from the atmospheric explorer satellite, *J.geophys. Res.* 89, 317.

Rees, M.H. and Lummerzheim, D., (1989) Characteristics of auroral electron precipitation derived from optical spectroscopy, *J. geophys. Res.* 94, 6799.

Schmidtke, G., Stasek, G., Wita, C., Seidl, P. and Baker, K.D. (1985) Rocket-borne EUV and visible emission measurements, *J. atmos. terrest. Phys.* 47, 147.

Sharp, W.E. and Hays, P.B. (1974) Low energy auroral electrons, *J. geophys. Res.* 79, 4319.

Sharp, W.E. and Torr, D.G. (1979) Determination of the auroral $O(^1S)$ production sources from coordinated rocket and satellite measurements, *J. geophys. Res.* 84, 5345.

Sharp, W.E., Rees, M.H. and Stewart, A.I. (1979) Coordinated rocket and satellite measurements of an auroral event: 2. The rocket observations and analysis, *J.geophys. Res.* 84, 1977.

Shepherd, G.G. and Gerdjikova, M.G., (1988) Thermospheric atomic oxygen concentrations inferred from the auroral I(5577)/I(4278) emission ratio, *Planet. Space Sci.* 36, 893.

Slanger, T.G. and Black, G. (1981) Quenching of $O(^1S)$ by $O_2(a^1\Delta_g)$, *Geophys. Res. Let.* 8, 535.

Solheim, B.H. and Llewellyn, E.J. (1979) An indirect mechanism for the production of $O(^1S)$ in the aurora, *Planet. Space Sci.* 27, 473.

Solomon, S.C., Hays, P.B. and Abreu, V.J. (1988) The Auroral 6300Å emission: observations and modelling, *J. geophys. Res.* 93, 9867.

Stamnes, K., (1980) Analytic approach to auroral electron transport and energy degradation, *Planet. Space Sci.* 28, 427.

Stamnes, K., (1981) On the two-stream approach to electron transport and thermalization, *J. geophys. Res.* 86, 2405.

Strickland, D.J., Book, D.L., Coffey, T.P. and Fedder, J.A. (1976) Transport equation techniques for the deposition of auroral electrons, *J. geophys. Res.* 81, 2755.

Strickland, D.J., Jasperse, J.R. and Whalen, J.A. (1983) Dependence of auroral FUV ;emissions on the incident electron spectrum and neutral atmosphere, *J. geophys. Res.* 88, 80511.

Tarasova, T.M., Yagodkina, O.I., Bogdanov, N.N., Yevlashin, L.S., Mikirov, A.E. and Shidlovski, A.A. (1981) Height profile of polar aurora in the red and visible regions of the spectra according to measurements from Franz-Joseph Land, Results of Researches on the International geophysical Projects (Publishing House "NAUKA", Moscow), *Aurora and Airglow* 28, 44.

Thomas, R.J. and Donahue, T.M., (1972) Analysis of Ogo 6 observations of the OI 5577-Å tropical nightglow, *J. geophys. Res.* 77, 3557.

Vallance Jones, (1975) A model for the excitation of electron aurora and some applications, *Can. J. Phys.* 53, 2267.

Vallance Jones, A. and Gattinger, R.L. (1974) The intensity ratios of auroral emission features, *Ann. Géophys.* 28, 91.

Vallance Jones, A. and Gattinger, R.L. (1981) TV morphology of some episodes of pulsating aurora, *Can. J. Phys.* 59, 1077.

Vallance Jones, A., Creutzberg, F., Gattinger, R.L. and Harris, F.R. (1982) Auroral studies with chain of meridian-scanning photometers 1. Observations of proton and electron aurora in magnetospheric substorms, *J. geophys. Res.* 87, 4489.

Vallance Jones, A., Meier, R.R. and Shefov, N.N. (1985) Atmospheric quantal emissions: a review of recent results. *J. atmos. terr. Phys.* 47, 623.

Vallance Jones, A., Gattinger, R.L., Shih, P., Meriwether, J.W., Wickwar, V.B. and Kelly, J. (1987) Optical and radar characterization of a short-lived auroral event at high latitude, *J. geophys. Res.* 92, 4575-4589.

Van Zyl, B., Gealy, M.W. and Neumann, H. (1984) Prediction of photon yields for proton aurorae in an N_2 atmosphere, *J. geophys. Res.* 89, 1701.

Velichko, V.A., Samsonov, V.P. and Nadubovich, Ya.A. (1981) Vertical and horizontal profiles of the surface brightness of discrete aurora forms in 4278Å and 6300Å emissions, Results of Researches on the International geophysical Projects (Publishing House "NAUKA", Moscow), *Aurora and Airglow* 28, 27.

Wasser, B. and Donahue, T.M. (1979) Atomic oxygen between 80 and 120 km: evidence for a latitudinal variation in vertical transport near the mesopause, *J. geophys. Res.* 84, 1297.

Yagodkina, O.I., Bogdanov, N.N., Tarasova, T.M., Orlovla M.V., Mikirov A.E., and Kachekan, V.A. (1981) Height distribution of emissions of aurora in the near I.R. region, Results of Researches on the International geophysical Projects (Publishing House "NAUKA", Moscow), *Aurora and Airglow* 28, 47.

Yagodkina, O.I., Tarasova, T.M., Yevlashin, L.S. and Morozov, B.I. (1982)

Height distribution of Hα emission in the N_2 1PG at the latitude of the polar cusp, Results of Researches on the International geophysical Projects (Publishing House "NAUKA", Moscow), *Aurora and Airglow* 30,12.

Yagodkina, O.I., Tarasova, T.M., Yevlashin, L.S., Davidov, V.S. and Shedlovsky, A.A. (1982) Rocket measurements of the vertical profile emission of Hβ and of the background near 14600Å at high latitudes, Results of Researches on the International geophysical Projects (Publishing House "NAUKA", Moscow), *Aurora and Airglow* 30, 20.

Yau, A.W. and Shepherd, G.G. (1979) Energy transfer from excited N_2 and O_2 as a source of $O(^1S)$ in the aurora. *Planet. Space Sci.* 27, 481.

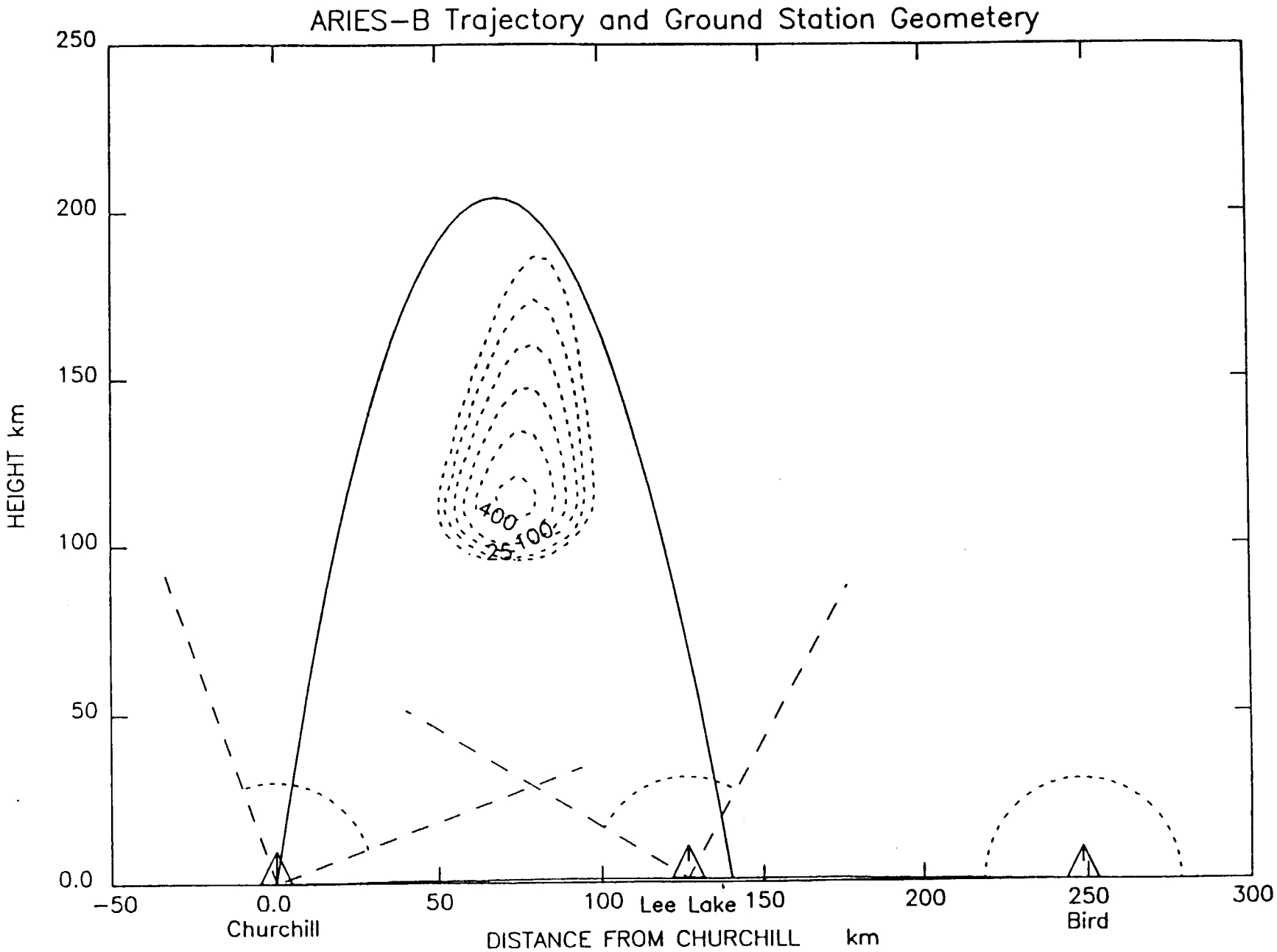

NAG5-670 'C' 58 Fig. C1

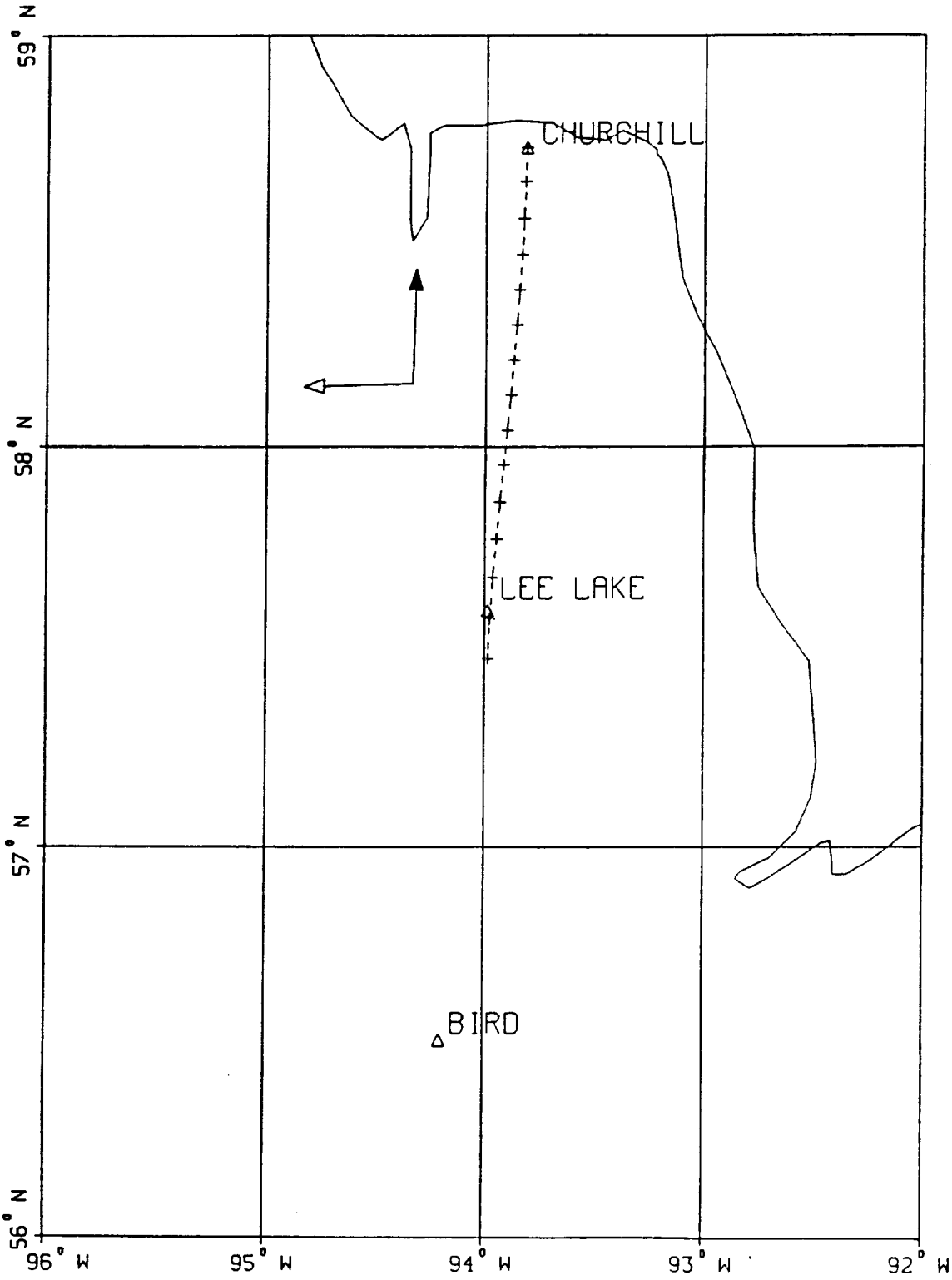

NAGS-670 'C' 59 Fig. C.2.

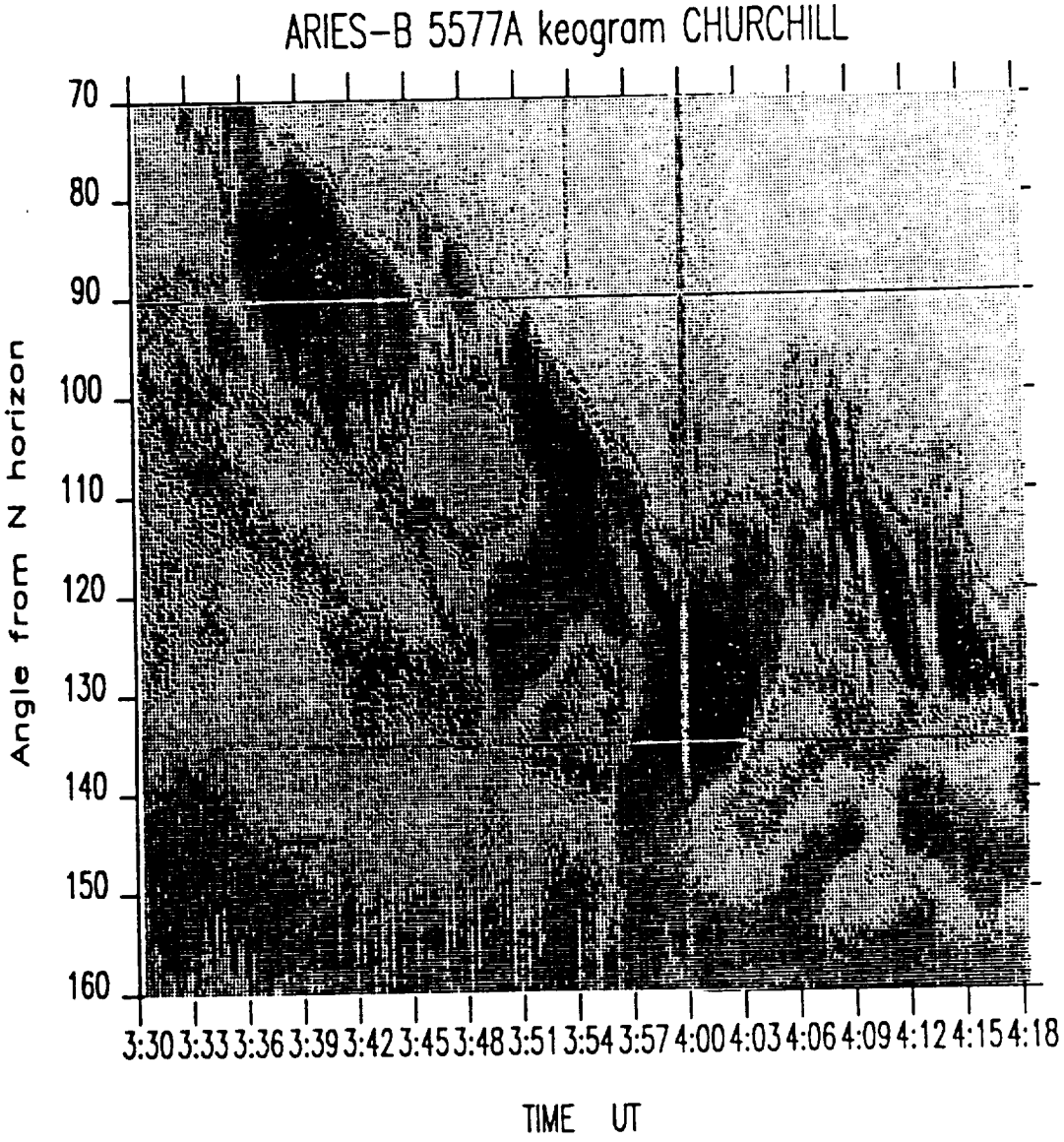
ARIES–B 5577A keogram CHURCHILL
Angle from N horizon
70
80
90
100
110
120
130
140
150
160
3:30 3:33 3:36 3:39 3:42 3:45 3:48 3:51 3:54 3:57 4:00 4:03 4:06 4:09 4:12 4:15 4:18
TIME UT

Fig. C3

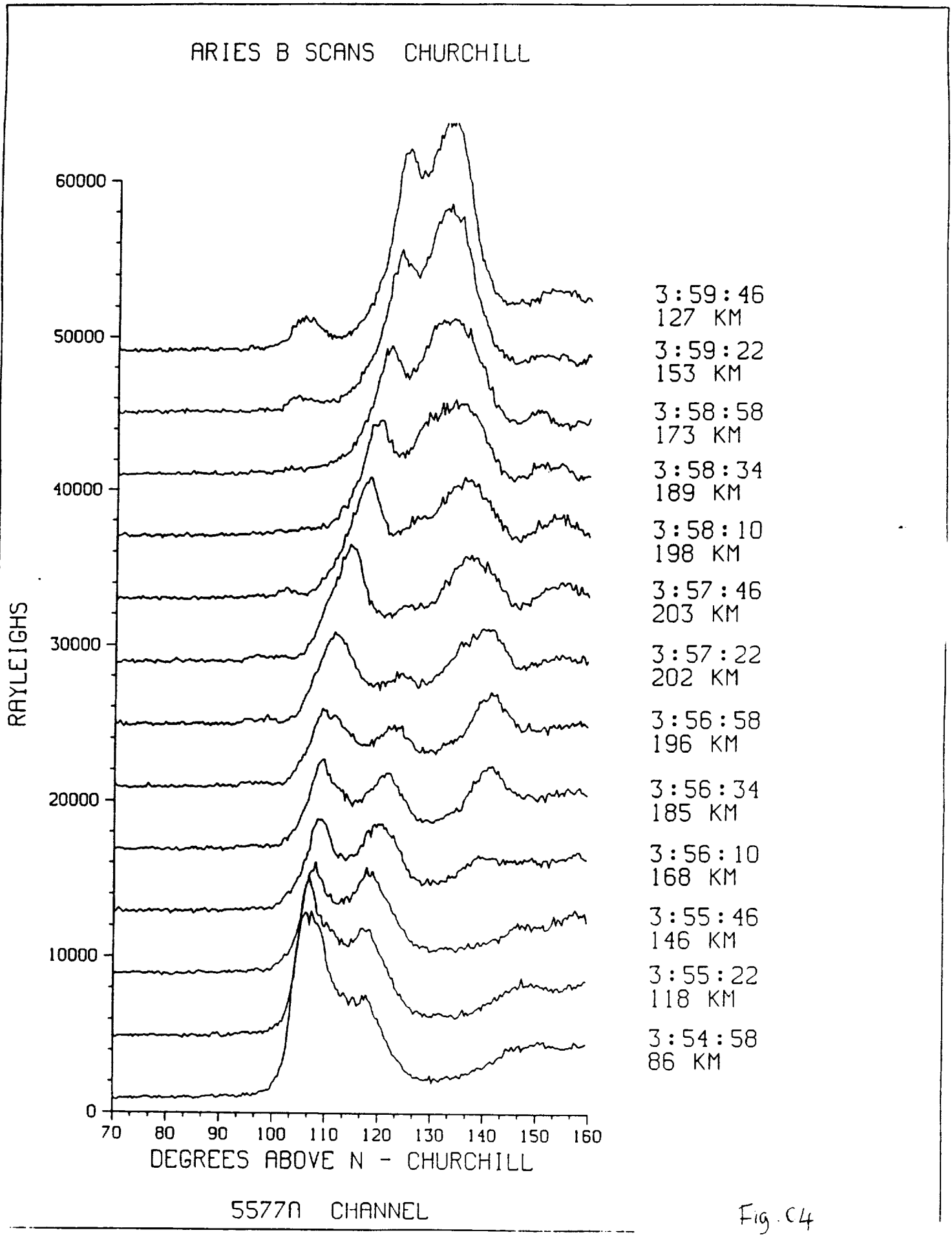
ARIES B SCANS CHURCHILL
60000
50000
40000
30000
20000
10000
0
RAYLEIGHS
70
80
90
100
110
120
130
140
150
160
DEGREES ABOVE N - CHURCHILL
3:59:46
127 KM
3:59:22
153 KM
3:58:58
173 KM
3:58:34
189 KM
3:58:10
198 KM
3:57:46
203 KM
3:57:22
202 KM
3:56:58
196 KM
3:56:34
185 KM
3:56:10
168 KM
3:55:46
146 KM
3:55:22
118 KM
3:54:58
86 KM
5577Å CHANNEL

Fig. C4

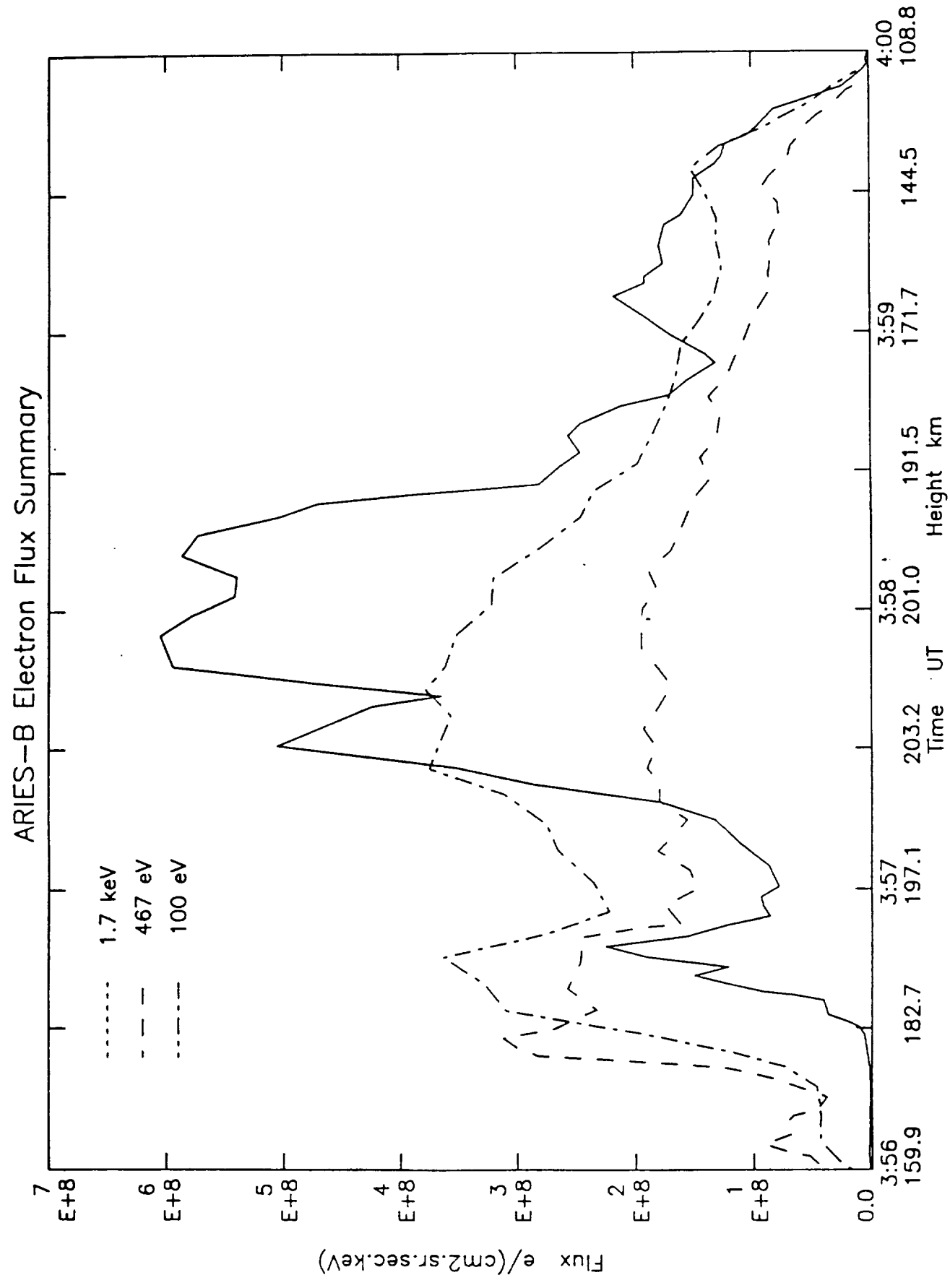
ARIES–B Electron Flux Summary
1.7 keV
467 eV
100 eV
Flux e/(cm2.sr.sec.keV)
7 E+8
6 E+8
5 E+8
4 E+8
3 E+8
2 E+8
1 E+8
0.0
3:56 159.9
182.7
3:57 197.1
203.2
3:58 201.0
3:59 171.7
191.5
4:00 108.8
144.5
Time UT
Height km

Fig. C5

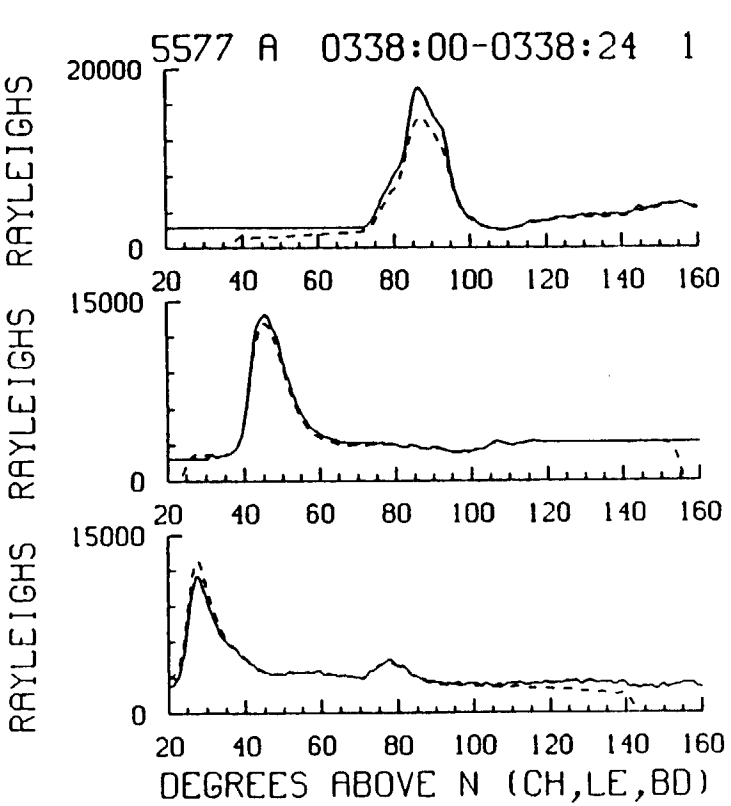

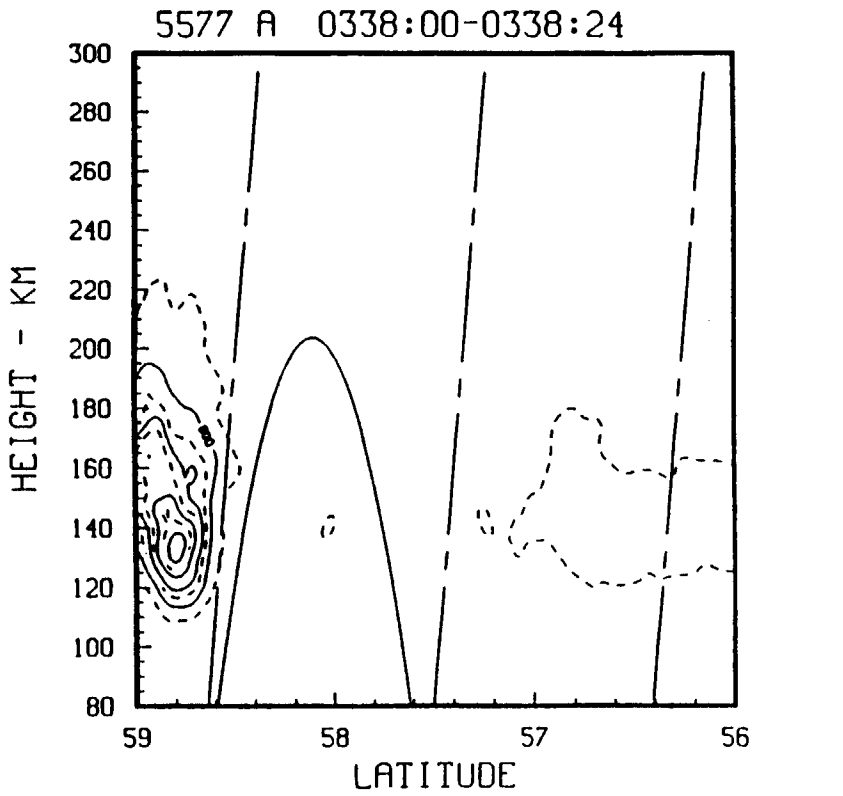

5577 EMISSION IN PHOTONS/CM3-SEC

Fig. C6

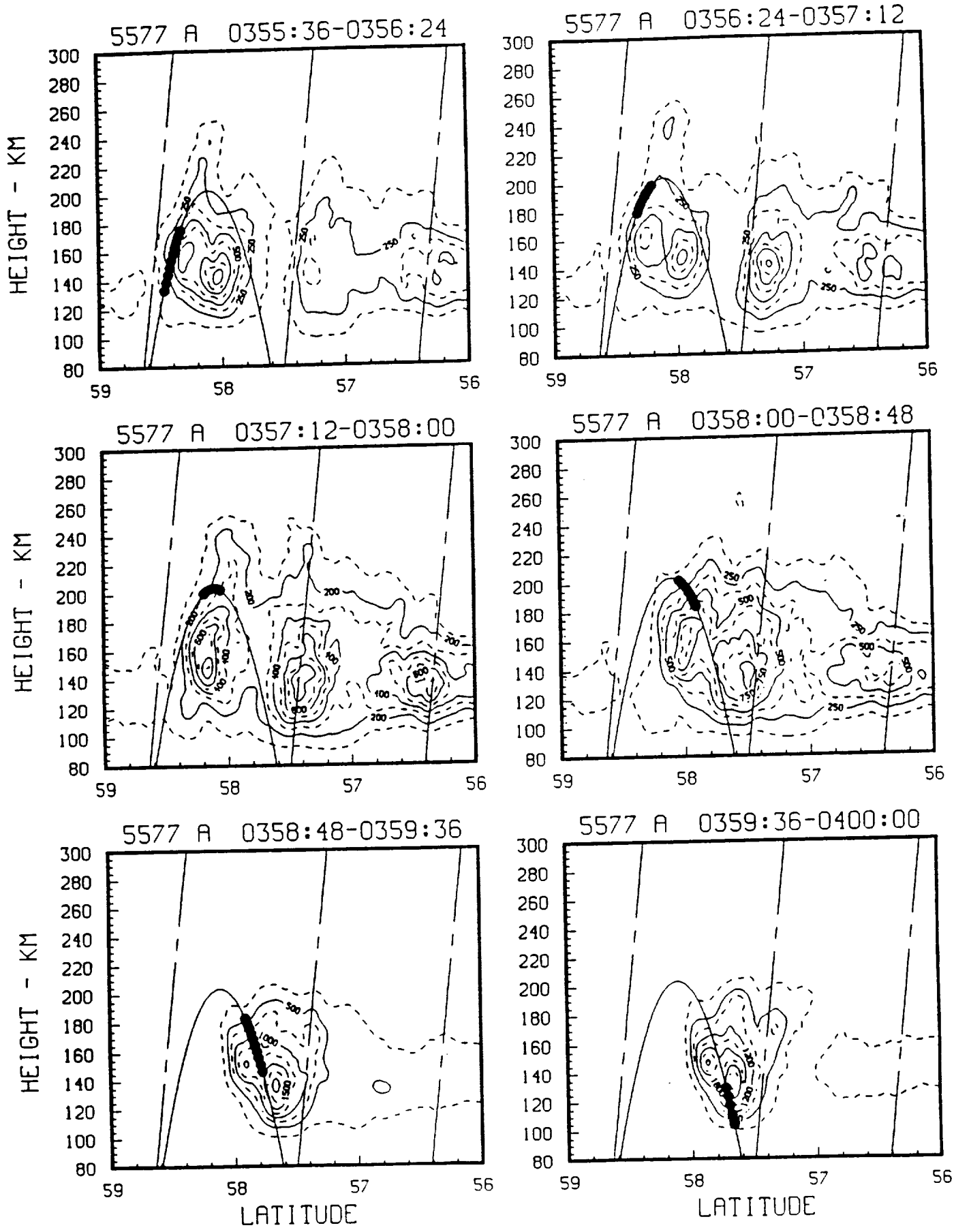

NAG5-670 'C' 64 Fig. C7

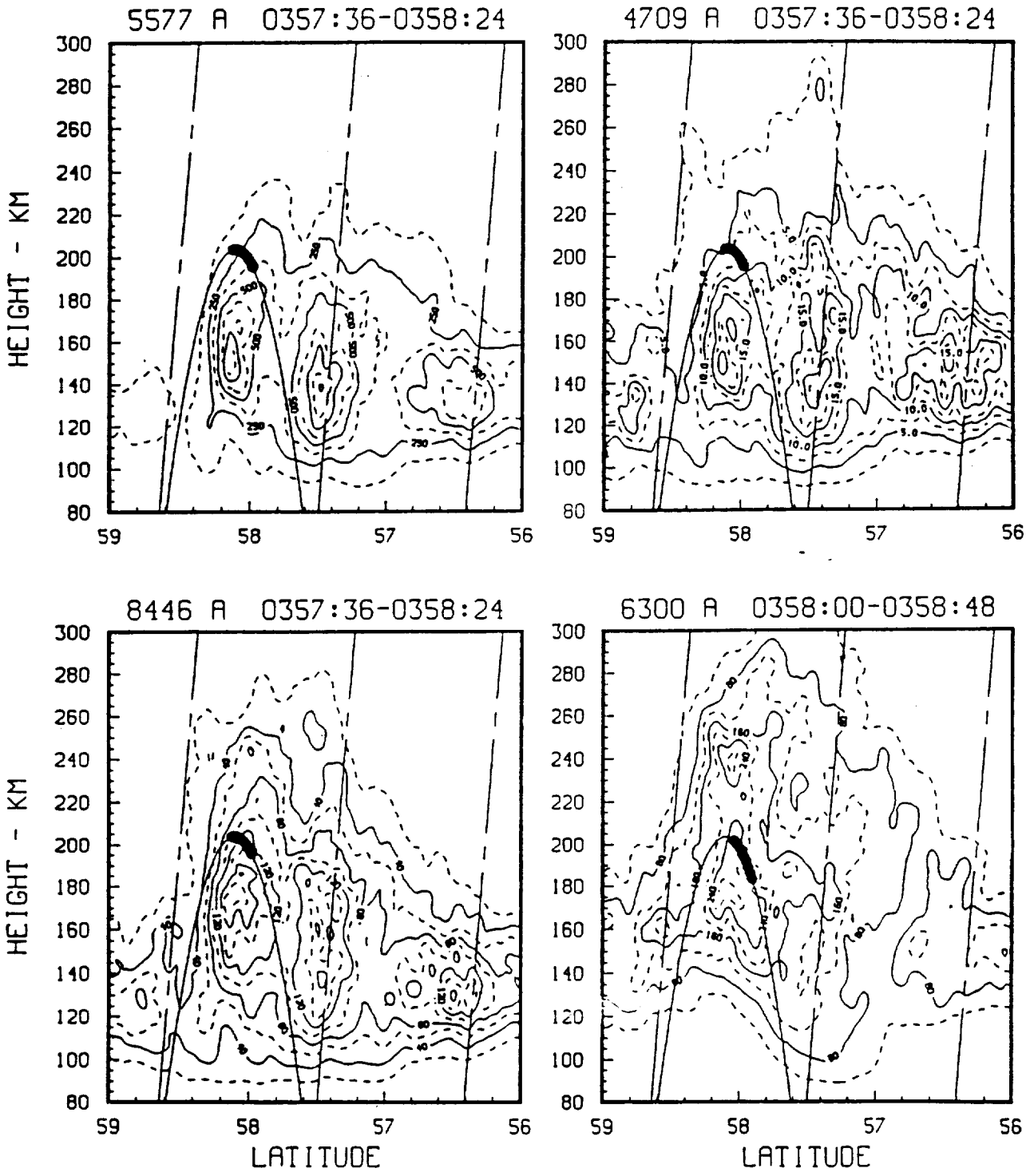
5577 A 0357:36-0358:24
4709 A 0357:36-0358:24
8446 A 0357:36-0358:24
6300 A 0358:00-0358:48
HEIGHT - KM
LATITUDE
300
280
260
240
220
200
180
160
140
120
100
80
59
58
57
56

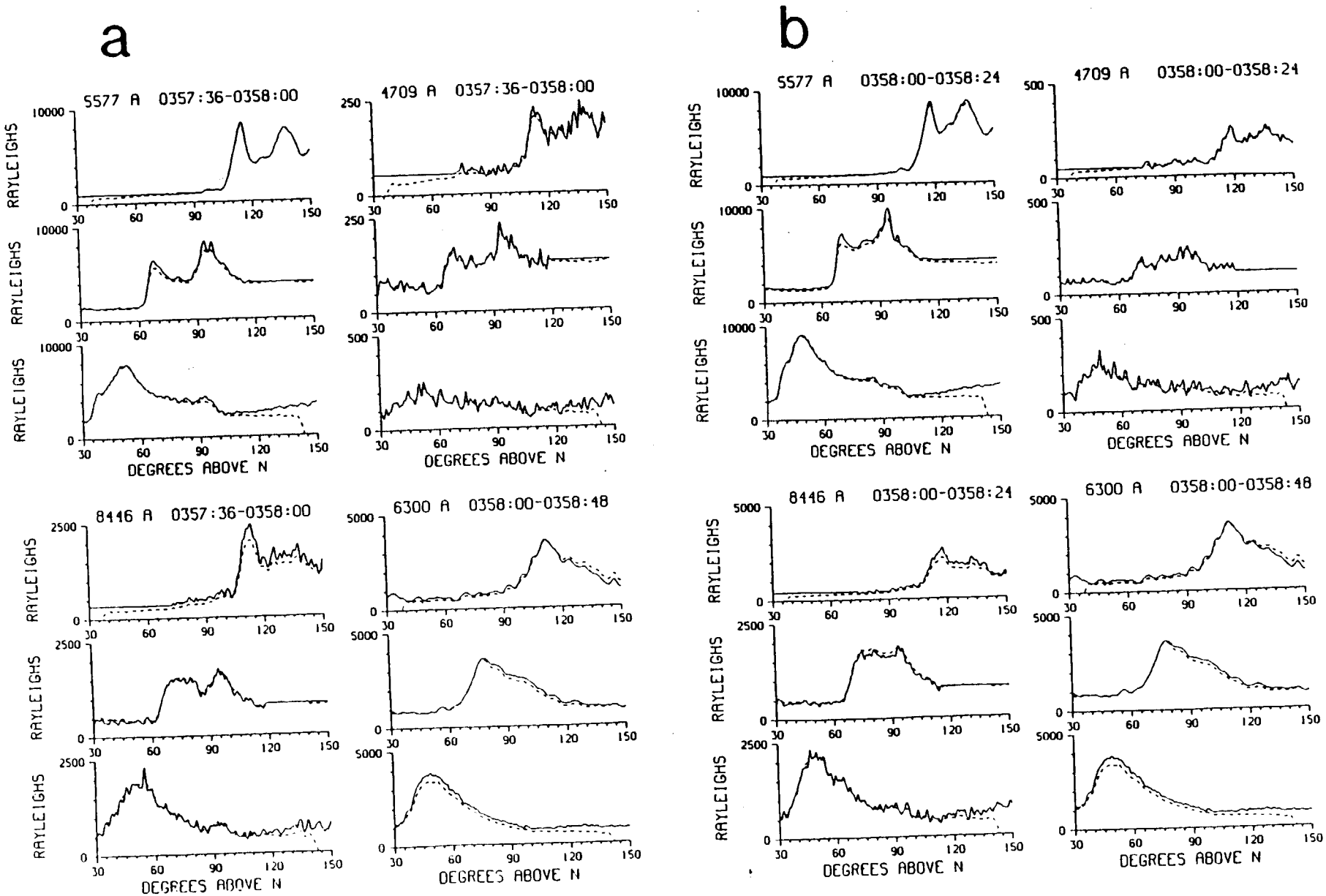

NAG5-670 'C' 66

Fig. C9

TOMOGRAPHIC AND ROCKET DATA
SOUTHERN FORM

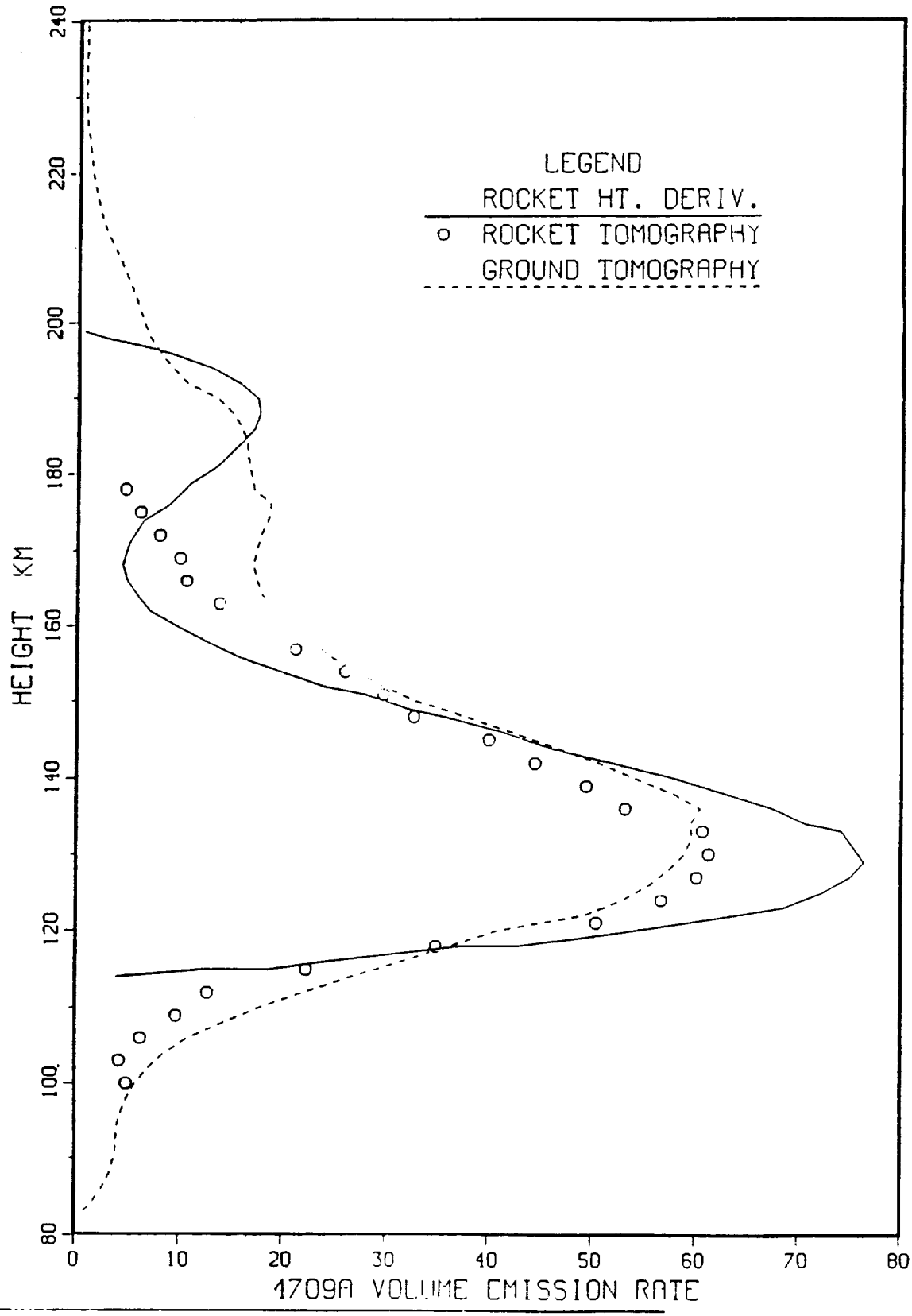

TOMOGRAPHIC AND ROCKET DATA
NORTHERN FORM

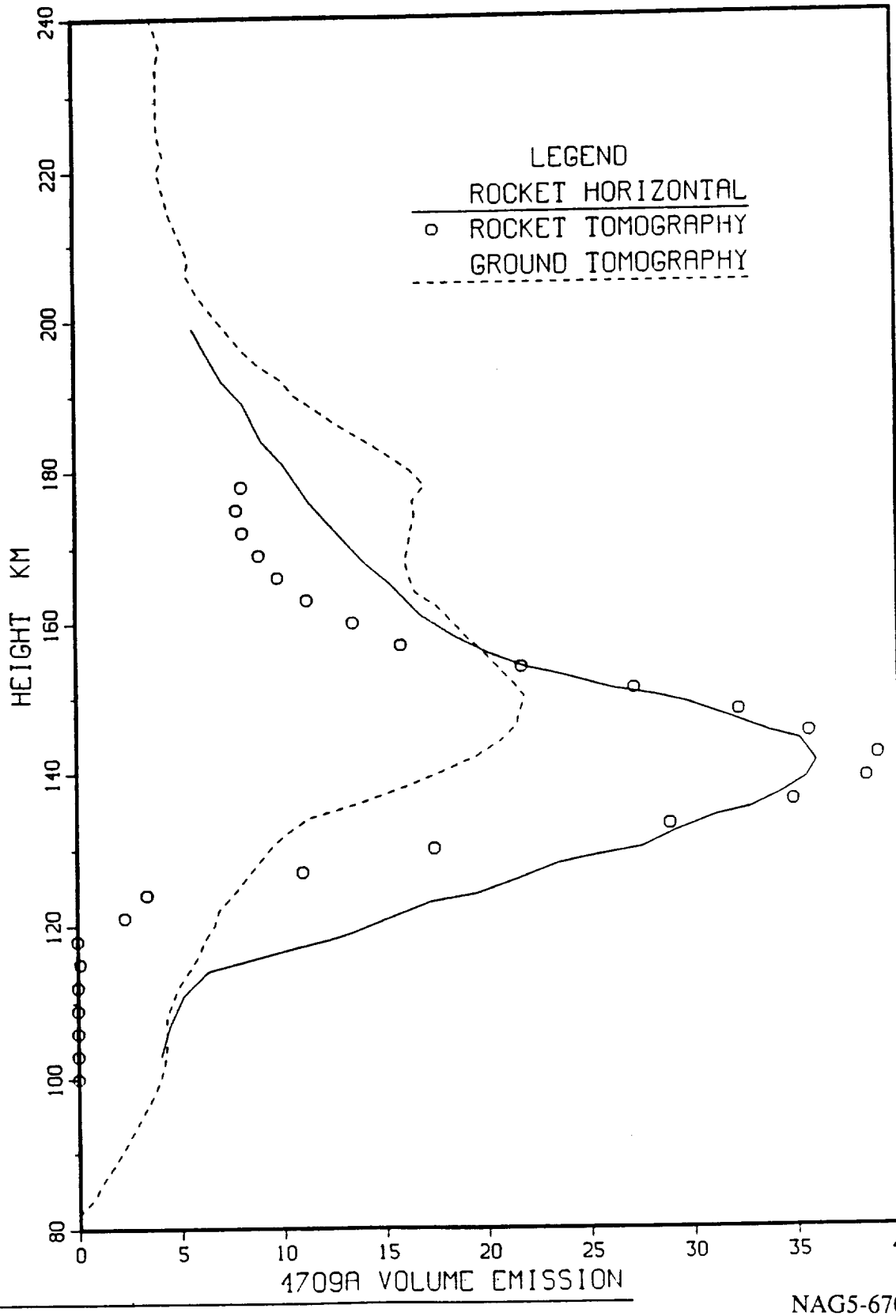

Fig. C11

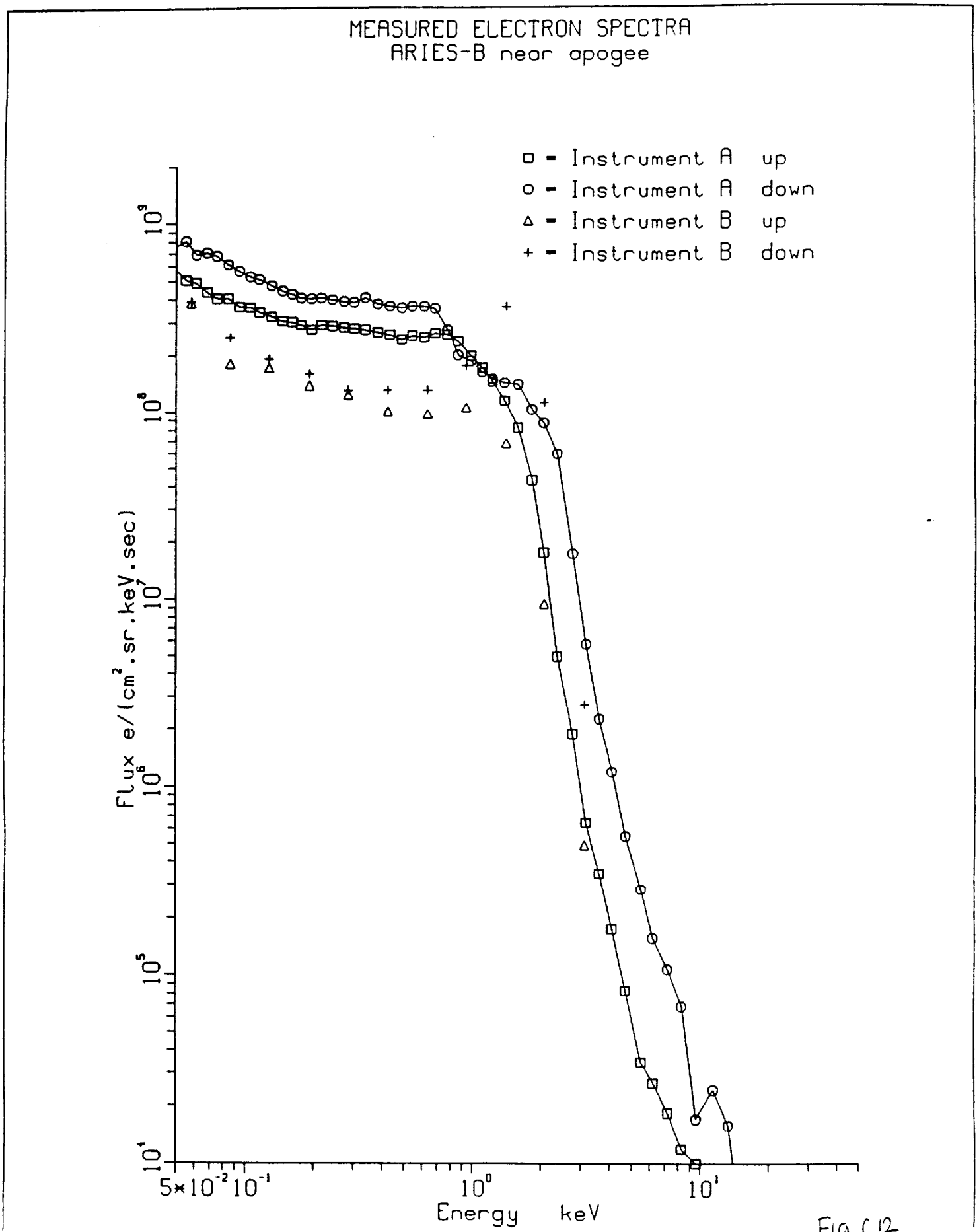
MEASURED ELECTRON SPECTRA
ARIES-B near apogee
□ - Instrument A up
○ - Instrument A down
△ - Instrument B up
+ - Instrument B down
Flux e/(cm².sr.keV.sec)
10⁹
10⁸
10⁷
10⁶
10⁵
10⁴
5×10⁻² 10⁻¹
10⁰
10¹
Energy keV

Fig. C 12

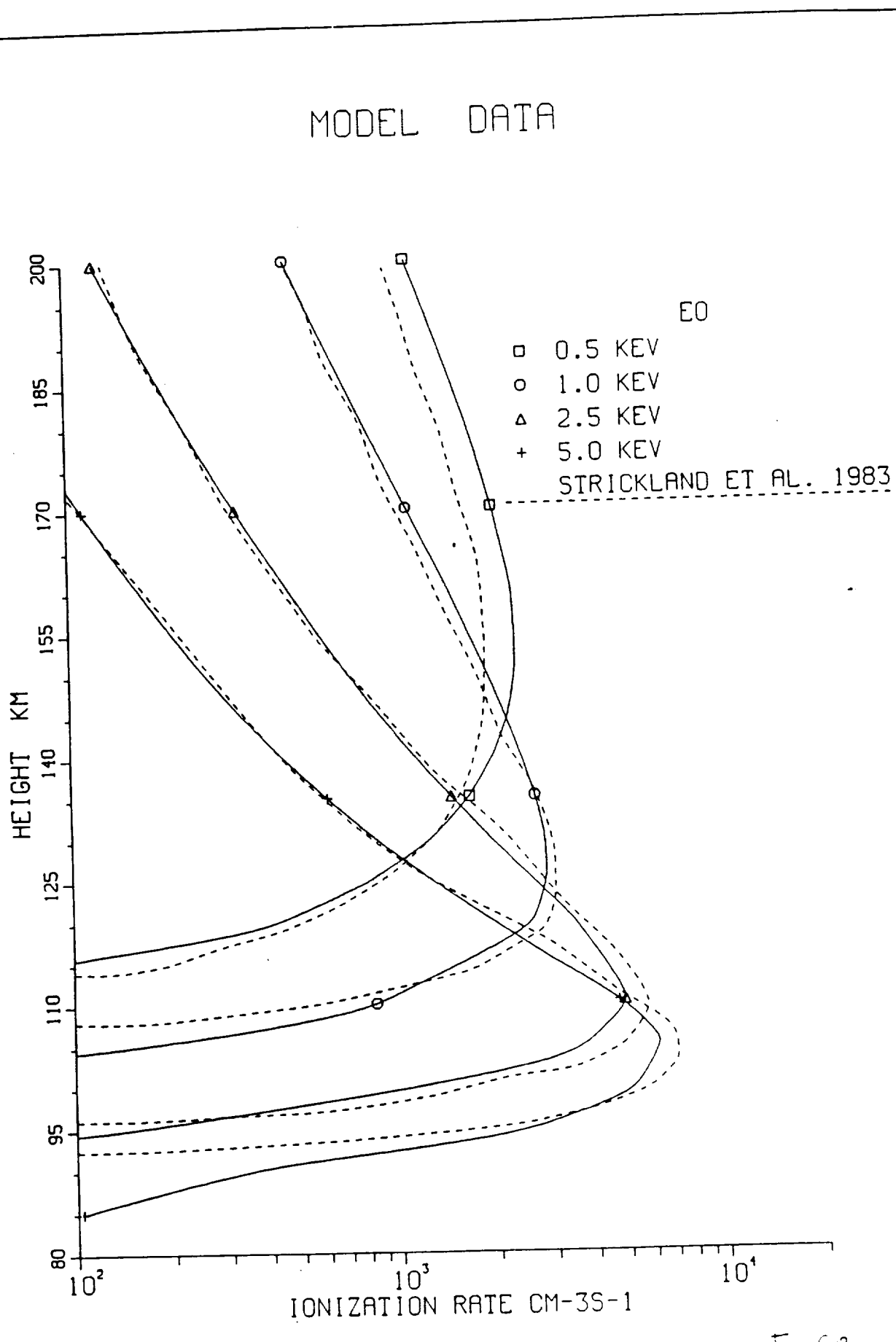
MODEL DATA
EO
0.5 KEV
1.0 KEV
2.5 KEV
5.0 KEV
STRICKLAND ET AL. 1983
HEIGHT KM
200
185
170
155
140
125
110
95
80
10^2
10^3
10^4
IONIZATION RATE CM-3S-1

Fig. C13

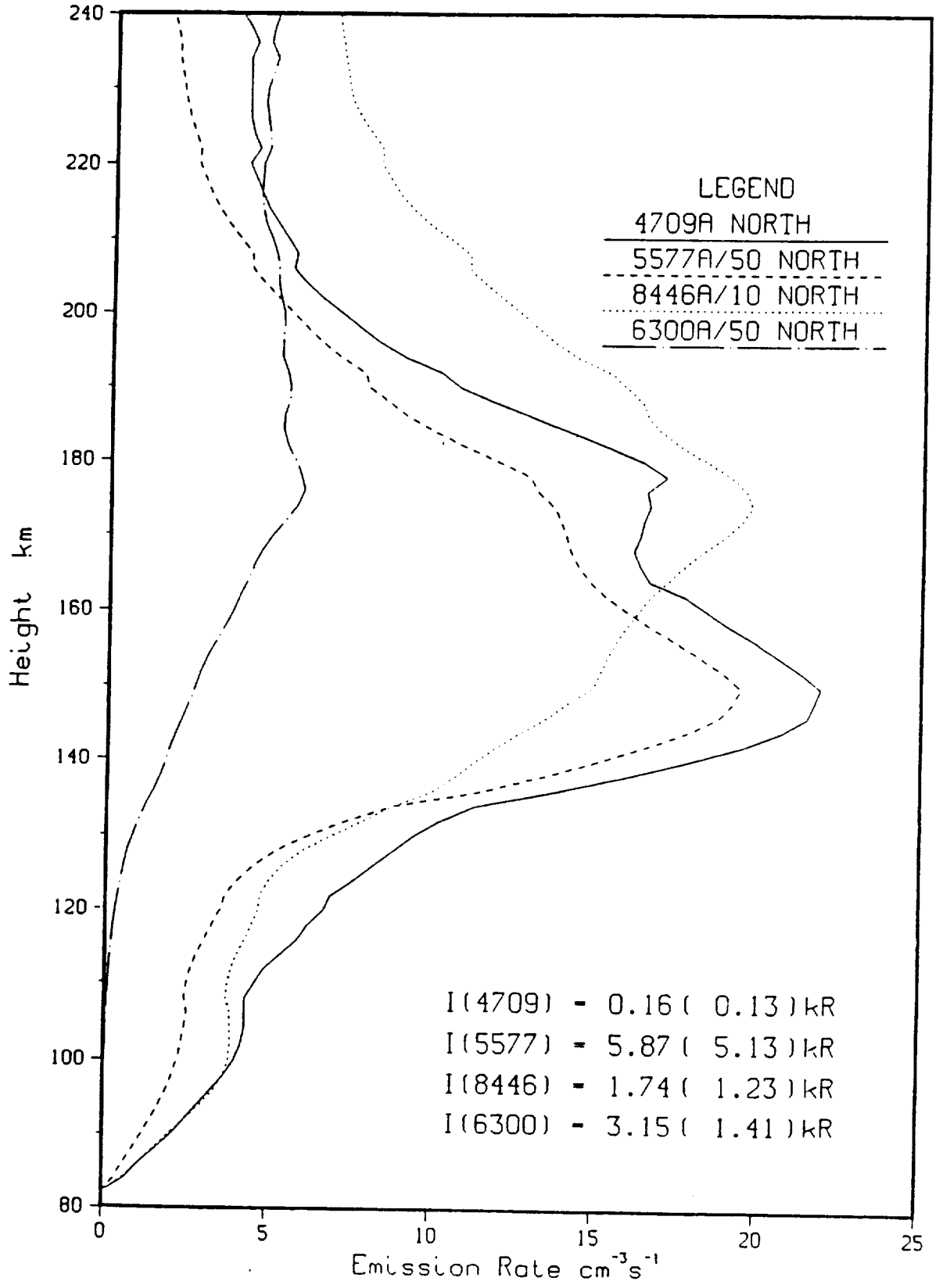
LEGEND
4709A NORTH
5577A/50 NORTH
8446A/10 NORTH
6300A/50 NORTH
I(4709) = 0.16 (0.13) kR
I(5577) = 5.87 (5.13) kR
I(8446) = 1.74 (1.23) kR
I(6300) = 3.15 (1.41) kR
Height km
240
220
200
180
160
140
120
100
80
0
5
10
15
20
25
Emission Rate cm^{-3}s^{-1}

Fig. C14

ARIES-B MODEL DATA

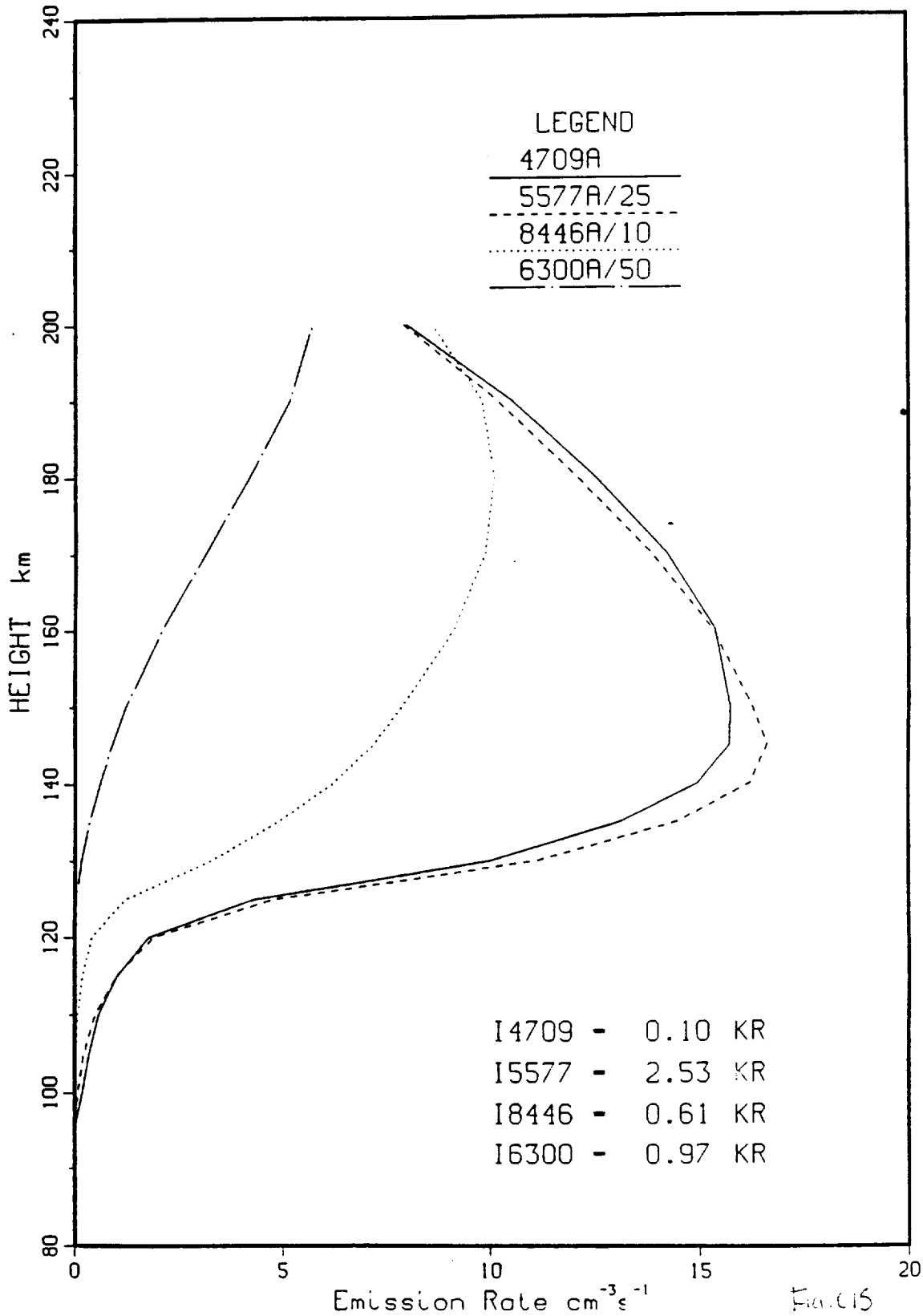

Fig. C15

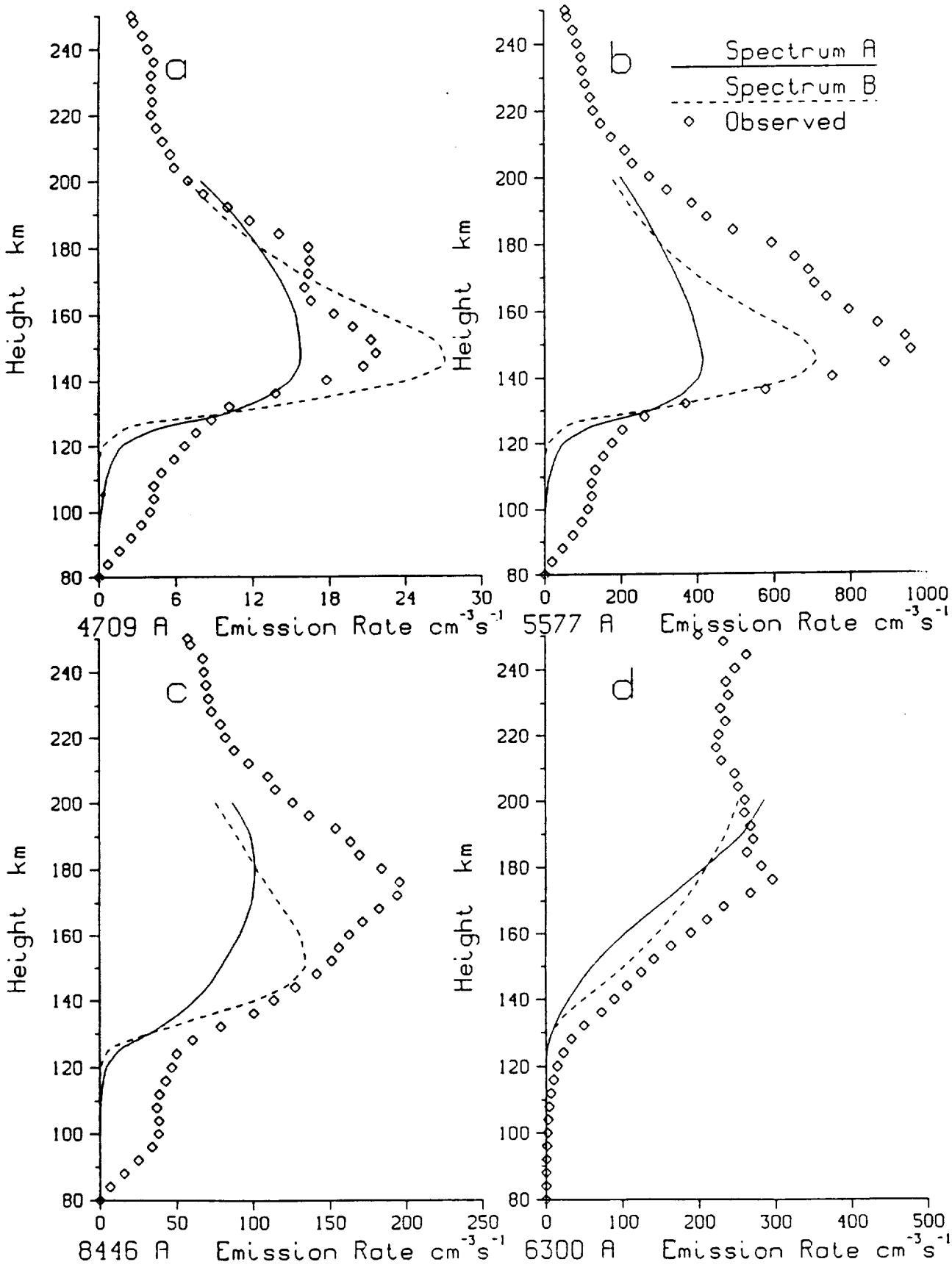
a
b
c
d
Spectrum A
Spectrum B
Observed
Height km
240
220
200
180
160
140
120
100
80
0
6
12
18
24
30
200
400
600
800
1000
50
150
250
4709 A Emission Rate cm^{-3}s^{-1}
5577 A Emission Rate cm^{-3}s^{-1}
8446 A Emission Rate cm^{-3}s^{-1}
6300 A Emission Rate cm^{-3}s^{-1}

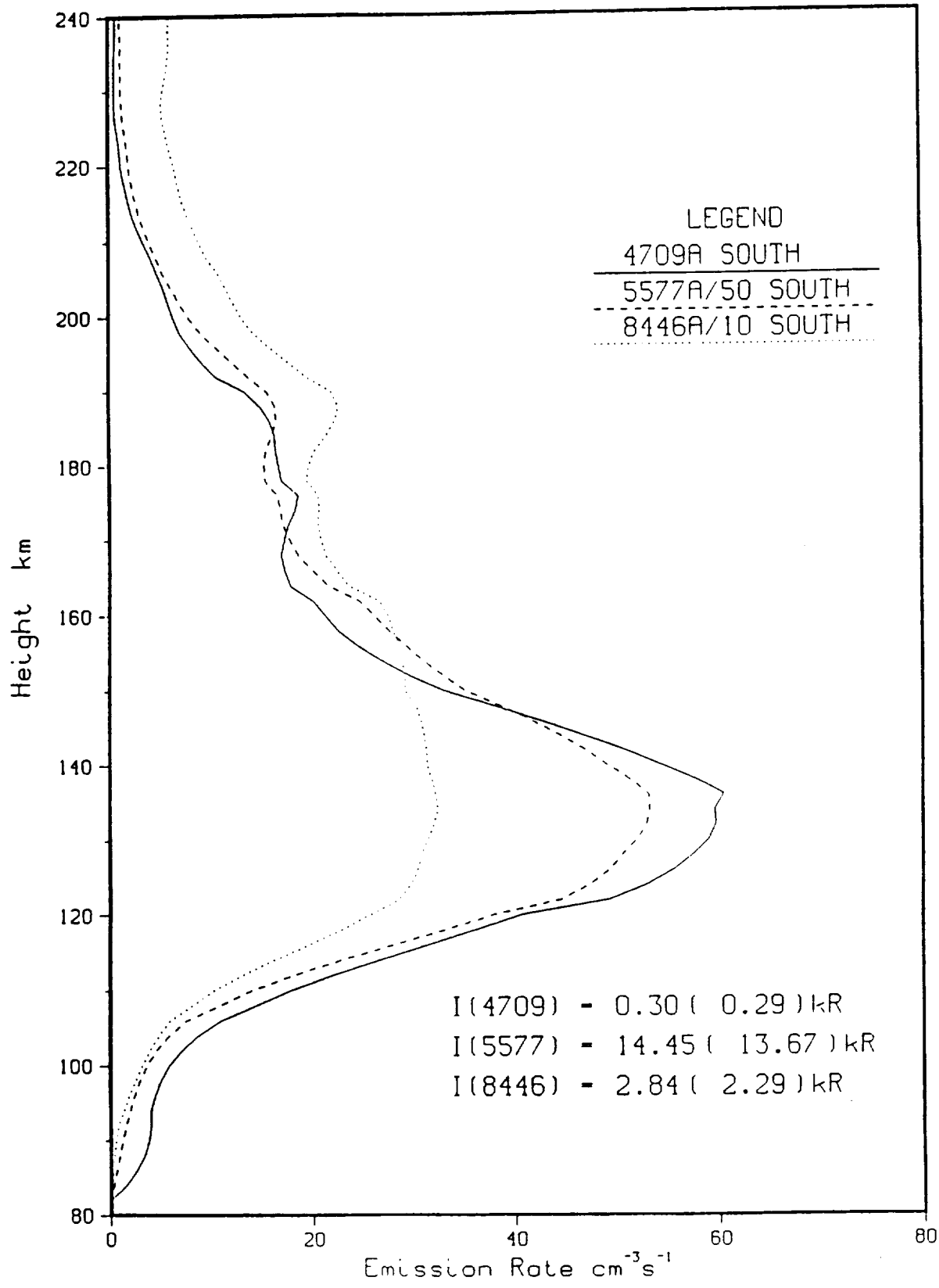
LEGEND
4709A SOUTH
5577A/50 SOUTH
8446A/10 SOUTH
I(4709) - 0.30(0.29)kR
I(5577) - 14.45(13.67)kR
I(8446) - 2.84(2.29)kR
Height km
240
220
200
180
160
140
120
100
80
0
20
40
60
80
Emission Rate cm^{-3}s^{-1}

Fig. C17

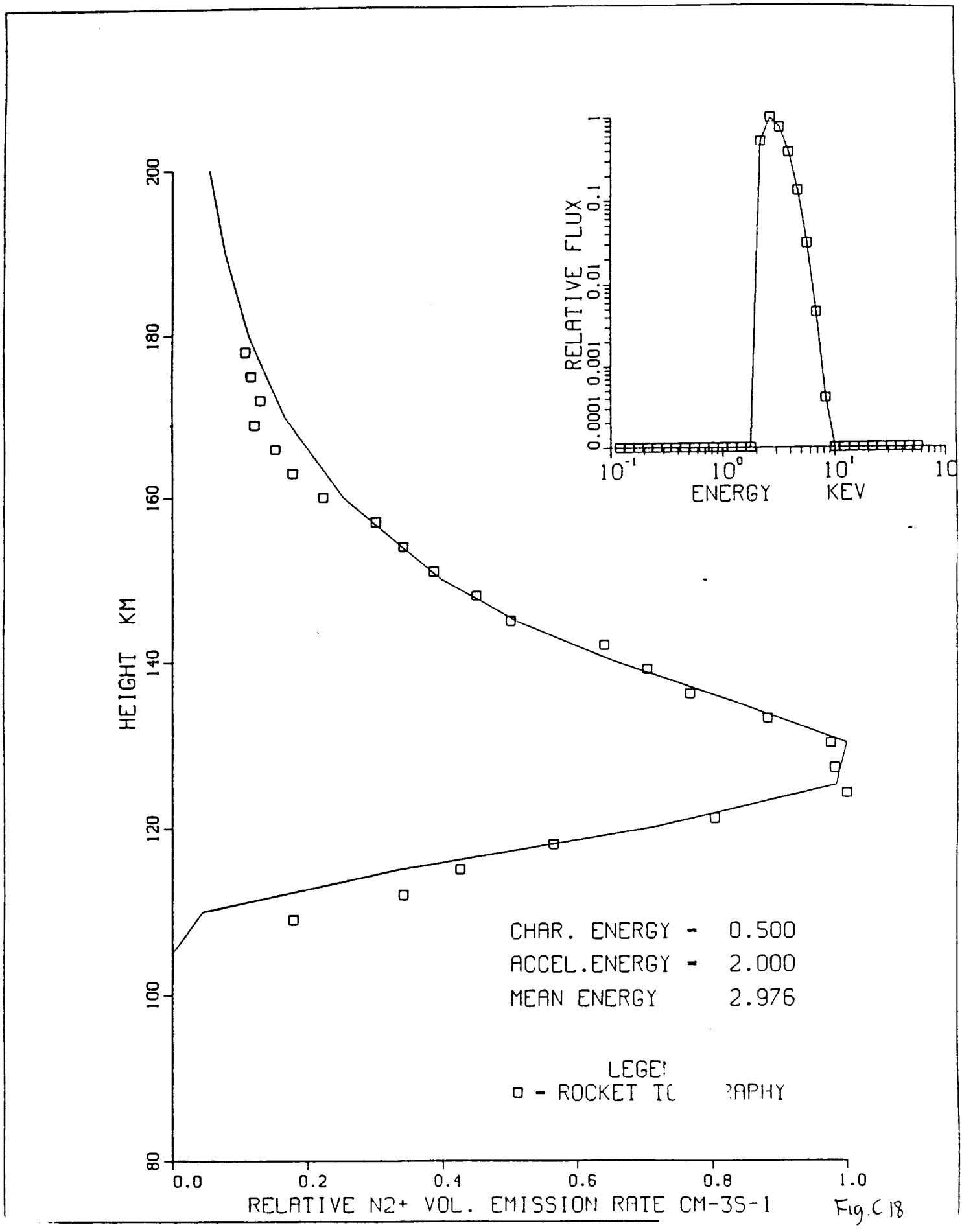
HEIGHT KM
200
180
160
140
120
100
80
0.0
0.2
0.4
0.6
0.8
1.0
RELATIVE N2+ VOL. EMISSION RATE CM-3S-1
RELATIVE FLUX
1
0.1
0.01
0.001
0.0001
10^{-1}
10^{0}
10^{1}
ENERGY
KEV
CHAR. ENERGY - 0.500
ACCEL.ENERGY - 2.000
MEAN ENERGY 2.976
LEGE
□ - ROCKET TC
APHY

Fig. C 18

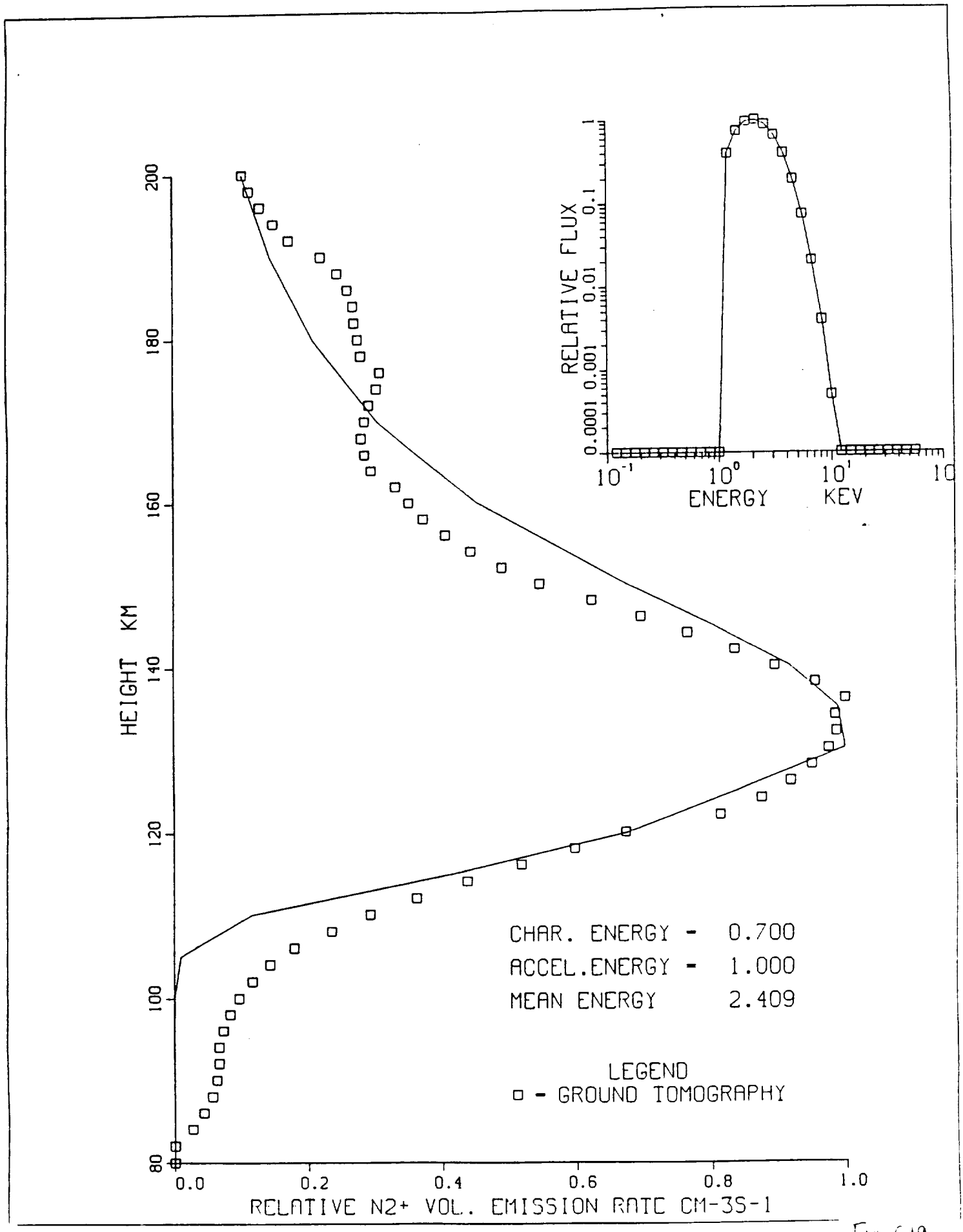
HEIGHT KM
200
180
160
140
120
100
80
0.0
0.2
0.4
0.6
0.8
1.0
RELATIVE N2+ VOL. EMISSION RATE CM-3S-1
RELATIVE FLUX
0.0001
0.001
0.01
0.1
1
10^{-1}
10^{0}
10^{1}
ENERGY KEV
CHAR. ENERGY - 0.700
ACCEL.ENERGY - 1.000
MEAN ENERGY 2.409
LEGEND
□ - GROUND TOMOGRAPHY

ARIES-B MODEL DATA

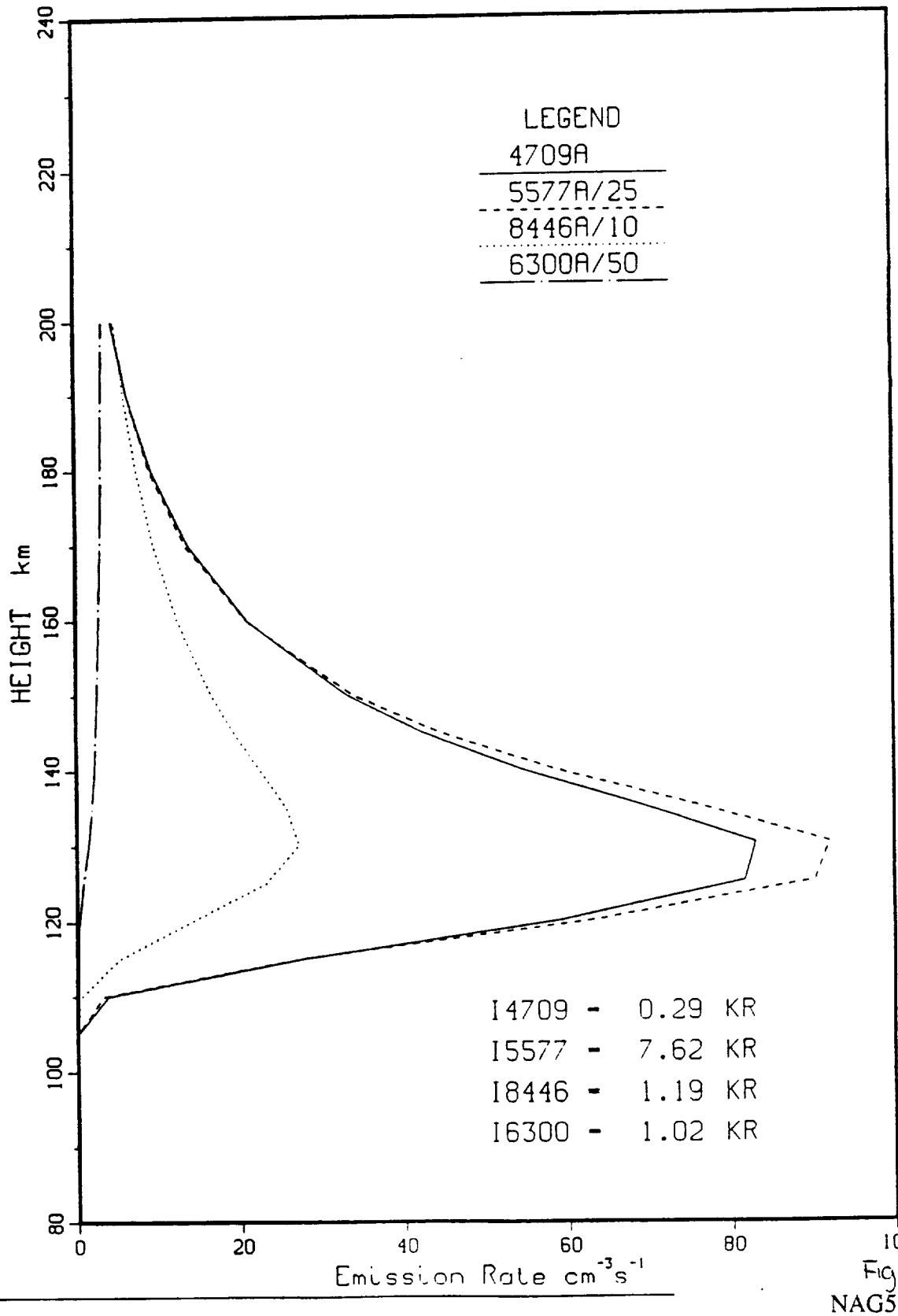

Fig. C20

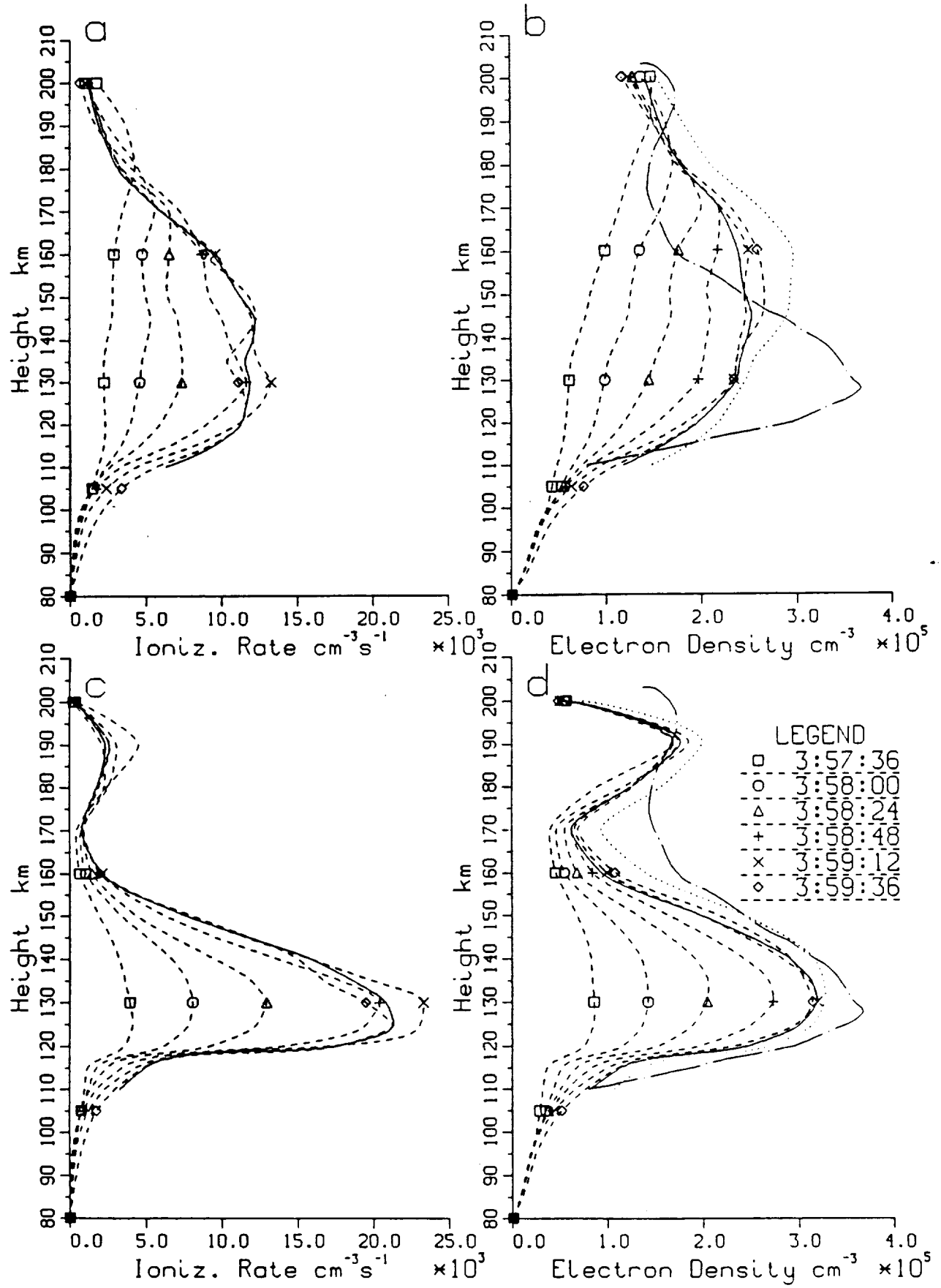
a
b
c
d
Height km
Ioniz. Rate cm^{-3}s^{-1} ×10^{3}
Electron Density cm^{-3} ×10^{5}
LEGEND
3:57:36
3:58:00
3:58:24
3:58:48
3:59:12
3:59:36

Fig. 22

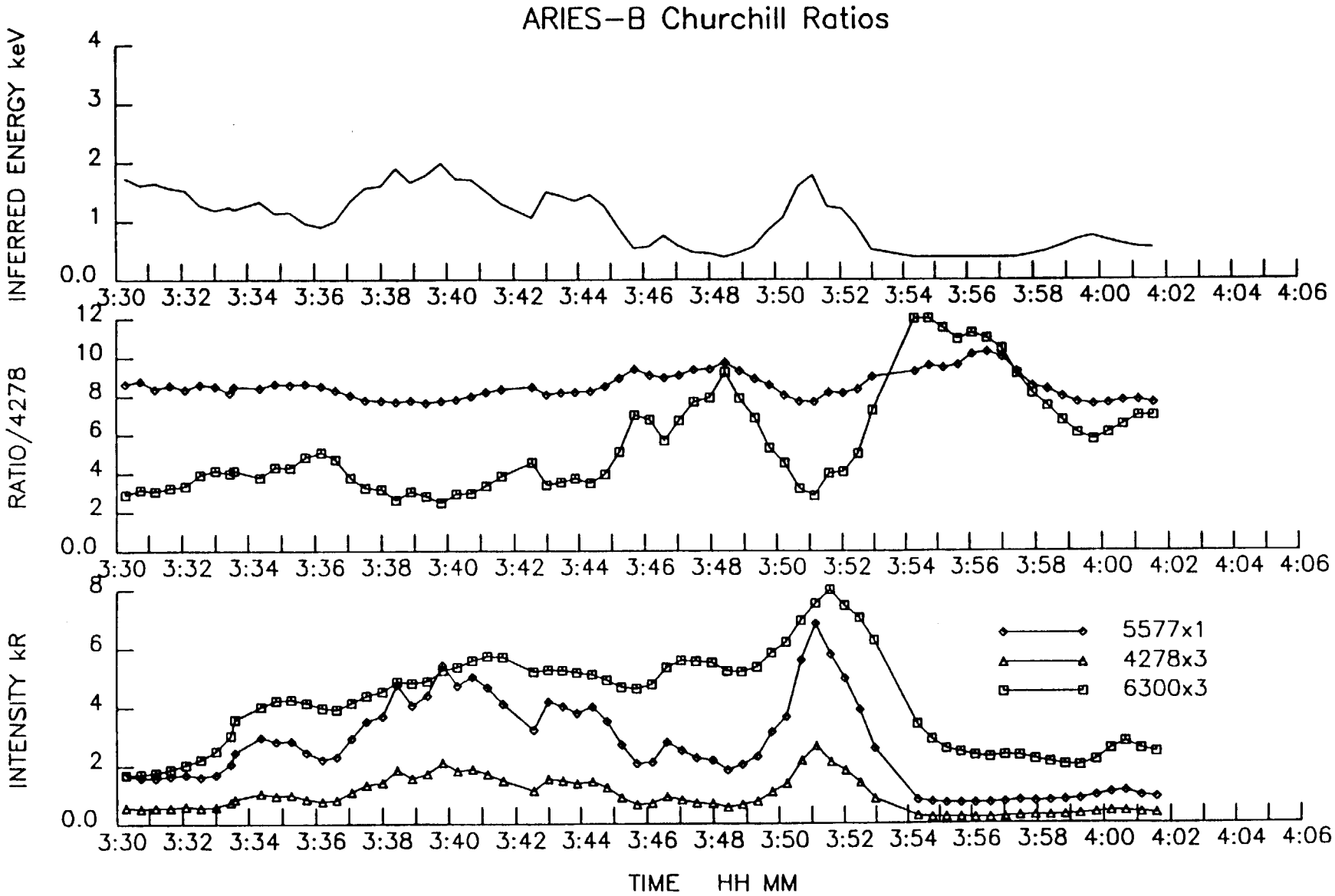

NAG5-670 'C' 79

Fig. C22.

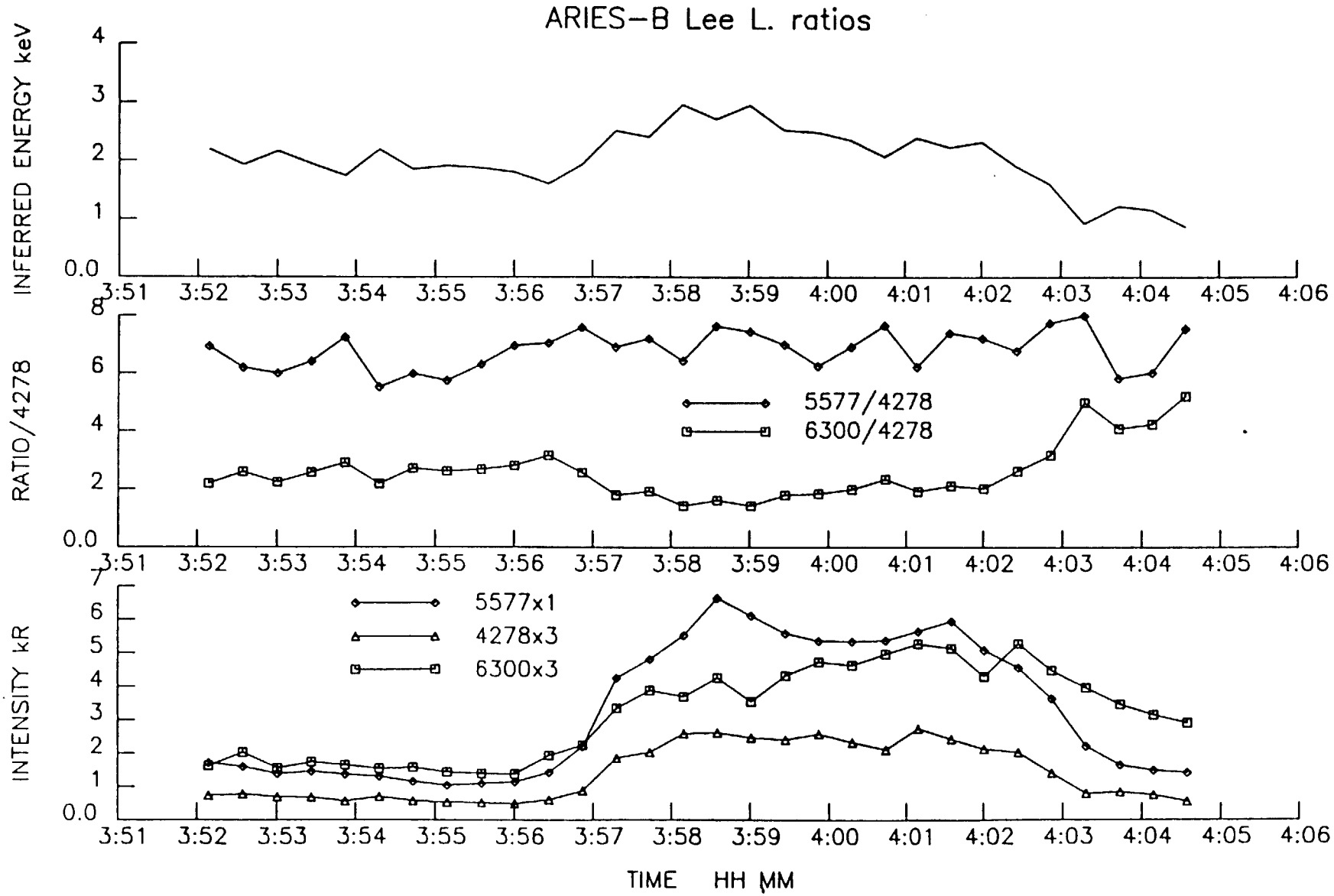

NAG5-670 'C' 80

Fig. C3